SYNTHESIS AND CHARACTERIZATION OF MAGNETIC CARBON NANOTUBES

SYNTHESIS AND CHARACTERIZATION OF MAGNETIC CARBON NANOTUBES

By AHMED MOHAMED S. A. ABDALLA, B.Sc., M.Sc.

A Thesis Submitted to the School of Graduate Studies in Partial Fulfilment of the
Requirements for the Degree Doctor of Philosophy

McMaster University

McMaster University DOCTOR OF PHILOSOPHY (2017) Hamilton Ontario
(Engineering Physics)

TITLE: Synthesis and Characterization of Magnetic Carbon Nanotubes AUTHOR: Ahmed Mohamed S. A. Abdalla, B.Sc. (Military Technical Collage, Egypt), M.Sc. (Military Technical Collage, Egypt) SUPERVISOR: Professor I. K. Puri NUMBER OF PAGES: xxiv, 181.

LAY ABSTRACT

The superior properties of carbon nanotubes (CNTs) are best manifested in bulk materials when the CNTs are organized axially and in tandem, and embedded in a continuous matrix. Decorating the CNTs with magnetic nanoparticles (MNPs) facilitates their organization through "action from a distance" with a magnetic field. The attachment of MNPs to the surfaces of CNTs can be realized through covalent or non-covalent (i.e. physical) bonding. This work develops both methodologies to investigate how the physical properties of magnetized CNT (mCNT) can be tuned and produce new CNT-based nanostructures for particular applications. First, mCNTs are utilized to synthesize a hitherto unreported class of colloidal suspensions based on which a magnetic bio ink is fabricated to print a fast-response biological sensor. Next, nickel-coated CNTs prepared using electroless deposition are used in the form of a filler at low volume fractions in an epoxy matrix, where they are aligned along multiple-direction using magnetic field, producing either anisotropic or isotropic bulk properties on demand. Finally, subsequent annealing of nickel-coated CNTs in air oxidizes nickel to nickel oxide while carbon is released in the form of gaseous carbon dioxide. This leads to another novel approach for the fabrication of nickel oxide nanotubes, which are demonstrated to be an alternate viable material to fabricate electrodes for use in supercapacitors.

ABSTRACT

The superior properties of carbon nanotubes (CNTs) are best manifest in bulk materials when the CNTs are organized in tandem and embedded in a continuous matrix. Decorating the CNTs with magnetic nanoparticles (MNPs) facilitates their expedient organization with a magnetic field. One of the most convenient methods for their decoration is to first treat the CNTs with oxidative acids, and then coprecipitated MNPs in situ. This method results magnetized CNTs that are covalently functionalized with the MNPs. The associated destruction in the CNTs required running a comparative study of this protocol to identify the influence of the acid treatment on the decoration of multiwalled CNTs (MWNTs). Further, we explore means to tune the physical properties of these magnetized CNTs (mMWNTs) by varying the (1) MNP material composition, and (2) MNP:MWNT (w/w) magnetization weight ratio (γ). The resulted composite materials (mMWNTs) are utilized to synthesize a novel and hitherto unreported class of colloidal suspensions (MCCs) for which the dispersed phase, which consists of MWNTs decorated with MNPs, is both magnetoresponsive and electrically conductive. Synthesis of the dispersed phase merges processes for producing ferrofluids and mMWNTs. Later, these MCCs are adapted and engineered to produce a biological ink containing MWNTs that are twice functionalized, first with MNPs and thereafter with the anti-c-Myc monoclonal antibodies (Abs). The ink is pipetted and dynamically self-organized by an external magnetic field into a dense electrically conducting sensor strip that measures the decrease in current when a sample containing c-Myc antigens (Ags) is deposited on it. On the other side, a nondestructive methods to magnetize MWNTs and provide a means to remotely manipulate them is through the electroless deposition of magnetic nickel nanoparticles on their surfaces. The noncovalent bonds between Ni nanoparticles and MWNTs produce a Ni-MWNT hybrid material (NiCH) that is electrically conductive and has an enhanced magnetic susceptibility and elastic modulus. Raising γ (Ni:MWNT weight ratios) increases the coating layer thickness, which influences the NiCH magnetic properties and tunes its elastic modulus. The NiCH was used to fabricate Ni-MWNT macrostructures and tune their morphologies by changing the direction of an applied magnetic field. Leveraging the hydrophilic Ni-MWNT outer surface, a water-based conductive ink was created and used to print a conductive path that had an electrical resistivity of 5.9 Ωm, illustrating the potential of this material for printing electronic circuits. Further, the NiCHs are introduced into an epoxy matrix at low 0.25-1% volume fractions and aligned along the direction of an applied magnetic field, which produces anisotropic bulk properties. However, nanoparticles aligned in perpendicular directions in sequential layers result in an effectively isotropic composite material. Furthermore, the subsequent annealing of the NiCH in the presence of air oxidizes nickel to nickel oxide whereas carbon is released as gaseous carbon dioxide, which leads to a novel approach for the fabrication of nickel oxide nanotubes (NiONTs) based on MWNTs as a sacrificial template. New chelating polyelectrolytes are used as dispersing agents to achieve high colloidal stability both for NiCH and NiONTs. A gravimetric specific capacitance of 245.3 F g^{-1} and areal capacitance of 3.28 F cm^{-2} at a scan rate of 2 mV s^{-1} is achieved with an electrode fabricated using nickel oxide nanotubes as the active element with a mass loading of 24.1 mg/cm^2.

TABLE OF CONTENT

LIST OF FIGURES

LIST OF TABLES

ACKNOWLEDGEMENTS:

This dissertation could not have been completed without the great support that I have received from so many people over the years. I would like to thank all the people who contributed in some way to the work described in this thesis. I wish to offer my most heartfelt thanks to them. First and foremost, I thank my Doctoral advisor, Professor. Ishwar K. Puri, for accepting me into his group. During my tenure, he contributed to a rewarding graduate school experience by giving me intellectual freedom in my work, engaging me in new ideas, and demanding a high quality of work in all my endeavors. Thank you for the advice, support, and willingness that allowed me to pursue research on topics for which I am truly passionate. Additionally, I would like to thank my committee members Professor John Preston, and Professor Gianluigi A. Botton for their interest in my work and their continuing guidance, you have my ultimate gratitude.

Every result described in this thesis was accomplished with the help and support of fellow lab-mates and collaborators. I would also like to thank Dr. Suvojit Ghosh for his assistance and guidance in getting my research work started on the right foot and providing me with the foundation for becoming a Ph.D. scholar. Additionally, I am very grateful for the friendship of all of the Multiphysics Research Group, especially Dr. Rakesh Sahu, Dr. Souvik Pal, Dr. Fei Geng, Abdel Rahman Abdel Fattah, Jenifer Tsai, Tahereh Majdi, Sarah Mishriki, Ri Chen, and Huifang Pang, whom I worked closely and puzzled over many problems. They helped me in numerous ways during various stages of my PhD. Many thanks to Abdel Rahman Abdel Fattah, Tahereh Majdi, and Jenifer Tsai, my road-mates from the beginning of my study. Ours friendship led to many brain storming sessions which results a lot of collaborative work and great projects that enriched my entire work. Thanks to Sarah, Elvira Meleca, and Dr. Fei Geng whom opened my eyes to the beauty of biology, and provided me with many biological knowledge. I wouldn’t be think to work in the supercapacitors and microwave absorbers without the collaboration that I have received from Ri Chen and Huifang Pang, thank you both for broaden my horizon. A very special thank you to Dr. Rakesh Sahu for his invaluable advice and feedback on my research and for always being so supportive of my work. He provides an ultimate guidance and assistance which led to many collaborations and successful projects. I would like to thank Professor. Igor Zhitomirsky for his advice and guidance through my first-time work in energy storage materials (e.g. supercapacitors).

This work is supported by a Natural Sciences and Engineering Research Council of Canada (Grant no.RGPIN-2014-04066) Discovery Grant (NSERC-DG), Canada Foundation for Innovation (Grant no.33016) John R. Evans Leaders Fund (CFI-JELF) and Ontario Research Fund Research Infrastructure (ORF-RI) grants. I would like to thank the following for assistance with measurements: Dr. Gregory Wohl of Department of Mechanical Engineering at McMaster University for assisting in tensile strength measurements, Dr. Carmen Andrei of Canadian Centre for Electron Microscopy for TEM/STEM, Ms. Victoria Jarvis of McMaster Analytical X-Ray Diffraction Facility for XRD, Dr. Paul Dube of Brockhouse Institute for Materials Research, Professor. Marek Niewczas of Materials Science and Engineering, McMaster University for PPMS, and Abhishaik Rampal of the Department of Engineering Physics at McMaster university for assisting in the AC electrical resistivity measurements. AMA thanks the Egyptian Armaments Authority for a Ph.D. scholarship.

Finally, and most importantly, I would like to acknowledge friends and family who supported me during my time here. I would like to thank my wife Doaa Saleh. Her support, encouragement, quiet patience and unwavering love were undeniably the bedrock upon which the past eleven years of my life have been built. Thank you for your love, friendship, and unyielding support. I thank my parents, for their faith in me and allowing me to be as ambitious as I wanted. It was under their watchful eye that I gained so much drive and an ability to tackle challenges head on. Also, I thank my siblings whom provided me with unending encouragement and support.

LIST OF ABREVIATIONS

Ab	Antibody
AC	Alternative current
AFM	Atomic force microscopy
Ag	Antigen
aMWNT	Activated multiwalled carbon nanotubes
Bioink	Biological ink
BSA	Bovine serum albumin
CNT	Carbon nanotube
CVD	Chemical vapor deposition
D_c	Critical diameter
Dc	Direct current
DI Water	Deionized water
DLS	Dynamic light scattering
DM	Double magnetized
D_s	Super paramagnetic diameter
DWNT	Double walled carbon nanotubes
EDX	Energy dispersive X-ray analysis
EELS	Electron energy loss spectroscopy
EGFP	Enhanced green fluorescent protein
ELISA	Enzyme linked immunosorbent assay
FET	Field effect transistor
FEMM	Finite element method magnetics
FF	Ferrofluid
FITC	Fluorescein isothiocyanate
FTIR	Fourier transformer infrared spectrometry
HRTEM	High resolution transmission electron microscope
IGFs	Insulin-like growth factor

mBioink	Magnetic biological ink
MCC	Magnetoresponsive and conductive colloidal suspension
MCH	Metal-CNT hybrid nanomaterial
mCNT	Magnetic carbon nanotube
MNP	Magnetic nanoparticle
MWNT	Multiwalled carbon nanotube
mMWNT	Magnetic multiwalled carbon nanotube
NiCH	Ni-CNT hybrid material
NiONT	Ni oxide nanotube
NP	Nanoparticle
PCR	Polymeric chain reaction
PDF	Powder diffraction file
PDMS	Polydimethylsiloxane
PLC	Programmable logic controller
PSA	Prostate specific antigen
SEM	Scanning electron microscopy
SQUID	Superconducting quantum interference device
STEM	Scanning transmission electron microscopy
SWNT	Single walled carbon nanotubes
TEM	Transmission electron microscopy
TMAH	Tetra methyl ammonium hydroxide
VSM	Vibrating sample magnetometer
XPS	X-ray photoelectron spectroscopy
XRD	X-ray diffraction

LIST OF SYMBOLS

$\boldsymbol{c}$	Chiral vector
θ	Angle
$\boldsymbol{r}$	Radius
r_o	The equilibrium bond length
χ	Magnetic susceptibility
μ	Permeability
$\boldsymbol{H}$	Magnetic field
$\mathbf{E}$	Electric field
$\boldsymbol{B}$	Magnetic induction
$\boldsymbol{M}$	Magnetization
M_r	Remanence magnetization
M_s	Saturation magnetization
H_c	Coercive field
I	Electric current
$\boldsymbol{J}$	Electric current density
q	Electric charge
p	Magnetic charges
ω	Angular frequency
f	Frequency
A	Area
$\boldsymbol{m}$	Magnetic moment
$\boldsymbol{m_o}$	Orbital magnetic moment
$\boldsymbol{m_s}$	Spin magnetic moment
$\boldsymbol{l}$	Orbital angular momentum
$\boldsymbol{s}$	Spin angular momentum
$\boldsymbol{v}$	Velocity
m_e	Electron mass

$\hbar$	The reduced Planck constant (1.055×10^{-34} J s)
μ_B	Bohr magneton
$\boldsymbol{F}$	Force
$\boldsymbol{\Gamma}$	Torque
E	Elastic modulus
N	Number of moles
V	Volume
U	Potential energy
γ	Magnetization weight ratio (MNP:MWNT)
β	Bio-functionalization weight ratio (an anti-c-Myc:MWNT)
λ	Wavelength
a, b, and c	Lattice space parameters
D	Crystal size
B	The full width at half maximum
ζ	Zeta potential
σ	Electrical conductivity
R	Electrical resistance
ρ	AC Electrical Resistivity
Z^*	Complex impedance
C_S^*	Complex differential capacitance

1. Introduction

1.1 The Era of Nanotechnology

Nanometer, a word referring to a length scale (one billionth of a metre) [1], is used to express objects such as viruses (cold virus, 25 nm) and DNA molecule (width of 2 nm). The understanding, measuring, manipulating, controlling, and using such nano-scaled materials (dimensions of <100 nm) is defined as nanotechnology [1-3]. The 21st Century can be considered as the era of the nanotechnology as this technology has spread across the world and becomes one of the technologies with enormous potential for current and future applications. Nanotechnology provides a unique and novel use and application in contrast to that existing in conventional materials and technologies. Nowadays, nanotechnology along with nanomaterials not only play an important role in science, research and development, but also is ubiquitous in everyday's life products [3]. Nanomaterials have a huge surface area per unit volume in comparison to conventional materials, e.g. by splitting an object with dimensions ~ cm into nano-fragments, the total surface area will therefore increase by millions times [2, 4]. Top-down (e.g. nanofibers produced by electrospinning) and bottom-up (e.g. carbon nanotubes (CNTs) produced by vapour deposition) technologies are the most common approaches used currently to make nanomaterials [3, 4]. The former technology starts with a micro/macro-sized materials which is then subsequently cut down to the nanometer scale using lithographical and etching techniques.

In contrast, the latter technology uses the self-organization of atoms or molecules to build up the nanostructures [3, 4].

At the intermediate stage between the atomic level and bulk material, nanoparticles gained a lot of interest. The nanomaterials feature exceptional physical properties that differ from bulky materials, this includes chemical reactivity (catalysis), sensing activity, absorption, dispersion ability, waterproofing, anti-microbial, high strength, and varying thermal, electric, magnetic, optical properties [2, 4]. Nanomaterials are unique as most of its material is situated at the surface, e.g. in single walled carbon nanotubes (SWNTs), all the carbon atoms are located at the surface. Also, when the particle size becomes smaller than the de Broglie wavelength, the optical properties of nanoparticles is significantly affected. Further, at a size smaller than the critical domain size (~few nm), ferromagnetic nanoparticles consists of a single domain that exhibits a superparamagnetic behavior where any retained magnetization can be removed by thermal energy. Furthermore, if the material's structure can constrain the length of cracks caused by stress within few nanometers, the stresses needed for the material failure would significantly increase [3].

Nanomaterials exists in different forms such as nanoparticles or even thin layer of few atoms [2, 4]. Nanoparticles could be of metals, metals oxides or carbon. Spheres are the most energetically favorable shape for the nanoparticles, however, other materials like hollow nanoballs, nanorods, nanowires, or nanotubes of diameter in nano-scale and length in nano/micro-scale can be formed. In all of them, carbon based nanomaterials provide a wide variety of physical properties associated with low density and currently, used in many potential applications [1].

1.2 The World of Carbon

Carbon (C, atomic number of 6) is the vital element of living creature and all known life. It is the 4th most abundant element in the Universe by mass. The unique ability of carbon to bond to itself and other elements forming millions of organic compounds and polymer chains allows it to act as an important role in our life [5, 6]. Carbon atom has four electrons participating in covalent bonding, resulting compounds with strong σ bonds due to the s and p orbitals hybridization, whereas the $2p_z$ orbitals can form weak π bonds in some other cases [6, 7]. The most common form of carbon is soot which has an amorphous structure. The formation of highly ordered carbon nanostructures with controlled morphology (tubes, spheres, helices and Y-junctions) requires depositing carbon atoms under controlled conditions [6]. Carbon atom is capable of forming multiple bonds (e.g. C-C, C=C and C≡C bonding) allowing it to form many types of allotropes such as diamond (3D structure; cubic lattice; sp^3 hybridization) is the metastable form of carbon, graphite or graphene (2D structure; layers with weak interlayer bonding; sp^2 hybridization) are the most thermodynamically stable form of carbon at room temperature, CNTs (1D structure; rolled sheets of graphene; sp^2 hybridization), fullerenes (0D structures; spheres formed by curling up sheet of graphene; sp^2 hybridization), and mesoporous carbon structures [6-10].

The carbon-carbon interaction significantly influences both the chemical and physical properties of the formed compound [6, 10]. The featured physical and chemical properties depends on their unique atomic structures [9, 10]. All carbon nanomaterials benefit from the low atomic weight of the carbon atom (one-sixth of iron). SWNTs are the strongest material synthesised to date, while diamond is the hardest known one. Carbon nanomaterials have a wide electronic properties depending on the bonding and the structure, e.g. carbon nanomaterials couth either be conductors, semi-conductors or even insulators. In most of the carbon nanomaterials, surface functionalization can be performed to modify their physical or chemical properties [6].

The carbon bonded structures with sp^2 hybridization are the strongest material ever measured on earth. The famous examples are CNTs and graphene which show the most outstanding properties; i.e. exceptional mechanical properties, low density, huge surface area, high stability, unique electrical and electronic properties, and wide electrochemical stability window. They are widely used in a range of applications; e.g., reinforced composite materials, catalysis, sensing, microelectronics, energy storage, energy conversion devices, and medicine [8, 10, 11].

1.3 Amazing Material: Carbon Nanotubes

Graphite, an amazing member in the club of the carbon nanostructures with sp^2 hybridization has the unique honeycomb atomic arrangement of the carbon atoms, where each atom form three σ bonds with their neighbours atoms. In 1991 Iijima observed tubular nanoshapes that are based on the unique structure of graphite. They consist of several graphitic layers rolled up into tubular shape (multiwalled carbon nanotubes (MWNTs)) [12]. These CNTs are long and thin cylinders with a diameter of 1-100 nm, that provide a best example of the true nanotechnology that is very useful for numerous applications. CNTs are electrically conductive like copper with thermal conductivity five times more than copper. Their measured mechanical strength is 20 times stronger than steel with density 5 times lighter [5]. The discovery of the CNTs with these extraordinary properties opened an incredible window for applications in the fields of materials science, electronics, chemical processing, energy, and biomedical applications [5-7]. CNTs can be made of only one layer of graphene (single-wall, SWNT), or many layers (multiwall, MWNT). Practically, their production introduces defects into their basic hexagonal carbon structure (e.g. pentagons, heptagons, and other imperfections) which degrade their featured physical properties [6, 7, 13].

Usually, CNTs are synthetized by heating a carbon precursor in the presence of a catalyst through one of three common fabrication techniques, e.g. arc-discharge, laser ablation and chemical vapour deposition [6, 7, 9, 12]. However, most of the bulky production results into unorganized CNT fragments that have limited properties which disturb the efficient and reliable use in widespread technologies. This raises the demand of obtaining, sorting and assembly techniques for large scale production of an organized and aligned CNTs in the form of forests, yarns, and sheets [9, 13].

1.4 Why to Functionalize CNT?

By definition, functionalization means the introduction of foreign atoms or molecules into the skeleton of the CNT, either by chemical bonding or physical adsorption [6, 14]. The objective of functionalizing CNTs is to modify a certain physical and chemical properties of the CNTs [6]. The extraordinary properties of the CNT make them suitable for several field of applications. However, functionalization could act as a mean to tailor and engineer new nanostructures according to the desired application [14]. Bridging or immobilizing biological or chemical molecules onto the nanotubes allows them to perform as bio/chemical sensors [14, 15]. Adsorption of oxygen molecules or functionalization with ferromagnetic atoms convert the diamagnetic behaviour of the CNT to ferromagnetic. SWNTs with zigzag chirality is a semiconductor with diamagnetic properties, however, the coating with titanium makes it conductive and magnetic [14].

Another benefit of functionalizing CNTs is to overcome its surface related problems. CNTs are poorly dispersible in polar solvents and polymer matrices. Surface functionalization of CNT's outer wall with polar molecular groups assists in enhancing the dispersion ability and improves its interfacial bonding with polymer chains, which allows effective utilization of CNT in solvent and composite applications [6]. Therefore, functionalization of CNTs can improve the physical properties by overcoming the CNT's surface problems, e.g. functionalizing CNTs with magnetic nanoparticles to enhance their dispersion ability and modifies their magnetic properties (a way to remotely control and manipulate) which finally can result in organizing the dispersion inside a polar matrix [16-19].

1.5 Magnetizing CNT: A Way to Remotely Control & Manipulate

Among different means of manipulation, magnetic field is the most economic, non-intrusive and efficient tool that can be used to manipulate magnetic objects and particles with action from a distance. It has been explored to manipulate and organize ferromagnetic, as well as diamagnetic nanoparticles in tandem to produce a pattern with certain functions

[18, 20]. e.g. Pisanello et al. were able to change the dielectric properties of a matrix utilizing the dynamic-assembly of magnetite nanoparticles under a magnetic field [21]. Also, Shin et al. successfully guided neurospheres that have been labeled with bacterial magnetic nanoparticles using a magnetic field [22]. However, many other similar examples of manipulating objects by magnetic field are also available [23-25].

When placed in an external magnetic field, magnetic nanoparticles feature large dipole moments, which consequently allow them to align and agglomerate, forming chains or rod-like microstructures [24]. This makes them very suitable to chaperone CNTs, and later when embedded into the polymer matrix, gets aligned and organized under the influence of external magnetic field. CNTs being quasi-one dimensional, their properties will be best manifested in the bulk if they are aligned along a particular direction in the matrix [18]. Herein, we are not only trying to magnetize CNTs in order to align them, but also to overcome the CNT's surface related problems, to allow their use in different applications. Further, we are trying to align and organize the mCNTs inside a polymeric matrix into a single layer i.e. aligning in 1D or in two consecutive layers aligned in perpendicular directions i.e. aligning in 2D and furthermore, investigate the effect of these aligning on the physical properties of the produced composites.

1.6 Outline

1.6.1 Background

The background chapter is intended to provide the reader with an overview of magnetization techniques in preparation for subsequent chapters. The reader will learn primarily about CNTs: history, structures, types, applications, and key problems, and magnetism and its fundamentals, followed by the methodologies for functionalizing and magnetizing CNTs. A brief discussion on the potential applications of the mCNT is also provided.

1.6.2 Magnetizing MWNT via Covalent Functionalization

In this chapter, background information and experimental investigations are presented to highlight the magnetization of MWNT via covalent functionalization. The results discussed in this chapter have been previously published in the articles titled *Decorating carbon nanotubes with co-precipitated magnetite nanocrystals*, Ahmed M Abdalla, Suvojit Ghosh, and Ishwar K Puri, available online on April 08, 2016 (DOI: 10.1016/j.diamond.2016.04.003) in the *Diamond and Related Materials* and *Magnetoresponsive conductive colloidal suspensions with magnetized carbon nanotubes*, Ahmed M Abdalla, Abdel Rahman Abdel Fattah, Suvojit Ghosh, and Ishwar K Puri, available online on August 08, 2016 (DOI: 10.1016/j.jmmm.2016.08.031) in the *Journal of Magnetism and Magnetic Materials*. The author of this thesis is the first author and main contributor of the above mentioned publications and has conducted all the experiments.

1.6.3 Conductive Nano-inks Based on Covalently Magnetized MWNTs

In this chapter, background information and experimental investigations are presented to highlight the application of magnetic MWNT synthesised via covalent functionalization in the fabrication of conductive nano-ink and then the adaptation of this ink to print a biosensor. Some of the results discussed in this chapter have been previously published in an article titled *Magnetoresponsive conductive colloidal suspensions with magnetized* *carbon nanotubes,* Ahmed M Abdalla, Abdel Rahman Abdel Fattah, Suvojit Ghosh, and Ishwar K Puri, available online on August 08, 2016 (DOI: 10.1016/j.jmmm.2016.08.031) in the *Journal of Magnetism and Magnetic Materials*. The author of this thesis is the first author and main contributor of the above mentioned publication and has conducted all the experiments. Rest of the work and results have been previously published in an article titled *Magnetic Printing of a Biosensor: Inexpensive Rapid Sensing to Detect Picomolar Amounts of Antigen with Antibody-Functionalized Carbon Nanotubes,* by Abdel Rahman Abdel Fattah, Ahmed M Abdalla, Sarah Mishriki, Elvira Meleca, Fei Geng, Suvojit Ghosh, and Ishwar K. Puri, available online on March 20, 2017 (DOI: 10.1021/acsami.6b15989) in ACS Applied Materials and Interfaces. The author of this thesis is the co-first author with Dr. A. R. Abdel Fattah, Ms. S. Mishriki of the above mentioned publication and has performed the magnetization of carbon nanotubes toward the biological ink's preparation and done the materials characterization.

1.6.4 Magnetizing of MWNT via Non-covalent Functionalization (Ni-MWNT Hybrid Nanomaterials)

In this chapter, background information and experimental investigations are presented to highlight the magnetization of MWNT via non-covalent functionalization. The results discussed in this chapter have been previously published in an article titled *Fabrication of Nanoscale to Macroscale Nickel-Multiwall Carbon Nanotube Hybrid Materials with Tunable Material Properties,* Ahmed M Abdalla, Tahereh Majdi, Suvojit Ghosh, and Ishwar K Puri, available online on December 07, 2016 (DOI: 10.1088/2053-1591/3/12/125014) in the *Material Research Express*. The author of this thesis is the first author and main contributor of the above mentioned publication and has conducted all the experiments.

1.6.5 Tailoring the Properties of a Ni-MWNTs Based Polymer Nanocomposite Using a Magnetic Field

The background information presented in this chapter is meant to briefly inform the reader about the advances and limitations of using CNTs in polymeric composite materials. An experimental investigation followed by results and discussion section highlights the effect of multi-directional alignment of nickel coated CNTs inside a polymer matrix on the physical properties of the resulted composite. The results discussed in this chapter have been submitted to the journal of *Composites part B: Engineering*. The author of this thesis is the first author and main contributor of the above mentioned publication and has conducted all the experiments.

1.6.6 Supercapacitor Based on Nickel Oxide Nanotubes Synthesized from Ni-MWNT Hybrid Nanomaterials

The background information presented in the chapter discusses the application of metal oxides in supercapacitors followed by experimental investigations highlighting a novel approach for the fabrication of nickel oxide nanotubes based on MWNTs as a sacrificial template. The results discussed in this chapter have been previously published in an article titled *Nickel Oxide Nanotubes Synthesis using Multiwalled Carbon Nanotubes as Sacrificial Templates for Supercapacitor Application*, Ahmed M Abdalla, Rakesh P. Sahu, Cameron J. Wallar, Ri Chen, Igor Zhitomirsky, and Ishwar K Puri, available online on January 16, 2017 (DOI: 10.1088/1361-6528/aa53f3) in *Nanotechnology*. The author of this thesis is the first author and main contributor of the above mentioned publication and has conducted all the experiments except the electrochemical characterization section.

1.5.7 Summary and Future Work

This final chapter provides a summary of the entire thesis with an emphasis on the contributions of each chapter. These concluding remarks reconnect the various chapters and works conducted in the thesis emphasizing the usefulness of mCNTs in potential engineering applications. Further, the chapter includes some thoughts about the future work that has to be done to fill the gaps and improve the current work.

2. Background

2.1 Carbon Nanotubes

2.1.1 Historical

With little scientific interest then, during 1970s, vapour grown, carbon nano-filaments were produced as a by-product during oxygen-limited combustion along with carbon fibers. Later, in 1991, these nano-filaments were investigated by Iijima using high resolution transmission electron microscopy (HRTEM), which led to the discovery of multiwalled carbon nanotubes (MWNTs) [26]. In 1993, single wall carbon nanotubes (SWNTs) were also reported by Iijima [27], and by Bethune [28]. SWNTs have a simpler structure that opened a door to produce novel electronics based on the characteristics of these carbon nanotubes (CNTs) that were experimentally proven in 1998 [29].

2.1.2 Structures and Main Types

A SWNT is a one-dimensional graphene sheet rolled into a cylindrical shape within a diameter of about 1-2 nm [27]. Double wall carbon nanotubes (DWNTs) have a morphology and properties similar to those of SWNTs but with significantly enhanced chemical resistance [30]. MWNTs consist of concentric cylinders of 10-80 nm in diameter formed by multiple wrapped graphene sheets with a ≈3.3 Å interlayer distance [31]. The rolled graphene sheet of these nanotubes is characterized by a repeated hexagonal pattern that consists of covalently bonded carbon atoms [32]. Each C atom forms three strong sp^2 hybridized covalent bonds (σ-bonds) with three neighbouring atoms that have intersection angles of 120º. This sp^2 hybridization combines a 2s orbital with two 2p orbitals in the carbon atom. However, the third 2p orbital forms a relatively weak π-bond, which is commonly used for covalent functionalization of a MWNT with external molecules. The three strong σ-bonds are mainly responsible for the unique properties of SWNTs and MWNTs [30].

Although CNTs are cylindrical, they have many different structures that depend on how the graphene sheet has been rolled. Figure 2.1 shows the honeycomb lattice of graphene folded into different types of CNT, directed by the orientation of the two unit vectors $\boldsymbol{a_1}$ and $\boldsymbol{a_2}$. The lattice or chiral vector $\boldsymbol{c} = n\boldsymbol{a_1} + m\boldsymbol{a_2}$ is expressed using two integers n and m. The CNT structure is identified through the chiral angle (θ) between the $\boldsymbol{c}$ and $\boldsymbol{a_1}$ vectors (0^o-30^o). The electronic properties of CNTs changes significantly with the chiral vector from conducting to semiconducting [33].

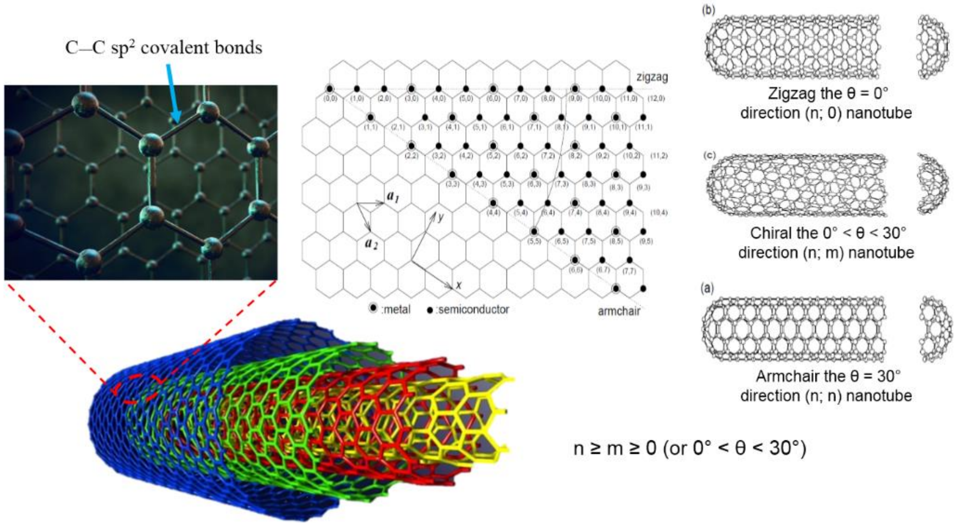

Figure 2.1: Different structures of CNTs.

Armchair and zigzag nanotubes are two cases of achiral nanotubes while chiral nanotubes have a unique structure (Figure 2.1). The naming originates from the shape of the cross-sectional ring as the armchair structure has the chiral directions (n, n); chiral angle

(θ) = 30° with metal like conductivity whereas the zigzag structure has chiral directions (n, 0); chiral angle (θ) = 0° with semi conducting properties, and the chiral structure has chiral directions (n, m); chiral angle (θ) = $0° < \theta < 30°$ [34]. The CNT radius (r_{CNT}) and chiral angle (θ) are determined from the following expressions (where r_o denotes the equilibrium bond length ≈ 0.1421 nm) [30],

$$r_{CNT} = \frac{\sqrt{3}r_0}{2\pi}\sqrt{n^2 + mn + m^2} \quad , \tag{2.1}$$

$$\theta = \cos^{-1}\frac{2n + m}{2\sqrt{n^2 + mn + m^2}} \quad . \tag{2.2}$$

2.1.3 Unique Properties and Wide Applications

The electrical properties of CNTs are influenced by their chirality (n, m) and tube diameters. CNTs can either be metallic, or semiconducting with small and large band gap [30]. Typically MWNTs are metal-like with a measured electrical resistivity of 10^{-4} to 10^{-3} Ω cm [34] with a current carrying capacity up to 10^{9} A cm^{-2}, which is 1000 times greater than that of copper [13, 35]. Because of their unique shape and structures, CNTs have an exceedingly higher longitudinal thermal conductivity than graphite [30]. CNTs have high thermal conductivities in the range of 1750–5800 W m^{-1} K^{-1} at room temperature, which is next to pure diamond [34]. These nanotubes have high thermal stability up to ~2800 °C in vacuum and ~750 °C in air [31, 35]. CNTs also have a high surface area (200-900 m^{2} g^{-1}), low density (1-2 g cm^{-3}), and superior mechanical properties. The reported high tensile strength and Young’s modulus for SWNTs has been as high as 150 GPa and 1.8 TPa, respectively, and for MWNTs up to 100 GPa and 1.0 TPa, respectively [13, 31, 34]. CNTs have many applications, including in sensors [36, 37], fuel storage [38, 39], high-strength materials, conductive suspensions [40], scanning microscopy tips [34], nanoelectronics [41, 42], and biomedicine [43-46].

2.1.4 Synthesis Methods

Originally, CNTs were produced through arc discharge, which is considered to be the oldest production method for these nanotubes [47]. Recently, chemical vapour deposition (CVD) techniques have replaced other methods due to several advantages, including the ability for large scale production, large growth areas, production of higher purity, aligned and longer CNTs, and lower cost. During the CVD process, hydrocarbon gases (e.g. ethylene) are decomposed on a hot catalytic metal substrate (~1000˚C) inside a reactor at atmospheric pressures to sustain CNT growth on the metallic catalyst. The catalyst can be introduced as a solid, deposited on a substrate (e.g. Si, SiO_2, or glass), or injected as a gas (that is fed with the reactants) [48-50]. A high magnetic field (10 T) can be used to provide control over the CNT morphology [51]. Currently, plasma enhanced CVD has replaced thermal-based CVD, since it is able to reduce the decomposition temperature of the hydrocarbon gas (~550 ˚C) [49, 50, 52].

2.1.5 Key problems of CNTs

A CNT is an anisotropic material with a one dimensional structure. Typically, commercially available CNTs are entangled and randomly orientated because of the van der Waals attractions between individual CNTs and/or Brownian motion in the dispersing medium. The randomness for highly anisotropic material reduces their application efficiency [53-56]. CNTs are diamagnetic materials, like graphite, which has a diamagnetic susceptibility χ of 10^{-5} emu g^{-1} [57, 58]. Furthermore, CNTs are hydrophobic because of their non-polar honeycomb structure, which prevents the formation of hydrogen bonds with water molecules. This hydrophobicity reduces the compatibility of CNTs with many dispersing mediums, including polar solvents and polymers [59, 60]. Finally, CNTs are commercially produced in the powder form and their manipulation and control at the micro and macro scale is a practical challenge that limits their applications.

2.2 Carbon Nanotubes Functionalization

Functionalization is defined as the introduction of external molecular groups onto CNT in order to modify a certain physical and chemical properties [14]. The bonding between a CNT and an external molecule could be of either chemical (e.g. covalent) or physical (e.g. van der Waals force) nature. Functionalization offers a method to chaperone CNTs, e.g. functionalization with a magnetic nanoparticle can provide a way to control and manipulate the now magnetic CNT from a distance. Also, active functional groups such as carboxylic acid can enhance CNT compatibility with dispersing mediums [61].

2.2.1 Non-Covalent Functionalization

This method is based on utilizing weak bonds like the Van der Waals force between a CNT surface and an external molecule. Mild reaction conditions do not affect the CNTs surface significantly, which is a significant advantage [62]. The non-covalent functionalization can be done through several techniques including biological, metal and polymer functionalization.

Bio-functionalization creates bioactive CNTs by the conjugation of bio materials such as DNA or proteins to the CNT wall, e.g., for biosensing, drug carriers [15, 62-64] and in artificial muscles [65]. The polymer functionalization induces Van der Waals force to wrap polymer chains around CNT walls [66]. Endohedral functionalization is another non-covalent method where external molecules are encapsulated inside the CNT driven by the capillary effect [66]. Metallic functionalization is performed by depositing a metal nanoparticle, such as Au, Ag or Ni, onto the outer surface of a CNT [62]. Attentions has been focused on electroless plating since it produces a more uniform and less porous layer over irregular and tiny surfaces than conventional electroplating [67].

2.2.2 Covalent Functionalization

While CNTs are inherently inert due to the stable sp^2 hybridized C-C σ bonds, they usually contain defect sites, which occur during production and mechanical loading. Local bonds destabilize at these defect sites, making the CNTs susceptible to attack by reactive molecular groups [14]. For instance, surface oxidation with HNO_3 [16, 61, 68-72], (HNO_3 / H_2SO_4) [73-80], and (HNO_3 or H_2SO_4 / H_2O_2) [69, 71] leads to the formation of COOH, C=O, and C–OH groups [61, 81] that are covalently linked to the CNT scaffold. These functional groups can be attached to nanoparticles (NPs) through an additional step, where the covalent bond could be formed directly by changing the C atom hybridization from sp^2 to sp^3 or indirectly by chemical transformations of previously generated functional groups. However, this method produces a strong bond and widespread surface destruction leading to large defective surface areas [62, 65, 66, 82].

2.3 Magnetism and Magnetic Nanomaterials

CNTs can be functionalized with magnetic nanoparticles using both methods of functionalization discussed previously. This offers a practical way to remotely control and manipulate CNTs inside different dispersing mediums utilizing external magnetic field. The following section presents a background on magnetism and magnetic nanomaterials.

2.3.1 The magnetic moment

An electric current passing through a wire generates a magnetic field (Ampère's law). In a steady electric field, the curl of the magnetic field ***H*** equals the electric current density ***J*** ($\nabla \times \boldsymbol{H} = \boldsymbol{J}$) [83, 84]. However, when a current $I = q\ (\omega/2\pi)$, with charge q and an angular frequency ω passes through a finite loop of area $A = \pi\ r^2$, it produces a magnetic moment of ***m***, where,

$$\boldsymbol{m} = \int dm = I \int dA = \frac{q\ r^2 \boldsymbol{\omega}}{2}\ . \tag{2.3}$$

Similarly, the circulation of an electron (Figure 2.2) with charge $q = -e$, mass of m_e, and velocity $\boldsymbol{v} = \boldsymbol{\omega} \times \boldsymbol{r}$, produces an orbital angular momentum ($\boldsymbol{l}$, (2.4)) and orbital magnetic moment ($\boldsymbol{m_o}$, (2.5)) [85, 86]:

$$\boldsymbol{l} = m_e(\boldsymbol{r} \times \boldsymbol{v}) = m_e\ r^2 \boldsymbol{\omega}, \tag{2.4}$$

$$\boldsymbol{m_o} = -\frac{e\ (\boldsymbol{r} \mathrm{x} \boldsymbol{v})}{2} = -\ \frac{e.\boldsymbol{l}}{2m_e}\ . \tag{2.5}$$

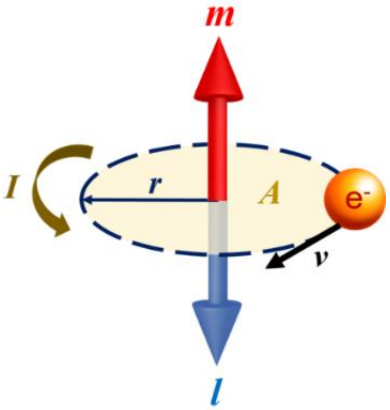

Figure 2.2: A current passing through a loop produces a magnetic moment ***m*** and angular momentum ***l***.

The value of the orbital magnetic moment ‹$\boldsymbol{m}^{z}{}_{o}$› can be expressed by quantizing the angular momentum ***l*** along a quantization direction of z as follows (2.7) [85, 87]:

$$\langle \boldsymbol{l}_z \rangle = \hbar\, l_z, \text{ and} \tag{2.6}$$

$$\langle \boldsymbol{m}^{z}{}_{o} \rangle = -\frac{e.\hbar}{2m_e} l_z = -\frac{\mu_B}{\hbar}\langle \boldsymbol{l}_z \rangle , \tag{2.7}$$

where l denotes the integer quantum number of the angular momentum, $\hbar$ is the reduced Planck constant (1.055×10^{-34} J s), and Bohr magneton μ_B is the unit that expresses the electron magnetic moment.

$$\mu_B = -\frac{e\hbar}{2m_e} = 9.27 \text{ x } 10^{-24} \text{ J/T}. \tag{2.8}$$

While undergoing orbital spin, the electron also spins around its axis, which is enough to produce a full Bohr magneton with only half $\hbar$. The electron spin produces a spin magnetic moment of $\boldsymbol{m}_s$ and spin angular momentum of ***s*** [85, 87].

$$\langle \boldsymbol{m}^{z}{}_{s} \rangle = -2\frac{\mu_B}{\hbar}\langle \boldsymbol{s}_z \rangle , \text{ where } \boldsymbol{s}_z = \pm\frac{\hbar}{2}. \tag{2. 9}$$

Finally, the total magnetic moment of the electron is the summation of its orbital and spin quantized magnetic moments [85, 87, 88], i.e.,

$$\langle \boldsymbol{m}^{z}_{\mathrm{Total}} \rangle = \langle \boldsymbol{m}^{z}_{o} \rangle + \langle \boldsymbol{m}^{z}_{s} \rangle = -\frac{\mu_B}{\hbar} \langle 2\langle \boldsymbol{s}_z \rangle + \langle \boldsymbol{l}_z \rangle \rangle . \tag{2.10}$$

2.3.2 Magnetic dipole

A magnetic pole is fictitiously defined as a magnetic point that has a charge (p) located at the magnet edge and concentrates the magnetic force. A magnetic dipole represents the interaction between two equally opposite magnetic charges ($+p$, $-p$) separated by a distance r [85, 89]. Similar to coulombic interaction, two poles of strengths p_1 and p_2 respectively act on each other with a magnetic force $\boldsymbol{F}(r)$,

$$\boldsymbol{F}\left(r\right) = \frac{p_1 p_2}{4\pi\mu_0 r^2} , \tag{2.11}$$

where μ_0 is the free space permeability and it equal $4\pi \times 10^{-7}$ Wb A^{-1} m^{-1} [87, 89].

For a finite distance between the two poles, the force is a measure for the magnetic field at any external point with a position vector $\boldsymbol{r}$. However, for any pole of strength p, the relation between the acting force and the magnetic field $\boldsymbol{H}(r)$ is [85, 87]:

$$\boldsymbol{F}(r) = p\, \boldsymbol{H}(r), \text{ and} \tag{2.12}$$

$$\boldsymbol{H}\left(r\right) = \frac{p}{4\pi\mu_0 r^3} \boldsymbol{r} . \tag{2.13}$$

Finally, magnetic dipoles always consist of two opposite magnetic charges where all flux lines that are produced from one pole always return to the opposite pole (Maxwell's equations (2.14)) [85, 88].

$$\nabla \bullet \boldsymbol{B} = 0 . \tag{2.14}$$

2.3.3 Magnetic Parameters

The magnetic field strength H depends on the separation distance between the field lines. An external field $\boldsymbol{H}$ with a uniform strength is able to act on a magnetic dipole (p) with force coupling that results in a torque $\boldsymbol{\Gamma} = pr\boldsymbol{H}\sin\theta$, as shown in Figure 2.3 [87, 89].

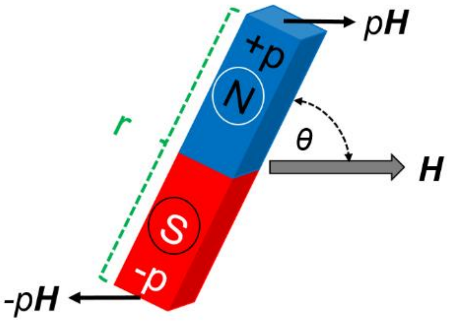

Figure 2.3: A magnetic field $\boldsymbol{H}$ apply a torque $\boldsymbol{\Gamma}$ on a magnetic dipole.

The coupling between the dipoles and the applied field produces the magnetization ($\boldsymbol{M}$, J T^{-1}) and magnetic induction ($\boldsymbol{B}$, T). The magnetization ($\boldsymbol{M}$) is a measure of the generated magnetic field from the magnetic material and equals the net dipole magnetic moment per volume density (2.15). It has a direction that polarizes under the effect of the applied field [87, 89]. The induction ($\boldsymbol{B}$) is the density of magnetic flux lines ($d\boldsymbol{\Phi} = \boldsymbol{B}dA$). It is considered as a measure for the magnetic material response. However, $\boldsymbol{B}$ has a linear relationship with $\boldsymbol{H}$ in vacuum (2.16), and with ($\boldsymbol{H}$+$\boldsymbol{M}$) inside any magnetic matter (2.17) [85-88],

$$\boldsymbol{M} = \boldsymbol{m}\frac{N}{V}, \tag{2.15}$$

$$\boldsymbol{B} = \mu_0 \boldsymbol{H}, \tag{2.16}$$

$$\boldsymbol{B} = \mu_0(\boldsymbol{H} + \boldsymbol{M}). \tag{2.17}$$

The magnetic susceptibility χ (2.18) and permeability μ (2.19) are considered to be parameters that quantify the magnetic response of any material [84, 86-88]:

$$\boldsymbol{M} = \chi \boldsymbol{H}, \tag{2.18}$$

$$\boldsymbol{B} = \mu \boldsymbol{H}. \tag{2.19}$$

2.3.4 Magnetic Domains

Because of magnetic anisotropy, magnetic materials tend to obtain a homogenous magnetization directed into their crystal easy axis for very small domains (size of a few nm), but not for bigger domains. The self-created magnetostatic energy increases with the domain size which is not favourable. The material tends to reduce its high energy by reducing the external path length of the magnetic field loop by dividing the large domain into smaller multidomains. The total magnetization is the sum of the moments of all created mini-domains. The domain division also creates a domain wall where adjacent molecules have net magnetic moments with different directions [85, 87, 88]. Domain Walls are classified according to the angle between the magnetization of adjacent domains into 180˚ wall and 90˚ wall (Figure 2.4) [88].

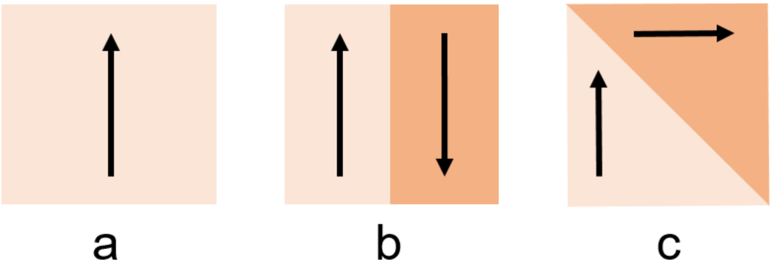

Figure 2.4: Domain walls. (a) single domain. (b) 180˚ domain. (c) 90˚ domain.

2.3.5 Magnetization Hysteresis Loop

Magnetic hysteresis is an irreversible phenomenon that represents the magnetization and demagnetization of any magnetic material (Figure 2.5). An applied magnetic field facilitates the motion of domain walls against the crystal imperfections until all magnetic moments are completely directed into their crystal's easy axis, which is aligned close to the field direction. Consequently, the magnetic material becomes a single domain. A field with high enough strength can rotate this single domain from its easy direction into a direction parallel to it. At magnetic saturation (M_s), removal of the applied field retains magnetization inside the material, which is called the remnant magnetization (M_r). The field required to reverse this process and reduce the remnant magnetization to zero is called the coercive field (H_c) [87, 89].

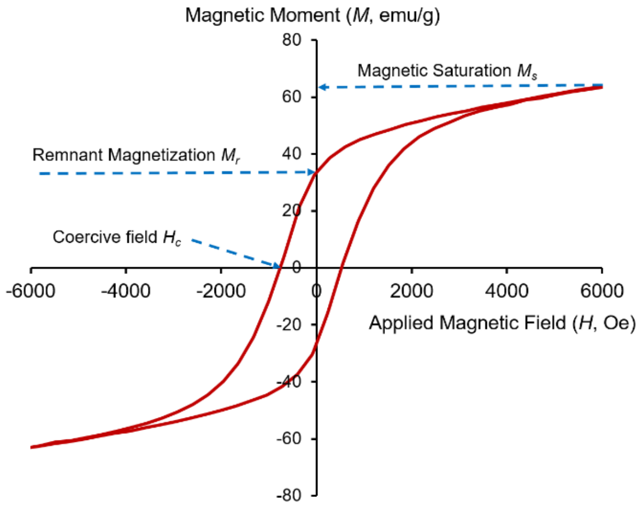

Figure 2.5: Magnetization Hysteresis Loop.

2.3.6 Classification of Magnetic Materials

Pure elements in the periodic table are classified at room temperature according to their bulk permeability into diamagnetic, paramagnetic, ferromagnetic, and antiferromagnetic materials as shown in Figure 2.6. Diamagnetism is the weakest form of magnetism where the magnetization is proportional to the applied magnetic field. Diamagnetic materials such as carbon and noble gases have a negative and very weak relative permeability. Paramagnetic materials such oxygen have a low and positive relative permeability. Antiferromagnetism exists only in chromium, where equal magnetic moments are antiparallel in a way that produces almost zero net magnetization [86-89].

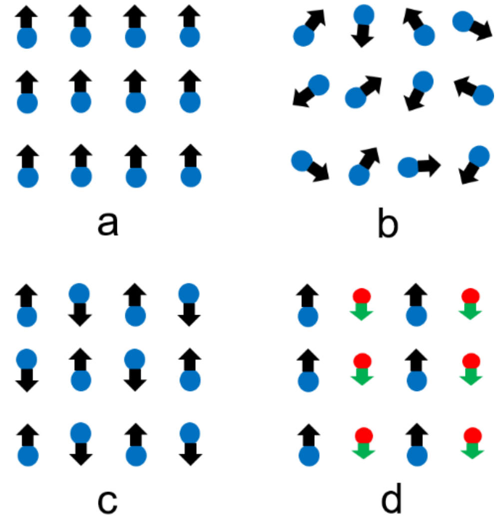

Figure 2.6: Different types of magnetism. (a) Ferromagnetism. (b) Paramagnetism. (c) Antiferromagnetism. (d) Ferrimagnetism.

Nickel, iron, and cobalt are the only three pure elements that are ferromagnetic. They have high positive relative permeability (10^2-10^5) so that all magnetic moments are equal and parallel. Ferrimagnetism is another type of magnetism that does not occurs in pure elements. Ferrimagnetic materials are known as ferrites, which are typically complex magnetic oxides that contain ferric oxide (Fe_2O_3) as their basic magnetic component. Ferrimagnetism is a special type of antiferromagnetism where antiparallel magnetic moments are not equal [86-89].

For ferromagnetic and ferrimagnetic materials, reducing particles sizes below a critical dimension (D_c, 15-150 nm) changes the material containing multimagnetic domains into a single domain (Figure 2.7) [1, 90]. Superparamagnetism is a special case of such a material when the particle size is lower than the superparamagnetic diameter (D_s, few nm). In this case, the particle consists of a small single domain that can be conceived as a single massive paramagnetic atom. Here, the coercivity is zero and upon removal of the applied field there is no residual magnetization inside the material [85, 91, 92].

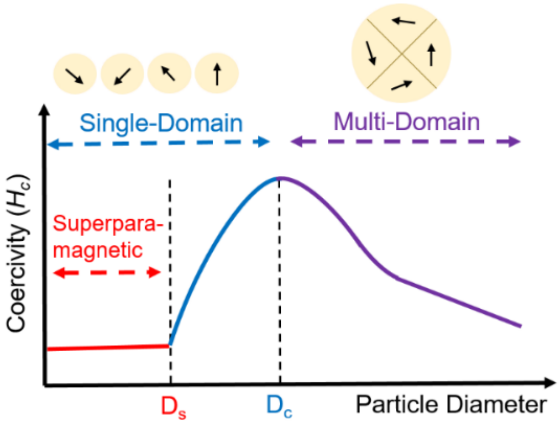

Figure 2.7: The relation between the coercivity and the particle size.

2.3.7 Magnetic Nanomaterials

Any material with a dimension less than 100 nm that responds to a magnetic field is considered to be a magnetic nanomaterial. These nanomaterials, such as metals and spinel ferrites, which feature a higher surface-to-volume ratio than micromaterials, are synthesized through several physical and chemical methods [93, 94]. Metals (e.g. Fe, Ni, and Co) have high magnetization, high density (~8 g.cm^{-3}) and low oxidation stability [1]. Spinel ferrites (i.e. Fe_3O_4) are easy to synthesis and have less prominent, but tunable, magnetic properties, lower density (~5 g cm^{-3}), higher stability. Spinel ferrites have a general chemical formula of $MO.Fe_2O_3$ and a crystal structure similar to naturally occurring spinel ($MgAl_2O_4$), where M denotes a divalent metal (e.g. Fe^{2+}, Mn^{2+}, and Zn^{2+}) [89]. Because of their small sizes (few nm), magnetic nanoparticles (MNPs) are expected to be individually superparamagnetic [92].

2.4 Magnetization of Carbon Nanotubes

Magnetization of CNTs occurs when magnetic nanoparticles (MNPs) are attached to the surfaces of the CNTs via either covalent or non-covalent functionalization. Introduction of MNPs with a high relative permeability to a diamagnetic material that has almost zero permeability produces a hybrid material with intermediate magnetic properties. Magnetization is a suitable way to align and manipulate CNTs under an applied magnetic field e.g., by immersing them in a liquid prepolymer containing dispersed magnetized CNTs (mCNTs) as it experiences an applied magnetic field [95, 96]. The magnetic nanoparticles that attach to a CNT surface provide new surfaces that are more compatible with dispersing mediums. They can be used to overcome the high contact electric resistance that arises due to the anisotropic behaviour of CNTs, and enhance their mechanical properties by assisting with mechanical load transfer [97].

In bulk materials, the superior properties of CNTs can be leveraged by dispersing them in a continuous matrix to form a nano-composite [53, 98]. Since CNTs are a quasi-one dimensional, their properties are best exploited by aligning them along their longitudinal axes [54, 99, 100]. mCNTs are utilized in many applications including wastewater treatment [101, 102], phase separation [103], biomedical applications [104], drug carriers [63, 105], and microwave absorbers [106-108].

2.4.1 Magnetization by Encapsulation

The stable crystalline structure of the CNT walls can be used to protect encapsulated materials so that they can be used as carrier systems for many nanomaterials, including magnetic nanoparticles [109]. During CVD, a CNT can be filled with a metal [110-116] or an oxide [117]. Utilizing capillary action to fill colloidal suspensions of nanomaterials is less expensive [109, 118], e.g., using magnetic assistance to accelerate encapsulation [118-121].

2.4.2 Magnetization by Surface Decoration

2.4.2.1 Co-Precipitation Method

Coprecipitation is the common synthesis methodology for nanocrystalline spinel ferrites. Mixed cations of hydroxide are coprecipitated from their aqueous ionic solution using a precipitant (e.g. ammonia) and then decomposed thermally into their corresponding oxides. Coprecipitation performed at room temperature and under atmospheric conditions produces homogenous, pure and fine nanoparticles [89, 122].

Magnetic CNTs have been produced by the covalent attachment of MNPs to the external walls of CNTs. Covalent functionalization commonly proceeds by first treating CNTs with acids, such as concentrated nitric acid HNO_3 [16, 61, 68-72], or a mixture of concentrated nitric and sulfuric acids [73-80]. Composite Fe_3O_4-CNTs have been produced by co-precipitating Fe_3O_4 nanoparticles on the CNT surfaces from an aqueous solution, such as one containing Iron (II, III) chloride [104, 123-126] or Iron sulphates [101-103, 124, 127, 128]. During the process, a precipitant is slowly introduced with the assistance of sonication to adjust the pH at 9-12. The common precipitant for Fe_3O_4 nano-particles is (30%) ammonia solution [102, 122, 127-130] and NaOH solution [104, 131-133]. Other MNPs such as maghemite (γ-Fe_2O_3) [123, 134, 135], and $M^{2+}Fe_2O_4$ (M^{2+} = Mn, Co, Ni, Cu, or Zn) [136-138] have been coprecipitated on CNTs.

2.4.2.2 Electroless Deposition

Surface treatment of CNTs with a metallic coating is a method of magnetization that improves their oxidation resistance [99], minimizes the ohmic contact resistance [139], increases CNT wettability, adhesion to polymers and assists in the transfer of mechanical loading [97]. Nanotubes can be coated with metals using electroless plating [97], a method which is applicable to many substrates [140]. The resulting metal-CNT hybrid (MCH) nanomaterial has a relatively high surface area, low electric contact resistance [141], superior hardness, wear resistance and magnetic properties [142]. MCHs are used in reinforced composites, sensors [143], catalytic and electrochemical applications [141]. Nickel is commonly used as a ferromagnetic plating material [144]. Electroless Ni deposition forms weak noncovalent bonds that utilize van der Waals forces, between the outer surface of the CNT and its surrounding metallic nanolayer [62]. The metal materializes from an ionic solution subjected to an in situ reduction reaction [145]. Nickel chloride is used as the source of metal ions [146]. A reducing agent, sodium hypophosphite, provides the electrons required to reduce nickel ions (Ni^{2+}) into metallic nickel (Ni) [147] using a catalyst [148]. To constrain the reaction on the CNT surface, the CNTs must be pre-treated with a catalyst prior to depositing Ni on their surfaces. The deposit forms a continuous Ni layer that encapsulates the CNTs [149].

The catalysis consists of sensitizing and activating steps. Tin ions (Sn^{2+}) are used for CNT sensitization and palladium ions (Pd^{2+}) for activation [99, 140]. Sn^{2+} adsorbs on the CNT surface during sensitization and reduces Pd^{2+} to Pd during subsequent activation. Pd initiates the reduction reaction that deposits Ni on CNTs [148]. The electroless deposition is a redox process that consists of an oxidation reaction (2.20) for the reducing agent and a reduction reaction (2.21) for nickel ions [149, 150]. Sodium citrate is generally used to prevent Ni from complexing [147].

1. Oxidation $$H_2PO_2^- + H_2O \rightarrow H_2PO_3^- + 2H^+ + 2e^- \tag{2.20}$$
2. Reduction $$Ni^{2+} + 2e^- \xrightarrow[CNT\ surface]{Catalyst} Ni \tag{2.21}$$

2.5 Potential Applications for Magnetic CNTs

2.5.1 Carbon Nanotubes in Nanofluids

Nanofluids are colloidal suspensions of nanoparticles dispersed in a liquid [151]. Due to their superior electrical and thermal conductivities, CNTs have been introduced as the dispersed phase into nanofluids [29, 31, 152], some of which have been used as coolants [153] and as electrically conductive nanofluids [154]. When dispersed in an aqueous medium, as little as 0.5% (w/w) of CNTs can increase the electric conductivity by an order of magnitude [154].

As shown in Figure 2.8, the ions in the surrounding medium rearrange around the ends of the conductive MWNTs when they are polarized with an applied electric field $\mathbf{E}_a$. This shortens the ion transport path in the direction of polarization and decreases the effective electrical resistance of the colloidal suspension as per Coulomb's law [151, 155].

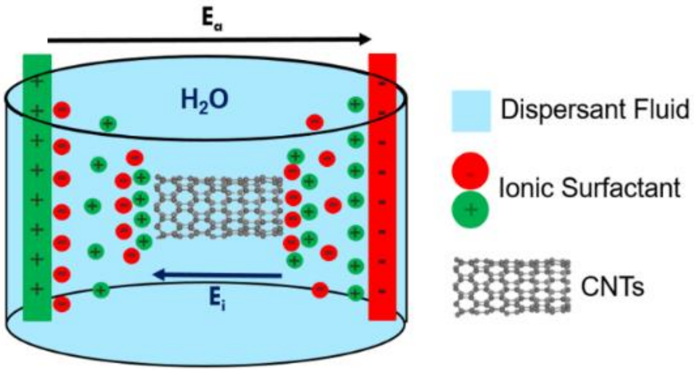

Figure 2.8: Polarization of CNTs placed in an ionic medium between two electrodes charged by an electric field E_a.

The effective thermal conductivity of a nanofluid is enhanced with increasing CNT loading [156]. Just 1-1.5 wt% of CNTs can increase the thermal conductivity of different liquids by threefold [153, 157], depending upon the suspension stability [158, 159]. Because of their high surface energy, high molecular weight, hydrophobicity and inertness of their outer surfaces, CNTs agglomerate into clusters that contain randomly oriented tubes, diminishing their dispersion in media [158]. Since aggregation depends primarily on the solution chemistry and surface charge [160, 161], it is ameliorated by decreasing the interparticle attractive force and raising the agglomeration energy of the particles [162], e.g., through ultrasonication [163] and chemical stabilization methods such as surface coating [164]. The coating layer could be with organic surfactants such as oleic acid, or ionic as tetramethylammonium hydroxide aqueous solution [162, 165, 166]. Whereas, precise manipulation of the nanotubes into fully aligned structures can be challenging [167], magnetization can provide a convenient solution for manipulating CNTs inside dispersing media as a response to an applied magnetic field [95, 96].

2.5.2 Carbon Nanotubes in Polymer Composites

Polymer nanocomposites are used as matrices because of their low density and tunable mechanical properties. Nanomaterials with a high surface area and tunable properties can be useful reinforcing fillers in composites [53]. As a filler, a small amount of CNTs can increase the electrical and thermal conductivity of a polymeric matrix with only a small increase in its density [54, 168]. For instance, a 1 wt% loading of MWNTs provides a 80% increase in the elastic modulus of polyvinyl alcohol [169], and a 1 wt% loading of single wall CNTs produces a 125% increase in the thermal conductivity of an epoxy polymer [170] while a 3% loading increases the thermal conductivity three fold [171]. Generally, composites based on aligned CNTs exhibit a higher electric conductivity [134], and thermal conductivity [171] than unaligned CNTs.

Because of Brownian motion, CNTs are randomly orientated in a polymeric matrix, which reduces their efficacy in enhancing bulk material properties [53-55]. Electric and magnetic fields can overcome the Brownian motion and assist in CNT alignment and manipulation [98, 168, 172, 173]. The poor magnetic susceptibility of CNTs requires a very strong magnetic field to produce a torque that exceeds their thermal energy (2.22) and the viscous resistance of the medium,

$$\Delta U \approx -m\left(\chi_{\parallel} - \chi_{\perp}\right)H^2 > \mathrm{k}T\,, \tag{2.22}$$

where U denotes the CNT potential energy, H the field strength, and m the mass of a CNT segment [55, 134]. As previously described, CNT functionalization with MNPs provides a means to enhance the magnetic susceptibility and therefore reduce the field strength required for their alignment (up to 0.2 T) [168, 172, 174].

3. Magnetizing MWNT via Covalent Functionalization

3.1 Introduction

In this chapter, an experimental investigations will be presented to highlight the magnetizing of the MWNT via covalent functionalization. Decorating the CNTs with magnetic nanoparticles (MNPs) facilitates their expedient organization with a magnetic field. One of the most convenient methods for their decoration is to first treat the CNTs with nitric or sulfuric acid, or a mixture of the two, and then co-precipitate MNPs in situ. Here, six variations of this protocol are compared to identify acid treatment influence on the decoration of multi-walled CNTs (MWNTs). Further, we explore means to tune the properties of these magnetic MWNT by varying the (1) MNP material composition, and (2) MNP:MWNT (w/w) magnetization weight ratio (γ). This chapter is reprinted and adapted with permission from *Diamond and Related Materials*, *Decorating carbon nanotubes with co-precipitated magnetite nanocrystals*, 66, **Ahmed M Abdalla**, Suvojit Ghosh, and Ishwar K Puri, Copyright 2016 and, from *Journal of Magnetism and Magnetic Materials*, *Magnetoresponsive conductive colloidal suspensions with magnetized carbon nanotubes*, 421, **Ahmed M Abdalla**, Abdel Rahman Abdel Fattah, Suvojit Ghosh, and Ishwar K Puri, Copyright 2017 and, with permissions from Elsevier. The author of this thesis is the first author and main contributor of the above mentioned publications and has conducted all the experiments. The chapter will provide a literature review which is discussed in the background information section, followed by excerpts from the above mentioned papers to emphasize some of the concepts disused below.

3.2 Background Information

The superior mechanical strength, and electrical and thermal conductivities of carbon nanotubes (CNTs) can be leveraged in bulk materials by embedding the nanotubes in a continuous matrix to form a nano-composite [53, 98, 175]. Since CNTs are quasi-one dimensional, their properties are best manifested in the bulk if they are aligned along a particular direction in the matrix [54]. Such alignment is easily implemented when the CNTs are magnetized (mCNTs). For instance, a polymer can be dissolved in a solvent that contains dispersed mCNTs, then solution-cast in the presence of an applied magnetic field [95, 96]. Herein, the field aligns the mCNTs, and the orientation is preserved by the solution-cast polymeric matrix.

Nanotubes can be magnetized in several ways, e.g., by encapsulating magnetic nanoparticles (MNPs) within them [109, 110, 115, 117-119, 176], plating them with a ferromagnetic metal [99, 139, 140, 177, 178], or decorating them with MNPs [135-138, 179-181]. Decoration is the most convenient route. Unlike encapsulation, which requires sophisticated *in situ* chemical vapor deposition (CVD) [109, 110, 117] with precise templates [115, 118, 119], and plating that requires expensive reagents [99, 139, 140, 177, 178], decoration uses inexpensive reagents and commonly available laboratory apparatus.

CNTs are inherently inert due to their stable sp^2 hybridized C-C σ bonds. However, they typically feature defect sites that are created during production and/or due to mechanical loading. At such defect sites, the local C-C bonds become destabilized and are susceptible to attack by reactive molecular groups [75, 182]. These structural defects are exploited to decorate CNTs. For instance, treatment with HNO_3 [71, 72], HNO_3 and H_2SO_4

[72, 80], or H_2SO_4 and H_2O_2 [69, 71], leads to surface oxidation at the defect sites, forming COOH, C=O, and C–OH functional groups that are covalently linked to the CNT scaffold [61, 183]. These functional groups form the sites where MNPs are attached to the CNT.

Various chemical routes for decoration have been developed, e.g., hydrothermal decomposition of iron compounds [105, 126, 184], surface imprinting of magnetite (Fe_3O_4) nanograins [125], and *in situ* co-precipitation of ferrite nanocrystals [101-104, 124, 127, 128, 185, 186]. Co-precipitation can be performed at room temperature and under atmospheric conditions. In contrast, hydrothermal processes employ high temperatures (~250 °C) and an inert atmosphere [184], while surface imprinting requires a sealed autoclave, also at high temperatures (~200 °C) over a long duration (~10 h) [125]. Thus, co-precipitation is by far the most convenient method for decorating CNTs with MNPs.

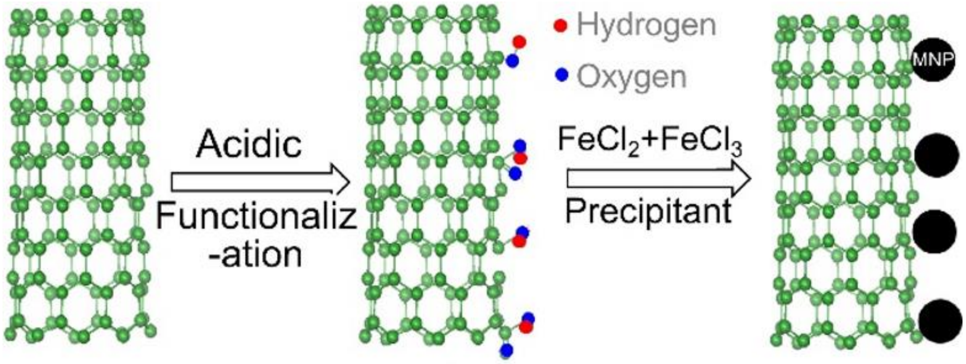

Figure 3.1: Magnetizing CNTs by coprecipitation. When CNTs are treated with strong oxidizing acids, COOH, C=O, and C–OH groups are formed at defect sites. In the presence of Fe^{+2}, Fe^{+3} and a precipitating base, they serve as nucleation sites for magnetite (Fe_3O_4) nanocrystals.

Magnetic decoration through co-precipitation is performed in two steps (Figure 3.1). First, the CNTs are treated with strong oxidizing acids, such as HNO_3 and H_2SO_4.

Herein, the NO_3^- and HSO_4+ radicals attack the weak C-C bonds at the CNT defect sites to produce functional groups, e.g., COOH, C=O, and C–OH. Next, these groups act as the nucleation sites for magnetite (Fe_3O_4) nanocrystals that are coprecipitated (3.1) from a solution of Fe^{2+} and Fe^{3+} ions [128, 181]. Many variations in the co-precipitation routes to decorate CNTs with MNPs have been reported, but these routes have yet to be compared to identify best practices. We fill this gap by examining (1) how use of two acids, HNO_3 and H_2SO_4, and their mixture influences the decoration produced on multi-walled CNTs (MWNTs), and (2) if filtration, washing and drying of MWNTs after acid treatment can be eliminated to prevent material loss to the filtrate and thus increase the yield of magnetized MWNTs (mMWNTs). Further, we explore means to tune the properties of these mMWNT by varying the (1) MNP material composition, and (2) MNP:MWNT (w/w) magnetization weight ratio (γ).

$$FeCl_2 + 2FeCl_3 + 8NH_4OH \rightarrow Fe_3O_4 + 8NH_4Cl + 4H_2O \,. \tag{3.1}$$

3.3 Methodology

3.3.1 Materials and Reagents

Multiwall carbon nanotubes (MWNTs) produced by CVD with purity > 95%, outside diameters of 20-30 nm, inside diameters of 5-10 nm and lengths between 0.5-2.0 µm, were purchased from US Research Nanomaterials. Other reagents used were ferric chloride hexahydrate ($FeCl_3 \cdot 6H_2O$, 97-102%, Alfa Aesar), ferrous chloride tetrahydrate ($FeCl_2 \cdot 4H_2O$, 98%, Alfa Aesar), copper II chloride ($CuCl_2$, 98%, Alfa Aesar), tetramethyl ammonium hydroxide ($C_4H_{13}NO \cdot 5H_2O$, 98%, Alfa Aesar), manganese II chloride tetrahydrate ($MnCl_2 \cdot 4H_2O$, 99%, Sigma Aldrich), zinc chloride ($ZnCl_2$, 99%, Sigma

Aldrich), sodium hydroxide (NaOH, 97%, CALEDON Laboratory Chemicals), nitric acid (HNO_3, 68-70%, CALEDON), sulfuric acid (H_2SO_4, 95-98%, CALEDON) and ammonium hydroxide (NH_4OH, 28-30%, CALEDON). All reagents were used as received without further purification.

3.3.2 Acid-enabled Functionalization

For each sample, 1 g of MWNTs was first dispersed in 200 ml of concentrated acid and sonicated for 4 h in a sonication bath (VWR International, Model: 97043-936). The MWNTs were subsequently washed three times by diluting the dispersion in 500 ml of deionized (DI) water, allowing the MWNTs to settle (~20 h) and then decanting the supernatant. After three washes, the solution pH ≈ 2, after which it was filtered, washed several times and finally dried. Six variations of this route were probed, as illustrated in Figure 3.2, yielding the six samples S1-S6.

Briefly, concentrated HNO_3 was used for S1 and S4, H_2SO_4 for S2 and S5 and a 1:1 (v/v) mixture of HNO_3 and H_2SO_4 for S3 and S6. For samples S4-S6, the filtration, washing and drying steps subsequent to acid functionalization were eliminated to prevent the loss of MWNTs to the filtrate. In these cases, excess NaOH was employed to neutralize the excess acid and to also induce co-precipitation of MNPs. Thus, the magnetite (Fe_3O_4) co-precipitation reaction occurred in a dilute acid medium. Routes S2 and S4-S6 are new and hitherto unexplored.

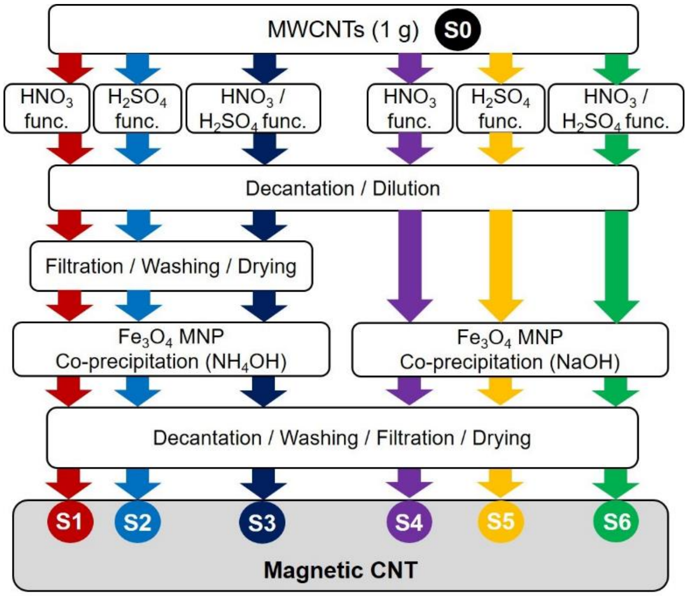

Figure 3.2: Schematic of the synthesis routes showing the variations used to produce the six samples, S1-S6. Since intermediate filtration leads to the loss of MWNTs that are shortened due to the damage caused by the acid, for routes S4-S6 the acid functionalization process is ceased after the sample has been decanted and diluted, i.e., co-precipitation is induced without any filtration or drying of the acid-treated MWNTs.

3.3.3 Decoration

Based on stoichiometric calculations to obtain a 1:1 (w/w) mixture of Fe_3O_4:MWNTs, 2.3 g of $FeCl_3 \cdot 6H_2O$ and 0.9 g of $FeCl_2 \cdot 4H_2O$ were first dissolved in 400 ml DI water for each sample. Prior to dissolving the salts, the water used was carefully degassed by boiling and sonication in order to prevent the formation of maghemite (γ-Fe_2O_3) and hematite (α-Fe_2O_3) by dissolved oxygen [187, 188]. The acid-treated MWNTs were dispersed in the solution using ultrasonic treatment for 10 mins with a probe sonicator (Qsonica, Model: Q500 with 1/4″ micro-tip at 35% power) and subsequently for 50 minutes in a sonication bath at 50˚C (VWR International, Model: 97043-936). The precipitant was slowly introduced during the second sonication step until the pH reached 10. For samples S1-S3, 30% ammonia solution was used as the precipitant. The higher acidity (pH ≈ 2) of samples S4-S6 required the use of a stronger base, 0.2 M NaOH, as a precipitant [131-133, 189]. After co-precipitation, the samples were settled through magnetic sedimentation and washed with DI water multiple times until the supernatant reached a pH ~ 7. Thereafter, the samples were washed using ethanol, filtered and then dried in a vacuum oven at 70 °C for 1 hr. The dried samples were strongly magnetic.

3.3.4 Influence of MNPs Concentration and Chemical Composition

Employing the process for the production of sample S1 described in section 3.3.3, stoichiometric calculations for different samples (S1, S1.2, S1.3, S1.4, and S1.5) were conducted to obtain different Fe_3O_4:MWNT (w/w) magnetization weight ratio $\gamma = 1, 1.25, 1.5, 1.75$ and 2. The effect of changing magnetization ratio γ on the uniformity and density of decoration was observed through transmission electron microscopy (TEM) images.

For the magnetization weight ratio γ of unity, the magnetite nanoparticles in S1 with a relatively high Curie temperature [190] were replaced with $Mn_{0.2}Cu_{0.20.6}Fe_2O_4$ to produce sample S1m and with $Cu_{0.4}Zn_{0.6}Fe_2O_4$ to make S1c, since both of the latter MNPs have lower Curie temperatures [191, 192]. For S1m and S1c, we used Mn^{+2}, Cu^{+2}, and Zn^{+2} chloride salts for co-precipitation and NaOH as the precipitant [193, 194], and the MWNTs and salt solution were dropped into the precipitant instead of *vice versa* [193]. SQUID magnetometry provided changes in the magnetic properties of the mMWNTs, X-Ray diffraction (XRD) revealed the material phases and MNP crystal sizes. TEM and energy-dispersive X-ray spectroscopy (EDX) were used to visualize the mMWNTs, the uniformity and density of their decoration with MNPs, and to identify their elemental composition.

3.3.5 Characterization Methods

The elemental composition of acid-treated MWNTs was determined using a PHI Quantera II Imaging and Scanning X-Ray Photoelectron Spectrometer (XPS). X-Ray Diffraction (XRD) analysis of MWNT and mMWNT powder samples was performed using a Bruker D8 Discover instrument comprising a DavinciTM diffractometer operating at 35 kV and 45 mA using Co-Kα radiation (λavg = 1.79026 Å). Bruker's DIFFRAC.Eva V3.1 and TOPAS softwares were used for the analysis and semi-quantitative estimation of the sample composition. For samples S1-S3, the semi-quantitative analysis was verified using a digital weighing balance. The sample weights were recorded three times during the synthesis process: (1) before and (2) after acid functionalization to determine the MWNT weight, and (3) after the mMWNTs were produced to obtain the weight of Fe_3O_4 that was attached to the MWNTs. Similar verification of samples S4-S6 was not possible because the filtration, washing and drying step was eliminated. Transmission electron microscopy (TEM) and energy dispersive X-ray (EDX) spectroscopy was conducted with a JEOL 2010F field emission microscope, where the samples were suspended in ethanol, dripped on to a TEM grid and then wicked off with a tissue-wipe. A Fourier transformer infrared spectrometer (FTIR, Bruker Vertex 70, ATR Diamond accessory, 64 scans at a resolution of 4cm-1) was used to determine the absorption for the Fe-O bond in the MNPs. Magnetization measurements were performed using SQUID magnetometry at room temperature.

3.4 Results and Discussion

3.4.1 Synthesis of Magnetic MWNTs via Variable Acid-enabled Functionalization

We synthesize mMWNTs, i.e., MWNTS decorated with MNPs, using six variations in the method for acid treatment, as described in section 3.3.2 and illustrated in Figure 3.2. The variations are implemented to compare the influence of acid-treatment by HNO_3, H_2SO_4, or a 1:1 (v/v) mixture of the two by using (1) XPS to measure the oxygen content in the acid-treated MWNTs as a metric for functionalization, (2) XRD to determine the material composition and size of MNPs decorating the mMWNTs, (3) transmission electron microscopy (TEM) to visualize the mMWNTs, and (4) vibrating sample magnetometry (VSM) to measure magnetic properties. Further, we determine the feasibility of eliminating the filtration, washing and drying of MWNTs after acid treatment to prevent material loss to the filtrate and thus increase the yield of magnetized MWNTs (mMWNTs).

3.4.1.1 Material Phases

XPS analysis (Figure 3.3), shows that acid treatment always leads to an increase in oxygen content. While pure MWNTs contain ~2 atomic percentage (at.%) oxygen, treatment with either nitric or sulfuric acid increase oxygen content to 4-5 at.%. This increase is moderate when contrasted with the effect of a 1:1 (v/v) mixture of the two acids, which yields ~15 at.% oxygen.

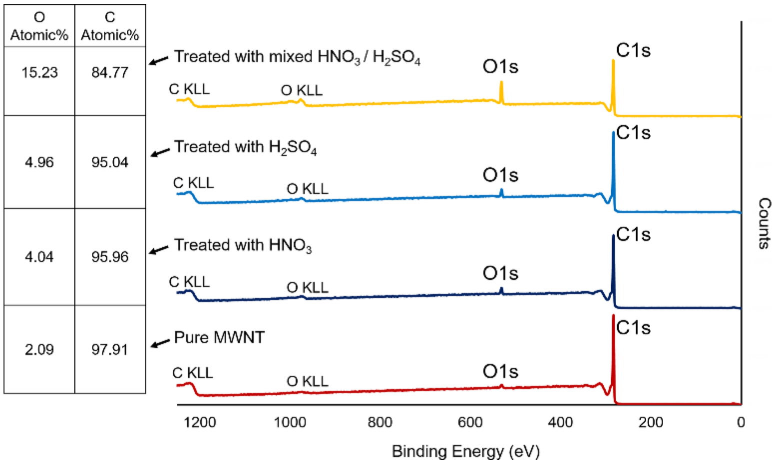

Figure 3.3: Comparison of acid-treatment routes. XPS analysis shows that treatment with HNO_3 or H_2SO_4 leads to a moderate increase in oxygen content (4-5%) relative to pure MWNTs (~2%). In contrast, treatment with a 1:1 mixture of the two acids produces a much higher (15.23%) oxygen content.

XRD analysis reveals the influence of a particular synthesis route on the material content of the mMWNTs. The spectra (Figure 3.4a) are used to quantify the resulting composition, presented in Table 3.1. For routes S1-S3, the XRD estimate is verified against the weights obtained using a weighing balance. That comparison, in Table 3.2, shows that the deviations from the XRD analyses are smaller than 5%. Table 3.3 lists the combined weight of the MWNT and its attached Fe_3O_4 MNPs as a fraction of the intended, or stoichiometric, weight.

Strong oxidizing acids cause structural damage to MWNTs and shorten their lengths. When these short MWNTs are washed and the dispersion filtered, they can be lost to the filtrate. A potential remedy to retain these shortened MWNTs is to eliminate the filtration step. To examine this, we contrast the compostion of samples S1-S3 and S4-S6 that are produced with and without the intermediate filtration respectively.

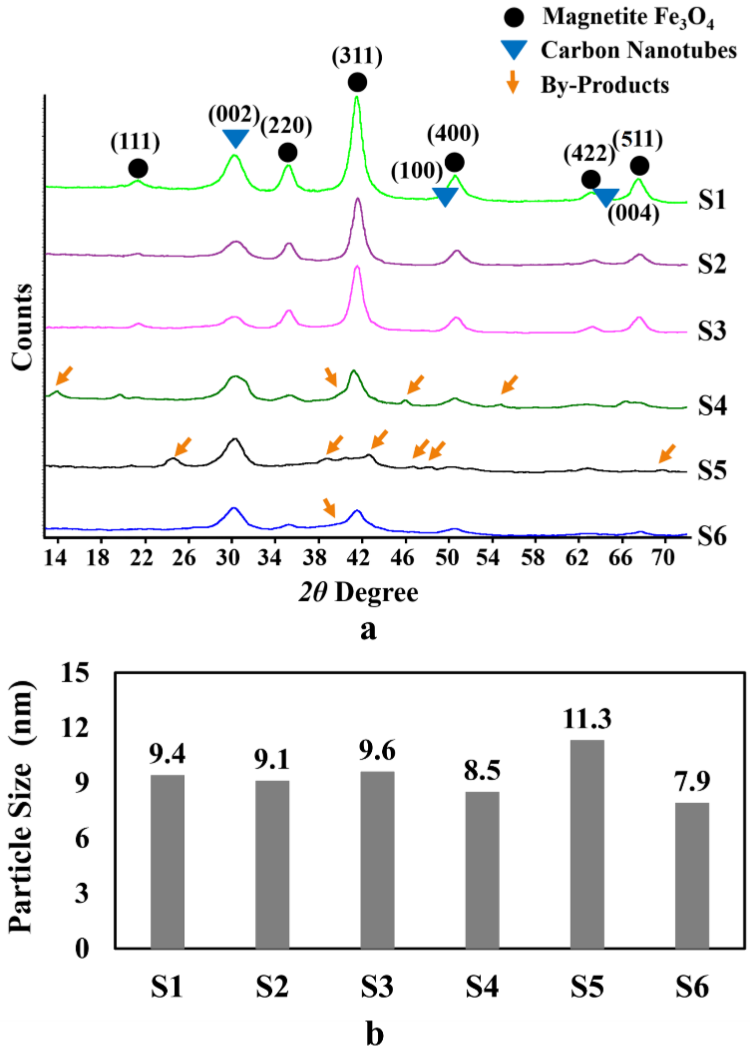

Figure 3.4: Comparison of Material Content of MWNTs. (a) The XRD (Co K_α, λ=1.79 Å) patterns for S1-S3 (b) The average crystallite size, determined using the XRD data by the Scherrer equation (3.3)) reveal a narrow particle size distribution of 8.5 -11.3 nm.

Samples S1-S3 contain only the intended material phases, i.e. magnetite (Fe_3O_4, PDF No. 01-071-6336) and hexagonal carbon C_6 (PDF No. 00-058-1638), as shown in Figure 3.4a. In contrast, undesired materials are found for samples S4-S6 that are an anciticpated consequence of co-precipitation in the presence of a strong acidic medium. S4 contains Akaganeite ($Fe^{3+}O(OH, Cl)$, PDF No. 00-013-0157). S5 contains the mildly magnetic iron oxide hematite (α-Fe_2O_3, PDF No. 00-032-0469), ferrous sulfate ($FeSO_4$, PDF No. 00-042-0229) and other phases that could not be identified by the EVA software using the PDF database. S6 contains $FeSO_4$. Thus, the filtration and drying of MWNTs subsequent to acidic functionalization is a necessary step.

Material Phase	S1	S2	S3	S4	S5*	S6
MWNT	41.7%	41.8 %	31.9 %	48.9%	38.8 %	47.3 %
Magnetite (Fe_3O_4)	58.3%	58.2 %	68.1 %	37.3 %	15.5 %	33.9 %
Hematite (α-Fe_2O_3)	0%	0%	0%	0%	28.4 %	0%
Akaganeite	0%	0%	0%	13.8 %	0%	0%
Ferrous Sulfate ($FeSO_4$)	0%	0%	0%	0%	17.3 %	18.8 %

Table 3.1: The XRD semi-quantitative analysis, obtained using TOPAS software, shows that the MWNT:Fe_3O_4 weight ratio differs from the intended value of 1:1 (w/w) that is stoichiometrically designed. (*A few peaks in the XRD spectrum for S5 result from material phases that could not be identified by TOPAS.)

Sample #	MWNT (wt %)		Fe_3O_4 wt%		Error
	XRD	Balance	XRD	Balance	
S1	41.7 %	43.97 %	58.3 %	56.03 %	2.27 %
S2	41.8 %	46.46 %	58.2 %	53.54 %	4.66 %
S3	31.9 %	35.06 %	68.1 %	64.94 %	3.16 %

Table 3.2: The weight percentages of MWNT and Fe_3O_4 for samples S1-S3, measured using a digital balance, deviates less than 5% from the corresponding measurements approximated through XRD analysis.

We note here that magnetite (Fe_3O_4) and maghemite (γ-Fe_2O_3) have almost identical crystal structures, and are thus nearly indistinguishable solely by XRD [131]. However, past reports have established that coprecipitation of Fe^{2+} and Fe^{3+} ions yields magnetite (Fe_3O_4) contaminated with maghemite (γ-Fe_2O_3) if the water used in the reaction contains dissolved oxygen, which oxidizes the Fe^{2+} to the Fe^{3+} state [187, 188]. If this is avoided, nearly pure magnetite (Fe_3O_4) nanoparticles are formed, which are stable in air and require high temperature (T = 300 °C) aeration for their oxidation into γ-Fe_2O_3 [195]. Thus, considering the water used in our reactions was meticulously degassed by boiling in vacuum for ~30 minutes and subsequent probe sonication for ~30 minutes, we assume that the nanoparticles produced herein by coprecipitation of Iron (II) and Iron (III) chlorides are largely of Fe_3O_4.

Material Phase	S1	S2	S3	S4	S5	S6
MWNT	90.2 %	91.6 %	54 %	100 %	78 %	82 %
Fe_3O_4	100 %	94 %	85.2 %	76.8 %	31 %	60 %
mMWNT (Total Yield)	95.3 %	92.8 %	69.6 %	88.4 %	54.5 %	71 %
Fe_3O_4: MWNT (w/w) (Magnetization Ratio, γ)	1.11	1.03	1.58	0.77	0.39	0.73

Table 3.3: Yields of the various material phases, as a fraction of their stoichiometrically designed values. The magnetization ratio γ is the ratio of Fe_3O_4: MWNT (w/w). The intended value of this ratio is unity for all samples.

Assuming a cubic lattice space ($a=b=c$), we calculated lattice parameters for samples S1-S3 at all XRD diffraction peaks (see Table 3.4) using Bragg's Law, i.e.,

$$a = \frac{\lambda}{2\sin\theta}\sqrt{h^2+k^2+l^2}\ . \tag{3.2}$$

These average lattice parameters were 8.410, 8.406 and 8.390 Å for S1, S2 and S3, respectively that are slightly higher than the anticipated values for magnetite (8.378 Å, PDF No. 01-071-6336; 8.394 Å, JCPDS No. 79-0417; and 8.400 Å, COD card No. 1011084) and further from those for γ-Fe_2O_3 maghemite (8.346 Å, PDF No. 01-089-5892; and 8.330

Å, COD card No. 9006316), which supports our assumption that magnetite is formed. The slight increase in the measured lattice parameters could be explained by the lattice defects and strains during the synthesis process.

Sample	**Lattice parameter (Å)**						
	(111)	(220)	(311)	(400)	(422)	(511)	$a_{average}$
S1	8.420	8.415	8.411	8.409	8.407	8.400	8.410
S2	8.413	8.410	8.407	8.400	8.405	8.398	8.406
S3	8.397	8.396	8.391	8.391	8.381	8.381	8.390

Table 3.4: The calculated lattice parameters at all XRD diffraction planes for samples S1, S2, and S3, obtained with Bragg's Law. The average lattice parameters for these samples concur with those for magnetite (Fe_3O_4).

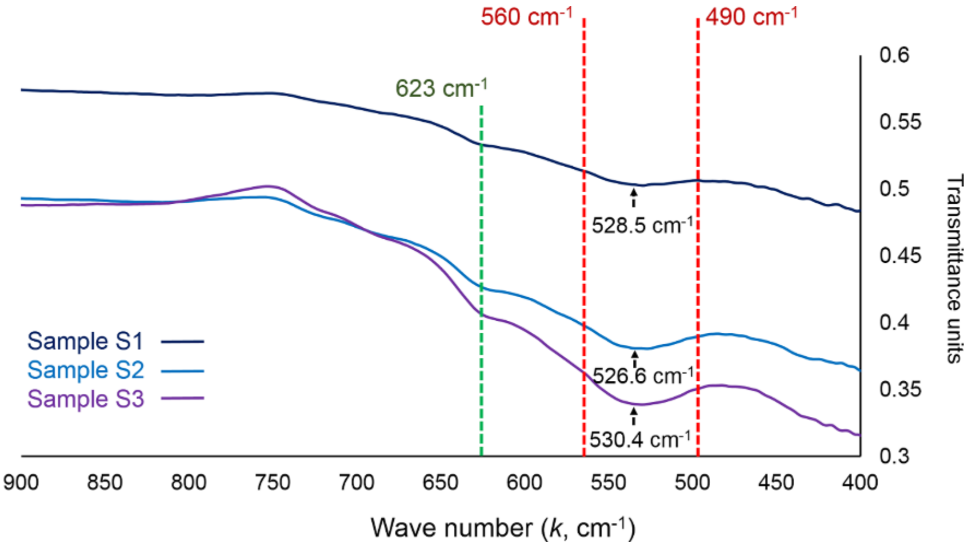

Figure 3.5: IR spectra of samples S1-S3 reveal individual broad absorption bands at 528.5, 526.6 and 530.4 cm^{-1}. The range between 490 and 560 cm^{-1} is associated with the vibration of the Fe–O functional group for samples S1, S2 and S3. This confirms magnetite formation since the absorption splits into multiple absorption bands for maghemite. The shoulder peak at 623 cm^{-1} could imply partial oxidation of magnetite into maghemite.

FTIR analysis at room temperature provided further information about the structure of samples S1-3. Figure 3.5 shows that, in the lower wavenumber range each sample has a single broad absorption band at 528.5, 526.6 and 530.4 cm^{-1}, respectively. The range between 490 and 560 cm^{-1} is associated with the vibration of the Fe–O functional group for samples S1, S2 and S3. This individual broad band confirms the formation of magnetite, since maghemite absorption occurs through multiple absorption bands [196]. However, the shoulder peak which occurs at 623 cm^{-1} could imply partial oxidation of the magnetite into maghemite [197].

Samples produced with the intermediate filtration step do not show substantial loss of MWNTs due to filtration when either HNO_3 or H_2SO_4 are used for functionalization. For S1 and S2, which use HNO_3 and H_2SO_4, the MWNT yields are 90.2% and 91.6% respectively. However, when a mixture of the two acids is used, a substantial fraction of the MWNTs is lost. S3 has a MWNT yield of a meagre 54%. This is because the acid mixture oxidizes and damages the MWNTs [81] much more than each acid individually. This influence is also evidenced by the substantially higher oxygen content of MWNTs treated with the acid mixture, as demonstrated by the XPS analysis above. Overall, the samples functionalized using either HNO_3 or H_2SO_4 (S1, S2) have considerably higher mMWNT yields (95.3% and 92.8% respectively) than those functionalized using the HNO_3/H_2SO_4 mixture (S3, 69.6%).

The magnetization ratio (γ), defined as the weight ratio of MNP to MWNT, is closest to the desired value of unity in samples S1 ($\gamma = 1.11$) and S2 ($\gamma = 1.03$). S3 yields the highest magnetization ratio ($\gamma = 1.58$), but this is because a substantial portion (46%)

of the MWNTs are lost due shortening by the acids while the produced MNPs are not. S4-S6 deliver the lowest magnetization ratios because iron is consumed in side reactions with the acid to produce non-magnetic byproducts. Considering a higher mMWNT yield, $\gamma \approx 1$ and minimal byproduct formation to be representative of a better quality process, magnetic decoration is best accomplished when the MWNTs are functionalized by either HNO_3 or H_2SO_4 and the intermediate filtration step is performed.

We use the Scherrer equation

$$D = 0.94\lambda / \left(B(2\theta)\cos\theta \right), \tag{3.3}$$

to determine the average Fe_3O_4 nano-crystal size D (Figure 3.4b). Here, B denotes the full width at half maximum (FWHM) of the profile of the highest peak at (311) expressed in radians, λ the X-ray wavelength and θ the Bragg angle. For all six samples, the MNP size lies in the narrow range from 8.5 – 11.3 nm. Thus, it appears that the co-precipitation process is not substantially influenced by variations in the synthesis route.

3.4.1.2 Decoration Quality and MWNT damage

TEM images at various magnifications (Figure 3.6) are used to visually evaluate the (1) quality of decoration and (2) the influence of the process on the structural integrity of the MWNTs.

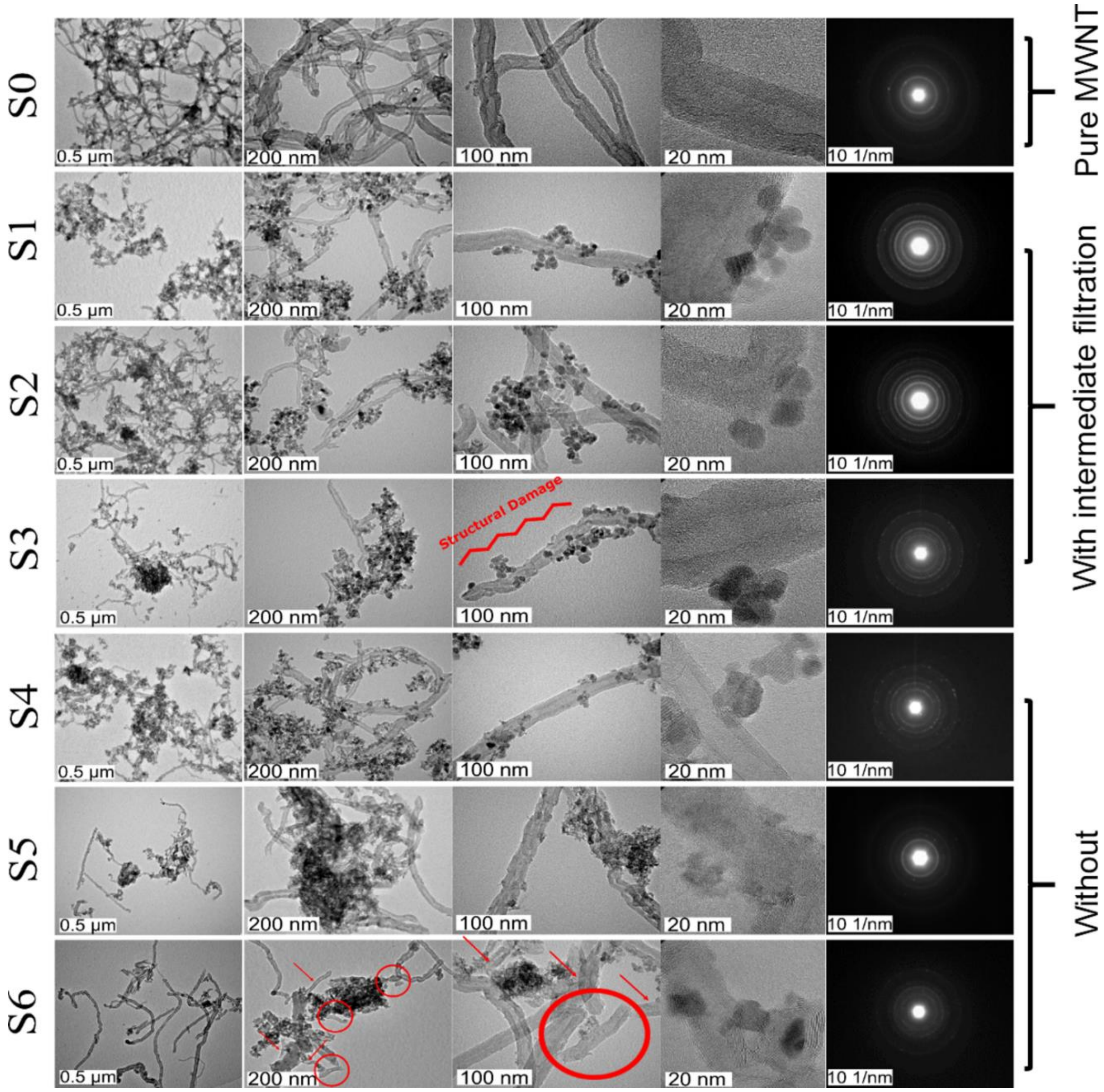

Figure 3.6: TEM images of samples S1-S6 show that the mMWNTs prepared with the intermediate filtration steps (S1-S3) have denser and uniform decoration, while those prepared without the step (S4-S6) have a sporadic non-uniform decoration. Decorations for S1-S4 and S6 are clearly crystalline, while that for S5 is largely amorphous, as demonstrated visually from the TEM image, and also by comparing the electron diffraction pattern of each with that of pure MWNTs (S0). Further, functionalization by either HNO_3 or H_2SO_4 does not inflict structural damage on the MWNT surface, which is evident by the smooth surfaces for S1, S2, S4 and S5. In contrast, S6, which was functionalized by a

mixture of the two acids, contains small (~ 100 nm) MWNT fragments, emphasized by the circles and arrows. S3, which was also treated with the acid mixture, does not contain these small fragments since these are lost during filtration. However the structural damage is manifested in the form of increased asperities on the MWNT surface.

The mMWNTs prepared using the intermediate filtration step (S1-S3) show a visibly higher decoration density and fairly uniform decoration. S3 shows the highest decoration density, which is consistent with the highest value of $\gamma = 1.58$ obtained using XRD analysis. In contrast, mMWNTs prepared without the intermediate filtration step (S4-S6) show sporadic decoration. S5 has the lowest decoration density, which agrees with the obtained value of $\gamma = 0.39$. Further, while S1-S4 and S6 have visibly crystalline decorations, the decorations on S5 are largely amorphous. This is evidenced by comparing the electron diffraction patterns of all samples (S1-S6) with pure MWNTs (S0). The diffraction pattern of S5 is largely identical to S0, i.e., no crystalline phases other than MWNTs are present in S5. In contrast, the diffraction patterns of all other samples (S1-S4, S6) differ from that of pure MWNTs, i.e., they contain crystalline phases other than MWNTs.

When MWNTs are functionalized using either HNO_3 or H_2SO_4 (S1, S2, S4, S5) they experience slight damage. In contrast, functionalization with a mixture of the two acids (S3, S6) leads to greater structural damage. Short (≈100 nm) MWNT fragments are seen in S6. Similar fragments were also likely produced in S3, but were lost to the filtrate. Here, the MWNT surface shows asperities that are indicative of structural damage.

3.4.1.3 Magnetic Properties

Fe_3O_4 nanoparticles in the size range formed herein have a saturation magnetization M_s = 60-80 emu/g [198, 199], while pure MWNTs (sample S0) are diamagnetic [57, 58]. Thus, the mMWNTs are expected to exhibit intermediate M_s values, which is observed through VSM magnetometry (Figure 3.7b).

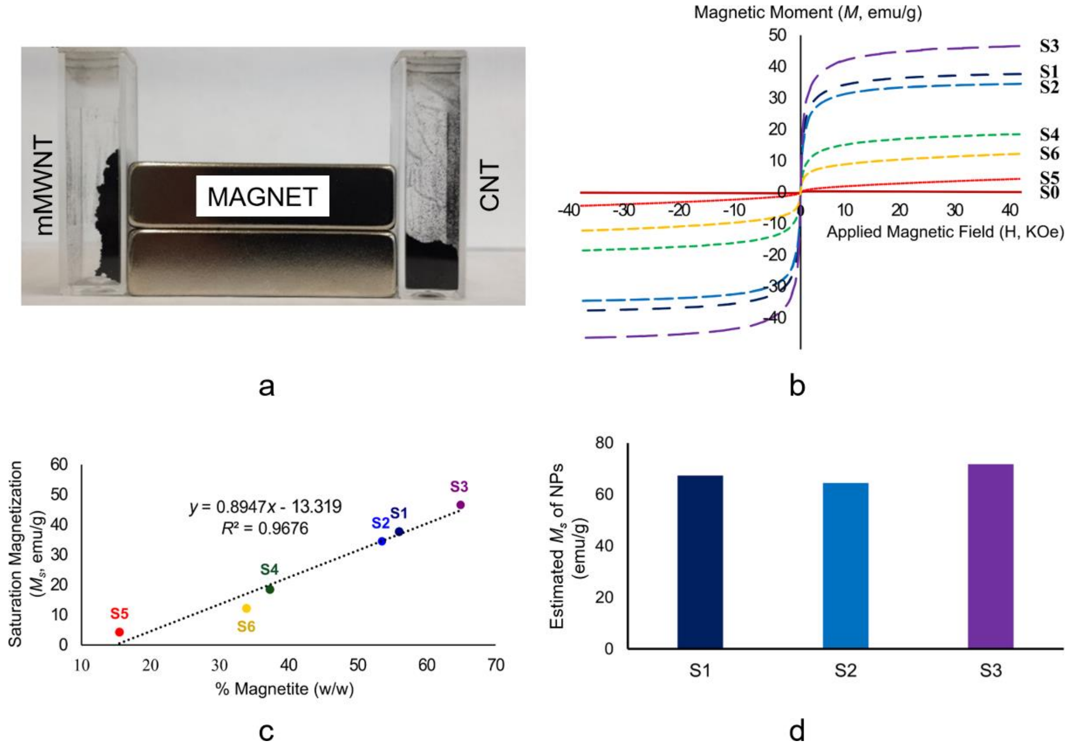

Figure 3.7: Magnetic Characterization. (a) The magnetized MWNTs (mMWNTs, left) are attracted by a magnet, while the bare MWNTs (right) show no such response. (b) Magnetic hysteresis curves. (c) The linear variation of M_s with the fraction of MNPs (w/w) produced by the respective synthesis routes explains the difference in M_s values produced by the various synthesis routes. (d) The M_s values of the NPs were estimated by dividing the M_s of the mMWNT samples S1-S3 by the mass fraction of the nanoparticles.

While the nanocrystals are expected to be individually superparamagnetic due to their small sizes [92], interactions between MNPs could lead to superferromagnetism, particularly in anisotropic ensembles [199-201]. However, the measurements provide no evidence of this phenomenon. The hysteresis data of Figure 3.7b shows that all samples are superparamagnetic at room temperature, i.e., there is no observable remanence and the coercive field is zero.

The variation in M_s depends upon the relative content of Fe_3O_4 in a sample, as shown in Figure 3.7c. Thus, the mMWNTs produced by a process that includes intermediate filtration to remove acids (S1-S3) are associated with higher M_s than those prepared without this step. Sample S5 has the weakest M_s = 4.3 emu/g, which is to be expected from the poor decoration observed in the corresponding TEM images, as well as from the lower ~15% (w/w) Fe_3O_4 content revealed through the XRD analysis.

The M_s of the MNPs can be estimated by dividing the M_s of the mMWNTs from samples S1-S3 by the mass fraction of MNPs in the corresponding samples. As shown in Figure 3.7d, we estimate that the M_s of the nanoparticles formed lie in the range of 66-71 emu/g, which is consistent with Fe_3O_4 nanoparticles in the size range formed herein [198, 199], and substantially higher than what would have resulted if the Fe_3O_4 were oxidized to γ-Fe_2O_3, i.e., M_s ~ 40 emu/g [195, 198, 199, 202, 203]. This adds credence to our claim that the nanoparticles formed are indeed magnetite.

3.4.2 Influence of MNP Concentration on the Decoration of mMWNT

Figure 3.8 presents TEM images at various magnifications that help visualize the mMWNTs and their decoration as the magnetite weight percentage with respect to MWNT weights is varied. For all samples, the high-resolution images show that magnetite MNPs are attached to the outer surfaces of MWNTs. The MNPs are crystalline with crystallite sizes between 10-15 nm.

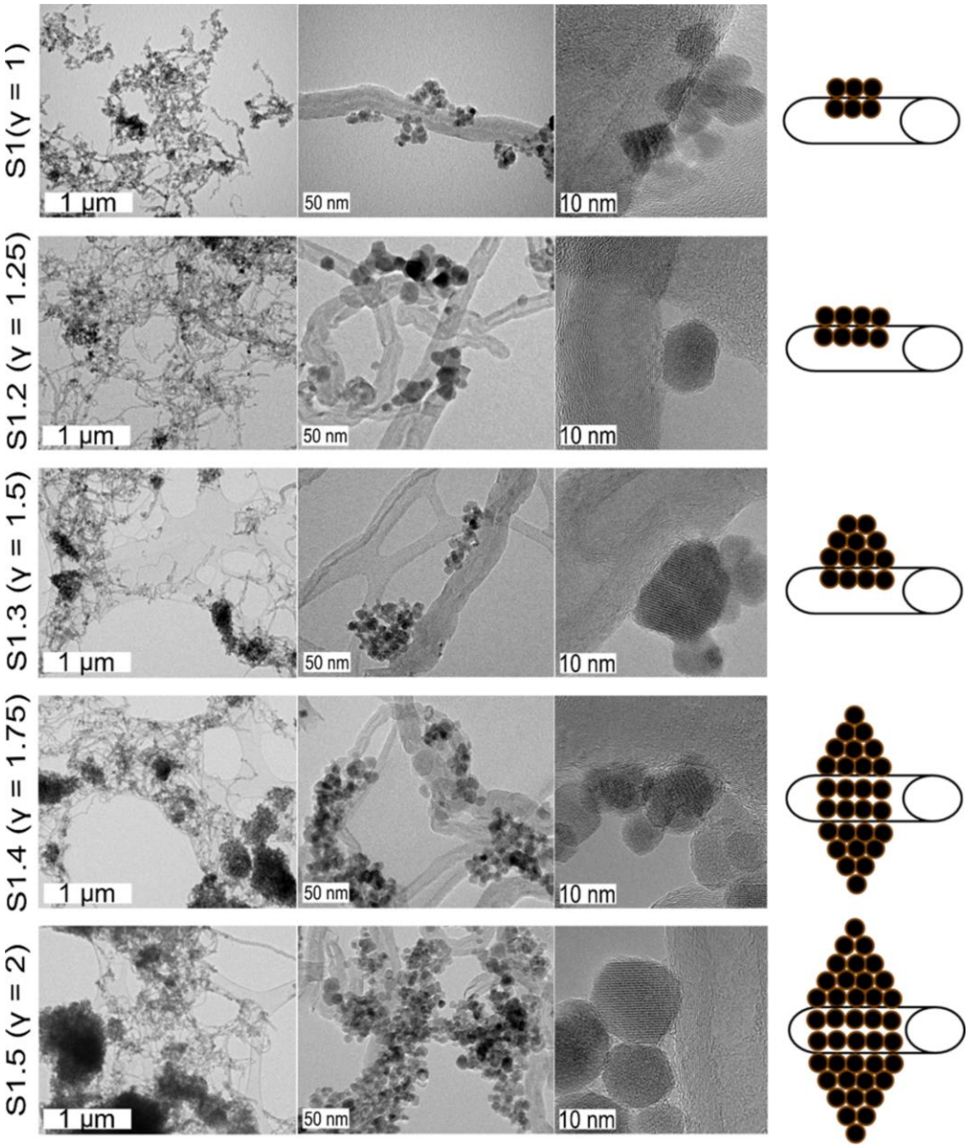

Figure 3.8: Influence of Fe_3O_4 - MWNT weight ratio (γ) on Morphology. Magnetic nanoparticles are precipitated on activation sites. However, when γ is increased above a certain value for which all available sites are occupied by MNPs, further precipitation of the nanoparticles produces MNP agglomeration in a direction perpendicular to the MWNT axis. An idealization of this process is presented on the left.

Increasing γ from 1 to 2 has a noticeable effect on the decoration density as the numbers of magnetite MNPs that have accumulated at various sites increases. The activated MWNT weight is constant in all samples. Thus, increasing the Fe^{+2}/Fe^{+3} weight content attaches a larger amount of MNPs to the same number of activation sites. Samples S1 and S1.2 reveal better decoration uniformity and distribution, implying that the numbers of activated sites on the outer surfaces of MWNTs and the corresponding MNPs are roughly equal. For S1.3–S1.5, the sizes of the MNP agglomerates increase as the magnetite weight percentage is raised. Since the weight percentage of magnetite is greater for S1.5 than for S1.4, and likewise for S1.4 it is greater than for S1.3, this supports our interpretation that a larger amount of MNPs become attached to a near constant number of activation sites. After all activated sites are occupied, due to their relatively high surface energy, excess Fe^{+2}/Fe^{+3} ions nucleate new MNPs on the surfaces of those that were previously precipitated.

Figure 3.8 presents representative TEM images for all samples, which reveal how the decoration is influenced by increasing the MNP weight percentage. During covalent functionalization, decoration is restricted to activated sites until all these sites are completely occupied. Thereafter, the surface energy of freshly produced MNPs facilitates their accumulation on the free surfaces of MNPs that are already attached to the MWNTs [204]. Consequently, this subsequent accumulation proceeds primarily in a direction perpendicular to the MWNT surface. Therefore, sample S1 with $\gamma = 1$ contains an optimal mMWNT sample for which all activated MWNT sites are mostly decorated with single MNPs and there are relatively few large agglomerates.

3.4.3 Effects of Changing MNPs Chemical Composition on the mMWNTs

3.4.3.1 Material Phases

The XRD analysis presented in Figure 3.9a for S1, S1m and S1c shows that the samples consist only of the intended material phases, being devoid of unanticipated foreign phases. All three samples reveal the existence of the crystalline spinel phase and hexagonal carbon C_6 (PDF No. 00-058-1638). Use of the powder diffraction file (PDF) database for the Eva software qualitatively confirms that the spinel phase is magnetite (Fe_3O_4, PDF No. 01-071-6336) for S1 and copper zinc ferrite ($Cu_{0.4}Zn_{0.6}Fe_2O_4$, PDF No. 01-077-0013) for S1c. Since $Mn_{0.2}Cu_{0.2}Zn_{0.6}Fe_2O_4$ could not be identified with the PDF database, XRD could not confirm its existence in S1m.

For this reason, we also employed EDX/TEM, as shown in Figure 3.9b, to determine the spinel structure. The result confirms the existence of elemental Mn, Cu, Zn, Fe, and O. This supports our inference that $Mn_{0.2}Cu_{0.2}Zn_{0.6}Fe_2O_4$ is produced. Previous investigations have established that oxygen dissolved in water can partially oxidize the coprecipitated magnetite (Fe_3O_4) into maghemite (γ-Fe_2O_3), both of which have nearly identical crystal structures [187, 188]. Degassing of water by boiling it in vacuum for ~30 minutes and subsequent probe sonication for ~30 minutes removes the dissolved oxygen from the reaction media, and its use produces reasonably pure magnetite (Fe_3O_4) nanoparticles [195]. Thus, we assume that the nanoparticles that were produced by coprecipitation of the iron (II) and iron (III) chlorides consisted of Fe_3O_4.

We used the Scherrer equation (3.3) to determine the average magnetic nanocrystal size *D*. For all three samples, the MNP sizes lie in the narrow range of 8.1, 8.9 and 9 nm for S1, S1m and S1c, respectively.

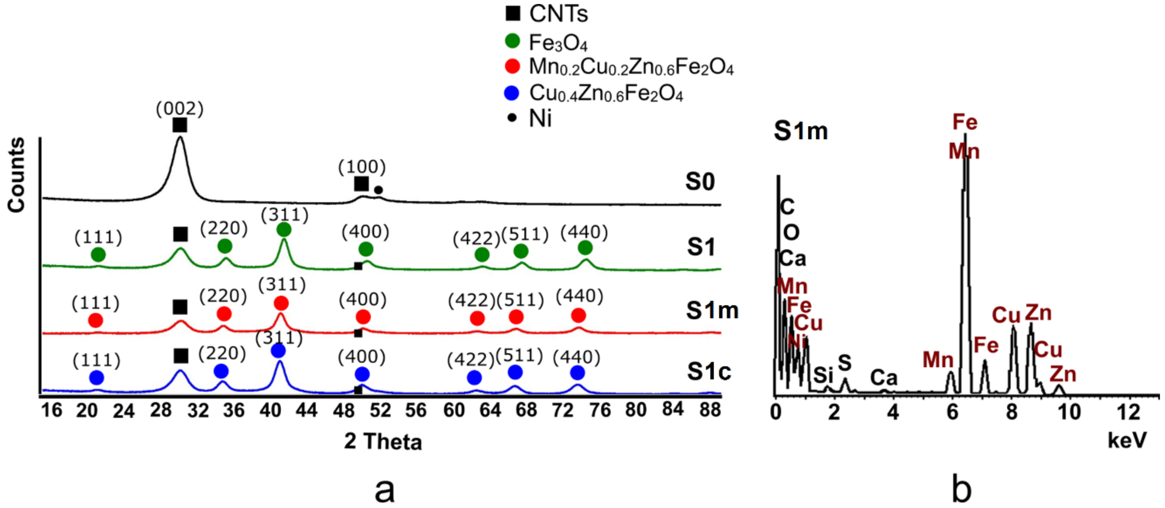

Figure 3.9: Phases Analysis of Magnetized MWNTs. (a) The XRD (Co K_α) patterns show that, besides C_6, a nanocrystalline spinel phase was formed. The Spinel phase in S1 was identified as magnetite (Fe_3O_4), in S1c it was Cu-Zn ferrite ($Cu_{0.4}Zn_{0.6}Fe_2O_4$). The corresponding phase in S1m could not be identified using the powder diffraction file (PDF) database. (b) EDX analysis revealed the presence of Mn, Cu, Zn, Fe, and O, which supports our inference that S1m contains $Mn_{0.2}Cu_{0.2}Zn_{0.6}Fe_2O_4$.

3.4.3.2 Decoration with Different MNPs

TEM images show successful direct attachment of the MNPs to the MWNT surfaces for samples S1, S1m and S1c at various magnifications (Figure 3.10). All MNPs have high crystallinity with a narrow crystallite sizes distribution between 10-15 nm. The $Cu_{0.4}Zn_{0.6}Fe_2O_4$/CNT sample S1c reveals more MNP agglomeration than is evident for S1 and S1m.

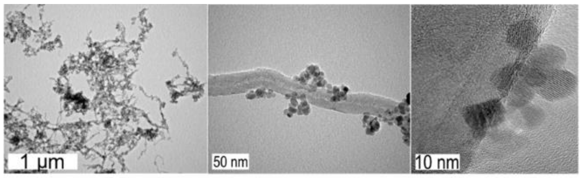

S1 (Fe_3O_4-CNT)

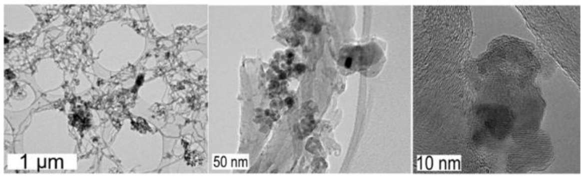

S1m ($Mn_{0.2}Cu_{0.2}Zn_{0.6}Fe_2O_4$-CNT)

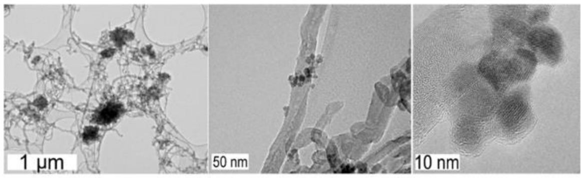

S1c ($Cu_{0.4}Zn_{0.6}Fe_2O_4$-CNT)

Figure 3.10: TEM images of samples S1, S1m and S1c (from top to bottom) confirm that all samples were successfully decorated with highly crystalline (but different) MNPs that were synthesized within the narrow size distribution of 10-15 nm.

3.4.3.3 Tunable Magnetic Properties

While the MNPs are expected to be individually superparamagnetic due to their small sizes [92, 202], the hysteresis data of Figure 3.11a shows that, since there is no observable remanence or coercive field, all of the mMWNT samples are also superparamagnetic at room temperature. The magnetic saturation M_s of the whole specimen is 30.7, 10.5 and 16.6 emu.g^{-1} for whole mMWNT specimens ($\gamma = 1$) for samples S1, S1m and S1c, respectively. These values correlate well with the MNP compositions and, considering γ variations, M_s for the Fe_3O_4–MWNT sample (30.7 emu.g^{-1}) lies within the range (15-50 emu.g^{-1}) reported in the literature [106, 123, 126, 128, 186, 205]. Since samples S1m and S1c are new and hitherto unexamined, similar results are not available in the literature. However the measured M_s values for these samples are comparable with those for their closest MNP families, i.e. 20 emu.g^{-1} for $Mn_{0.2}Zn_{0.8}Fe_2O_4$–MWNT [136] and 17 emu.g^{-1} for $CuFe_2O_4$–MWNT [137].

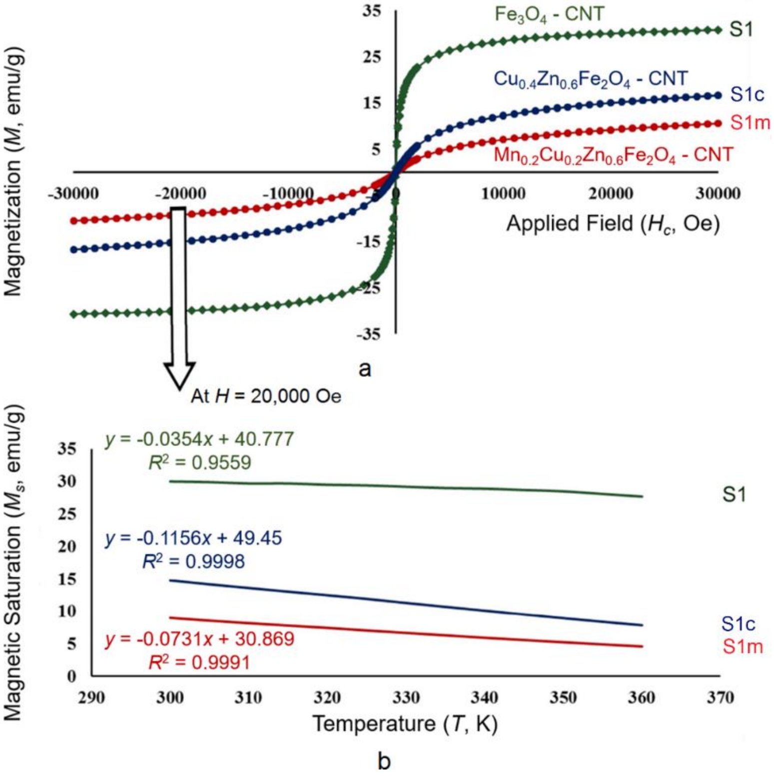

Figure 3.11: Magnetic Characterization. (a) Magnetic hysteresis curves of the dry powders shows no evidence of remanence, i.e., the mMWNTs are superparamagnetic. (b) For all samples, M_s decreases with increasing temperature. Magnetite (S1) has the strongest magnetization and weakest sensitivity to temperature, Mn-Cu-Zn ferrite (S1m) has the weakest magnetization while Cu-Zn Ferrite (S1c) has the strongest temperature sensitivity.

The magnetic properties for the three samples have different sensitivities to a temperature increase from 300 to 360 K, as shown in Figure 3.11b. For all three samples, M_s decreases linearly with increasing temperature but with different slopes. Since S1 contains high Curie temperature Fe_3O_4 MNPs, it is weakly sensitive to the temperature rise and hence exhibits the lowest slope of 0.04 emu.g^{-1}.K^{-1} due to a small loss of 7.7% from its 300 K M_s value. Results for the MNPs that have lower Curie temperatures, i.e., $Mn_{0.2}Cu_{0.2}Zn_{0.6}Fe_2O_4$ in S1m and $Cu_{0.4}Zn_{0.6}Fe_2O_4$ in S1c, show that they are more sensitive to the temperature increase. The two respective slopes of 0.07 and 0.12 emu.g^{-1}.K^{-1} are steeper, with samples S1m and S1c losing 48.9% and 46.6% of their M_s values at 300 K. These results provide evidence that the magnetic properties of mMWNTs can be tuned to by varying the MNP composition.

3.5 Conclusion

Six functionalization routes to decorate MWNTs by *in situ* co-precipitated magnetic nanoparticles are examined to determine best practices. Of these six routes, four (S2 and S4-S6) are newly reported herein. Functionalization using H_2SO_4 is found to minimize MWNT loss during decoration and provides a decoration density very close to unity. Although mixtures of HNO_3 and H_2SO_4 have been commonly employed, they are found to inflict significant structural damage to the MWNTs. If the MWNT suspension is filtered after acid functionalization, this damage produces short MWNT fragments that are lost to the filtrate. The loss of MWNTs can be as much as ≈ 46% (w/w) and accompanied with significant nanotube oxidation with oxygen content up to 15.23%. Functionalization with either HNO_3 or H_2SO_4 is much less destructive with less oxidation in this context. However, even after considering MWNT damage, the filtration step is important since it removes leftover acid from the dispersion prior to co-precipitation. In the absence of filtration, the acids react with iron ions to produce nonmagnetic byproducts which compromise the magnetization of the mMWNTs. Overall, (a) functionalizing with HNO_3 or H_2SO_4, followed by (b) filtration, (c) washing, (d) drying and (e) subsequent *in situ* coprecipitation of MNPs yields the best quality MNPs, relatively high mMWNT yield of ≈ 95%, magnetization ratio close to the intended value of unity, reasonably uniform MNP distribution on the mMWNT surfaces, and negligible MWNT shortening and damage.

MWNTs were decorated by *in situ* co-precipitation with different magnetic nanoparticles (MNPs) for varying magnetization weight ratios γ in the range of 1-2. The decoration of the MWNTs with MNPs depends upon the availability of activation sites on the outer surfaces of the nanotubes. All MWNT activation sites are utilized when γ reaches a specific value. Typically, γ =1 provides uniform decoration and minimum agglomeration. Although the quantity of MNPs exceeds the number of the activation sites when γ is increased above this value, decoration still continues with nanoparticle agglomeration occurring perpendicular to the MWNT surface. The MNP chemical composition influences the magnetic properties of mMWNTs. Fe_3O_4 MNPs that have a high Curie temperature produce mMWNTs with the highest magnetic saturation M_s = 30.7 emu.g^{-1}. These mMWNTs exhibit the weakest sensitivity to a temperature increase of 60 K above 300 K with a corresponding reduction in M_s of 7.7%. $Mn_{0.2}Cu_{0.2}Zn_{0.6}Fe_2O_4$, and $Cu_{0.4}Zn_{0.6}Fe_2O_4$ MNPs have lower Curie temperatures. Thus mMWNTs produced with these MNPs have lower M_s values (10.5 and 16.6 emu.g^{-1}, respectively) and are more sensitive to a temperature increase (with up to 48.9% and 46.6% reductions in M_s).

4. Conductive Nano-inks Based on Covalently Magnetized MWNTs

4.1 Introduction

In this chapter, an experimental investigations will be presented to highlight the application of magnetic MWNT synthesised via covalent functionalization in the fabrication of conductive nano-inks. We synthesize a novel and hitherto unreported class of colloidal suspensions for which the dispersed phase, which consists of multiwall carbon nanotubes (MWNTs) decorated with magnetic nanoparticles (MNPs), is both magnetoresponsive and electrically conductive. Synthesis of the dispersed phase merges processes for producing ferrofluids and magnetic MWNTs (mMWNTs). Further, we explore how to adapt this magnetoresponsive and conductive ink to be also bio-sensitive enabling the printing of biosensing strips by the magnetic dynamic-assembly. That led to the fabricating of biological sensors. This chapter is adapted from the Journal of Magnetism and Magnetic Materials, Magnetoresponsive conductive colloidal suspensions with magnetized carbon nanotubes, 421, **Ahmed M Abdalla**, Abdel Rahman Abdel Fattah, Suvojit Ghosh, and Ishwar K Puri, Copyright 2017, with permissions from Elsevier. The author of this thesis is the first author and main contributor of the above mentioned publication and has conducted all the experiments. Rest of the work and results have been previously published in journal of ACS Applied Materials and Interfaces, Magnetic Printing of a Biosensor: Inexpensive Rapid Sensing to Detect Picomolar Amounts of Antigen with Antibody-Functionalized Carbon Nanotubes, 9 (13), Abdel Rahman Abdel Fattah, **Ahmed M**

Abdalla, Sarah Mishriki, Elvira Meleca, Fei Geng, Suvojit Ghosh, and Ishwar K. Puri, Copyright 2017, with permissions from ACS Publications. The author of this thesis is the co-first author with Dr. A. R. Abdel Fattah, Ms. S. Mishriki of the above mentioned publication and has performed the magnetization of carbon nanotubes toward the biological ink's preparation and done the materials characterization.

4.2 Background Information

Nanofluids are colloidal suspensions that contain nanoparticles dispersed in a liquid [151]. Due to their superior electric conductivity, carbon nanotubes (CNTs) have been introduced as the dispersed phase in a nanofluid. When dispersed in an aqueous medium, as little as 0.5% (w/w) of CNTs can increase its electric conductivity by an order of magnitude [154]. However, CNTs tend to flocculate rapidly in an aqueous medium, yielding clusters of randomly oriented nanotubes that settle under gravity [158]. Since flocculation is typically caused by inter-CNT attractions due to surface charges [160, 161], temporary dispersions can be achieved by enhancing inter-CNT distances, e.g., through ultrasonication [206, 207]. However, to achieve long term stability, chemical peptization methods are required, such as providing CNTs with a surface coating to counterbalance the surface interactions [164]. Peptization is hard to achieve for CNTs due to their high molecular weight, hydrophobicity and inertness of their outer surfaces [208].

Ferrofluids are nanofluids that respond to a magnetic field [209-212] since the dispersed phase consists of magnetic nanoparticles (MNPs) [213-215]. Several methods have been developed to peptize MNPs in aqueous media to enable their colloidal stability for extended periods [216-218]. Typically, MNPs are coated with a surfactant that produces interparticle repulsion [161, 219]. These MNPs can chaperone other nonmagnetic materials, such as MWNTs, to orient and organize them [20, 220], and print spatial heterogeneities in materials [95, 96]. However, the MNPs in most ferrofluids are ferrites that possess poor intrinsic electrical conductivity. A ferrofluid containing an electrically conductive dispersed phase has promising applications. Since its MNPs can be manipulated by a magnetic field, the local electrical conductivity of a conductive ferrofluid can be tuned. Magnetic manipulation also allows the printing of an electronic circuit with a conductive ink.

Conductive nanofluid inks are typically dispersions of gold, silver, and copper nanoparticles, but these are expensive, require nanoparticle sintering and have only fair dispersion and oxidation resistance [221]. While use of graphene and CNTs has been reported, their agglomeration and dispersion are problematic [151, 155, 222]. Our solution is to decorate multiwall carbon nanotubes (MWNTs, the electrically conductive dispersed phase) with magnetically responsive MNPs.

We probe ways to influence the electrical and magnetic properties of the MWNTs by altering the material content of the MNPs. The synthesized mMWNTs are dispersed in an aqueous medium to prepare novel magnetoresponsive conductive colloidal suspensions (MCCs). An ionic dispersant (tetramethylammonium hydroxide, or TMAH), commonly used to peptize ferrite MNPs, is used to ensure colloidal stability. These MCCs are a hitherto unreported type of colloidal suspension that responds to an external magnetic field, is electrically conductive and can be stably dispersed.

The need for early pathogen detection and diagnosis of disease has led to strategies for DNA and antigen (Ag) detection such as polymerase chain reaction (PCR) and enzyme-linked immunosorbent assay (ELISA). Being time consuming and labor intensive, these methods are not suitable for inexpensive rapid detection [223]. Recent advances in nanomaterial synthesis and nanofabrication have enabled the rapid identification of pathogen and disease biomarkers. Nanoscale lithography allows for femtosensitive DNA detection [224, 225] and the electrical response of carbon nanotubes (CNTs) to specific biological species has led to resistance and field effect transistor (FET) biosensors [226-230].

Biosensors can be tailored towards specific biomarkers by selectively modifying a CNT surface, e.g., by decorating it with particular antibodies (Abs), which enables the detection of specific Ags, leading to an inexpensive and rapid alternative to current methods. Usually, fabrication utilizes laborious lithography for electrode deposition and general sensor assembly, while simpler benchtop fabrication methods, e.g., CNTs in paper-based biosensors, provide longer sensing response times [231].

Magnetic nanoparticles (MNPs) can be patterned into a polymer matrix to produce a functional material [62, 215, 232-241]. As described previously in MCC, MNPs can also be used to chaperon MWNTs by remotely manipulating MNP-MWNT complexes with a magnetic field, for instance, to print conductive networks and sensors [232, 242]. Magnetic MWNTs (mMWNTs or MWNT-Fe_3O_4 hybrid nanoparticles) have been explored for biological applications, e.g., human IgG immunosensors [233], and for electrical current measurements [230, 243]. Most such measurements involve cyclic voltammogram analysis, which requires sophisticated acquisition devices and a magnet to be continually present during sensing to affix the sensing material to an electrode [244].

Based on the same concept of the previously described MCC, our contribution is through development of a new mMWNT biosensor ink that utilizes immobilized Abs to detect specific Ags, which expands the utility of mMWNTs as protein-sensing nanomaterials. Without requiring complex chemistry or lithographic techniques, synthesis of the magnetic ink is inexpensive and a sensor strip is readily fabricated. The ink is printed using an external magnet by dynamically organizing its nanoparticle constituent into an electrically conducting strip in 4-5 minutes, excluding drying time. The resulting biosensor detects Ag samples with picomolar sensitivity in less than a minute.

Biomarkers distinguish between healthy and diseased cells. Examples include prostate-specific antigen (PSA) [245], insulin-like growth factors (IGFs) [246], and human epidermal growth factor receptor (HER)-2 [247], which are used to diagnose human cancers. Recognized by the anti-c-Myc primary Ab, the c-Myc Ag is over-expressed in many human cancers, such as breast, prostate, gastrointestinal, lymphoma, melanoma and myeloid leukemia [248, 249]. High expression of c-Myc Ag can accelerate tumour progression [250], making it a potentially important cancer biomarker for predicting clinical outcomes. Therefore, we focus on c-Myc Ag detection to illustrate proof of concept of an Ab magnetic ink for an Ag sensing application.

4.3 Methodology

4.3.1 Materials and Reagents

Multiwall carbon nanotubes (MWNTs) produced by CVD with purity > 95%, outside diameter of 20-30 nm, inside diameter of 5-10 nm and length between 0.5-2.0 µm, were purchased from US Research Nanomaterials. Other reagents used were ferric chloride hexahydrate ($FeCl_3 \cdot 6H_2O$, 97%, Alfa Aesar), ferrous chloride hexahydrate ($FeCl_2 \cdot 4H_2O$, 98%, Alfa Aesar), copper II chloride ($CuCl_2$, 98%, Alfa Aesar), tetramethyl ammonium hydroxide ($C_4H_{13}NO \cdot 5H_2O$, 98%, Alfa Aesar), manganese II chloride tetrahydrate ($MnCl_2 \cdot 4H_2O$, 99%, Sigma Aldrich), zinc chloride ($ZnCl_2$, 99%, Sigma Aldrich), sodium hydroxide (NaOH, 97%, Caledon Laboratory Chemicals), nitric acid (HNO_3, 68-70%, Caledon), and ammonium hydroxide (NH_4OH, 28-30%, Caledon). C-Myc Ag (Abcam, Cambridge, Massachusetts, USA) had a molecular weight of 49 kDa (49,000 g mol^{-1}). Bovine serum albumin (BSA) (Sigma Aldrich, Oakville, Ontario, Canada) was used as a negative control. All reagents were used as received without further purification. The NdFeB, Grade N52 magnets were purchased from K&J Magnetics Inc (25.4×6×6 mm). The electrode support was fabricated using polydimethylsiloxane (PDMS) and a curing agent (Sylgard 184 kit, Dow Corning). The coverslips (Fisher Scientific, 12-540-B) had dimensions of 22×22×2 mm.

4.3.2 Synthesis of Magnetoresponsive Conductive Colloids (MCCs)

Three different MCCs (MCC1, MCC2 and MCC3) were synthesized using the mMWNT samples S1, S1c, and S1m (section 3.3.4). These preparations followed principles used to synthesize ordinary ionic ferrofluids [162]. As illustrated in Figure 4.1, since the MNPs are attached to the outer surface of the MWNTs through covalent bonds, they magnetize the MWNTs and, with assistance of an ionic surfactant and vigorous sonication, carry, suspend, and stabilize the MWNTs in DI water. The mMWNTs therefore have the ability to move along with the whole fluid in response to an applied magnetic field. The ionic surfactant facilitates whole fluid electric conductivity since the electrical discontinuity due to separate suspended mMWNTs is now overcome.

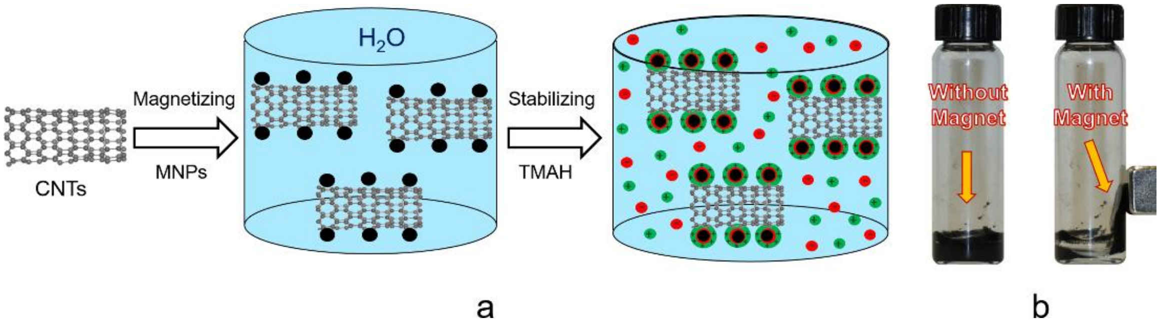

Figure 4.1: Synthesis of Magnetoresponsive Conductive Colloids (MCCs). (a) MWNTs are first dispersed in water and then covalently functionalized with MNPs that are coprecipitated *in situ*. The resulting mMWNTs are peptized using tetramethylammonium hydroxide (TMAH) as a surfactant, yielding magnetoresponsive conductive colloids (MCCs). (b) Upon visual inspection, an aqueous dispersion of MCCs rests in the absence of a magnet (left) whereas it is attracted towards a magnet when it is present (right).

Although the mMWNT suspensions were not filtered or dried, the co-precipitation by-products were removed from the three samples by decanting and washing them. The pH was concurrently stabilized between 9-10 using precipitant drops during washing. The resulting dilute suspensions settled over 24 h under gravity after which excess water was removed, leaving behind denser suspensions. Next, a 25% TMAH solution of the ionic surfactant was added where 60 ml of the solution was used for each 100 ml of an mMWNT suspension. Sonication was performed thereafter for 10 min using a probe sonicator. The MCCs were isolated for 24 h after which excess water was again removed. Samples of known volume were extracted from the preparation before and after surfactant addition, and also weighed before and after drying.

4.3.3 Synthesis of Magnetic Biological Ink

Like MCC, the first step in producing the magnetic biological ink requires treatment of CNTs with concentrated HNO_3. This creates surface sites where reactive molecules, such as COOH, C=O, and C–OH, form covalent bonds with the CNT scaffold and subsequently nucleate magnetite nanocrystals (Fe_3O_4) [18]. When the MNP yield is low enough, anti-c-Myc covalently bonds to the surface through a condensation reaction between the amine groups of the Ab and the remaining carboxylic groups [226] without additional reagents [244]. The synthesis process of bioink is described in Figure 4.2.

The MWNTs are functionalized in the manner we reported of sample S1 described previously in section 3.3.3 [18]. Briefly, 1 g of MWNTs was first activated by dispersing it in 200 mL of concentrated nitric acid and sonicated for 4 h in a sonication bath (VWR International, Model: 97043-936). The activated MWNTs (aMWNTs) were subsequently washed several times with deionized (DI) water, filtered, washed again and finally dried in a vacuum oven. Magnetite nanoparticles were co-precipitated onto the aMWNTs by stoichiometric calculations to obtain a Fe_3O_4:aMWNTs magnetization weight ratios $\gamma = 0.1$, 0.2, and 0.4 (w/w). For $\gamma = 0.4$, a mixture of 0.92 g of $FeCl_3 \cdot 6H_2O$ and 0.36 g of $FeCl_2 \cdot 4H_2O$

was first dissolved in 160 mL of degassed DI water and followed by ultrasonic dispersion of 1 g of the aMWNTs for 10 mins with a probe sonicator (Qsonica, Model: Q500 with 1/4″ micro-tip at 35% power) and subsequently for 50 minutes in a sonication bath at 50° C. A 2 ml of 30% ammonia solution was slowly introduced as a precipitant to increase the pH to 9. The magnetized MWNTs (mMWNT) produced were washed several times until a pH ~ 7 was reached, and then filtered and dried in a vacuum oven for 1 hr. In the case of the adsorbed MNPs on the surface of MWNTs, a previous methodology [232] was followed to entangle magnetite and MWNTs, yielding $\gamma = 0.4$.

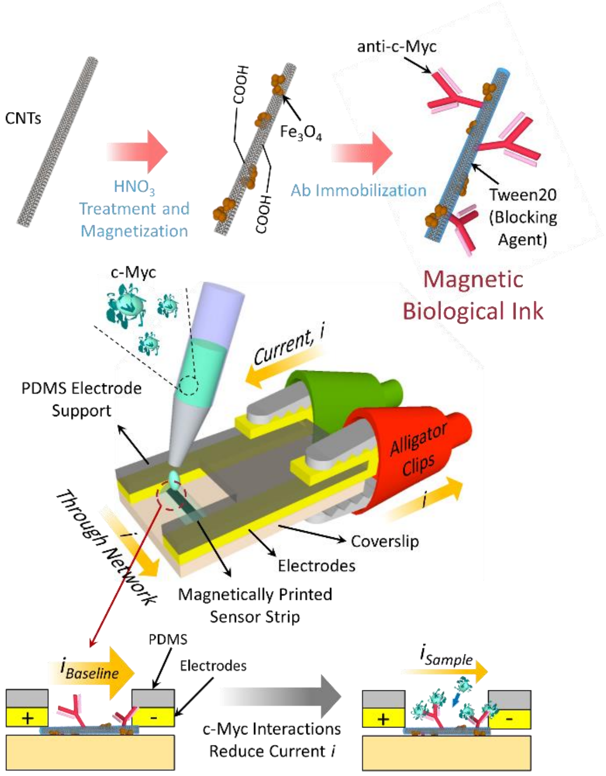

Figure 4.2: Synthesis of the magnetic biological ink and its use to print a c-Myc sensor. MWNTs are treated with concentrated nitric acid, which produces unsaturated carboxylic (–COOH) groups on the surface. Some of these groups act as nucleation sites for the *in situ*

co-precipitation of magnetite (Fe_3O_4) nanocrystals and the remainder are available for anti-c-Myc amine (–NH_2) groups to form covalent bonds with the MWNT surfaces. The magnetic biological ink is then deposited onto a glass substrate using a pipette where it dynamically organizes under the influence of an external magnetic field and prints an electrically conducting pattern.

Following activation and magnetization of the MWNTs, Ab immobilization was performed. For each mg of MWNTs contained in the mMWNTs, 2 mL of deionized water was used as media to disperse the precursor magnetic ink in solution with a probe sonicator (15 seconds, 30% amplitude). Corresponding to the amount of MWNTs, an anti-c-Myc:MWNT weight ratio β = 2.5×10^{-4} value was selected and an appropriate amount of Ab (0.5 µL, 0.5 mg mL^{-1}) was added to the mMWNTs (1.4 mg) in solution. The mixture was incubated for 1 hour at room temperature, inverted gently every five minutes to maintain the suspension, or when sedimentation of the magnetic biological ink was observed. Following incubation, the supernatant was removed.

A blocking procedure was then performed to prevent non-specific binding of Ag molecules to the magnetic biological ink. Blocking of the MWNT surface ensures that the detected signal is directly related to the specific Ag-Ab interaction, reducing noise that may originate due to adsorption of non-specific molecules [226, 251]. For every 1 mg of aMWNTs, 2 mL of blocking solution (0.1% Tween 20 in deionized water) was added to the magnetic biological ink [229]. The ink was blocked for a half hour at room temperature, inverted gently every five minutes to ensure saturation of the ink surface. Following incubation with the blocking solution, the blocked ink was washed three times in deionized water. A final concentration of 10 mg/mL was obtained by adjusting the amount of DI water. The same approach was followed for the case when MNPs and Ab were adsorbed on the MWNT surfaces. These biological inks are used to print patterns between electrically conductive electrodes. Once the pattern evaporates, the resulting feature is used as a biosensor that measures its electrical response to deposited samples. The measurements are capable of distinguishing between varying picomolar concentrations of c-Myc within 60 seconds (Figure 4.2).

4.3.5 Electrical Circuit, Sensor Assembly and Sensing.

To investigate the sensing capability of the dried ink, a voltage divider circuit was used with a reference resistance of R_{ref} = 100 kΩ. A square PDMS (2.5×2.5×0.3 cm) section was used to support two aluminum foil electrodes. The electrodes were separated by 5 mm and fixed to the PDMS support using double-sided tape. A cutout (1×0.5 cm) through the PDMS support was centered between the electrodes to allow sample deposition on the ink strip. The electrodes were wrapped around this support to provide electrical access with alligator clips. The PDMS electrode assembly was positioned on the top of the sensor, while the alligator clips held the sensor assembly together mechanically. This ensured good connection between the ink network and the aluminum electrodes. Each electrode covered a ~1 mm section of the sensor, leaving another 5 mm ink strip exposed for sample deposition and therefore Ag detection. The printed sensor of resistance R_s was connected in series with R_{ref}. A PLC (Arduino Uno) supplied the circuit with a 5 V DC power supply, while an analog feedback voltage allowed the PLC and computer unit to interpret and sample the current i passing through the circuit at a frequency of 10 Hz. After each test, the electrodes were wiped with ethanol (100%) and left to dry to ensure that no cross contamination occurred.

4.3.6 Characterization Methods

XRD analysis of MWNT and mMWNT powder samples was performed using a Bruker D8 Discover instrument comprising a Davinci^{TM} diffractometer operating at 35 kV and 45 mA using Co-K_α radiation (λ_{avg} = 1.79026 Å). Bruker's DIFFRAC.Eva V3.1 software was used for qualitative analysis of the constituent phases. Transmission electron microscopy (TEM) and electron energy loss spectroscopy (EELS) spectroscopy were with a JEOL 2010F field emission microscope. For TEM, the samples were suspended in ethanol, dripped on to a TEM grid and then wicked off with a tissue wipe. Optical and fluorescence (Enhanced Green Fluorescent Protein, EGFP) microscopy were conducted using a Zeiss Axio Observer.Z1. Magnetization measurements were performed using SQUID magnetometry at room temperature. Electrical conductivity measurements were performed using a VWR SympHony conductivity probe (Model B40PCID). The suspension stability was measured using a dynamic light scattering and zeta potential measurer (Malvern Instruments, Model: ZEN3600 - Zetasizer Nano ZS). The zeta potential ζ is the potential difference between the dispersion medium and the thin stationary layer of fluid on the surface the particle. The potential indicates the degree of repulsion between charged particles in dispersion, where large ζ is indicative of stability [252].

4.4 Results and Discussion

4.4.1 Magnetoresponsive Conductive Colloids (MCCs)

The MCC densities and compositions (γ =1) are presented in Table 4.1. The compositions of the colloidal suspensions were measured by drying samples of known weight and volume before adding the surfactant solution that had a specified concentration. The 1.22 g/cm^3 density of MCC2 is slightly lower than the 1.26 g/cm^3 densities of MCC1 and MCC2. This small variation can be explained by the difference in the chemical composition of the MNPs. The three fluids exhibit different visual responses toward magnets. MCC1 has the strongest response, as shown in Figure 4.1b, which is reasonable since it is based on sample S1 that has the highest M_s = 30.6 emu/g.

Material Phase	MCC1	MCC2	MCC3
MNPs	Fe_3O_4	$Mn_{0.2}Cu_{0.2}Zn_{0.6}Fe_2O_4$	$Cu_{0.4}Zn_{0.6}Fe_2O_4$
mMWNT wt%	4.1%	3.9 %	4.1 %
TMAH wt%	10%	10 %	10 %
H_2O wt%	85.9%	86.1%	85.9%
Density (g/cm^3)	1.26	1.22	1.26

Table 4.1: MCC compositions and densities. In all MCCs, ≈4 weight percent of mMWNT was dispersed in 10 weight percent TMAH aqueous solution. The densities of the three MCCs are almost similar and lie between 1.22-1.26 g/cm. The small variations occur due to the different MNP weight percentages and chemical compositions.

As shown in Figure 4.3a, the ions in the surrounding medium rearrange around the ends of the conductive MWNTs when they are polarized with an applied electric field E_a. This shortens the ion transport path in the direction of polarization and decreases the effective electrical resistance of the colloidal suspension as per Coulomb’s law [151, 155]. DI water has a relatively poor electric conductivity of 0.005 mS.cm^{-1}, as shown in Figure 4.3b. Its conductivity is enhanced to 90.5 mS.cm^{-1} by simply dissolving ten percent TMAH by weight. Adding another 4 weight percent of mMWNTs further increases the conductivity by 65% for MCC1 (to 149.5 mS.cm^{-1}), 78% for MCC2 (to 161 mS.cm^{-1}) and 90% for MCC3 (to 169.5 mS.cm^{-1}). MCC3 consisting of MNPs with the highest copper content facilitate the highest electric conductivity, which shows how increasing the Cu content in an MNP improves the electric conductivity of its MCC.

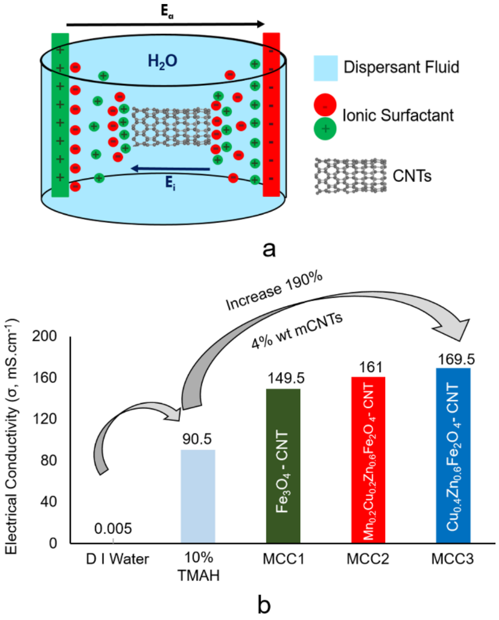

Figure 4.3: MCC Electrical Conductivity. (a) MWNTs placed in an ionic medium between two electrodes charged by an electric field E_a polarize and become oriented along the direction of the field. This MWNT orientation shortens the ion transport path, decreasing the effective electrical resistance of the colloidal suspension. (b) Dissolving 10% (w/w) of tetramethyl ammonium hydroxide (TMAH) in DI water increases the electrical conductivity σ to 90.5 mS cm^{-1}. Dispersing 4% (w/w) of the different mMWNTs in the TMAH solution enhances σ by 65-90%.

Figure 4.4 presents the measured apparent zeta potential ζ for the three MCCs, which are -32.5, -33.2, -33.1 mV for MCC1, MCC2 and MCC3, respectively. Since the peak ζ value is larger than 30 mV, all three MCCs have moderate colloidal stability [253].

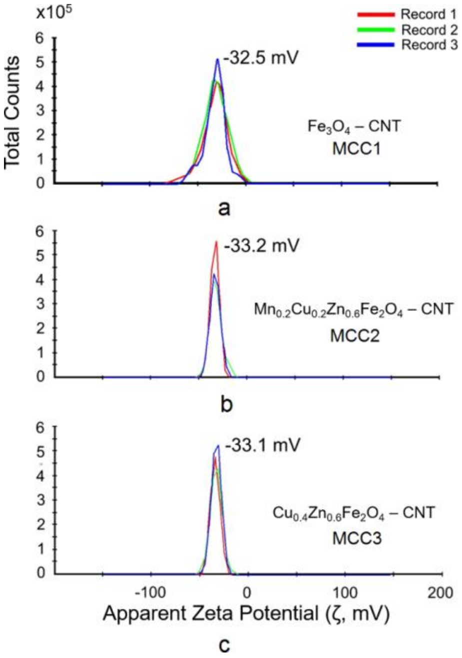

Figure 4.4: Apparent Zeta Potential Distribution. All three samples show a similar mean zeta potential (N = 3), of $\zeta \approx 33 \text{ mV}$, which indicates moderate colloidal stability.

4.4.2 Adaptation of mMWNT for the Magnetic Biological Ink

The first step during ink production requires that MWNTs be treated with concentrated HNO_3, which creates surface sites where reactive molecules, such as COOH, C=O, and C–OH, form covalent bonds with the MWNT scaffold and where magnetite nanocrystals (Fe_3O_4) are subsequently nucleated [254]. The material characterization of the mMWNTs is shown in Figure 4.5-4.7. XRD, TEM and SQUID measurements confirm that the MWNTs are successfully decorated with crystalline Fe_3O_4 magnetic nanoparticles.

XRD analysis of dried mMWNTs was conducted for the three Fe_3O_4: MWNT weight ratios $\gamma = 0.1$, 0.2, and 0.4. Figure 4.5 shows that all samples consisted only of the intended magnetite and carbon phases. The powder diffraction file (PDF) database, available through the Eva software, qualitatively confirmed that all three samples contain hexagonal carbon (CNTs, PDF No. 00-058-1638) and the spinel magnetite phase (Fe_3O_4, PDF No. 01-071-6336). The average size of the Fe_3O_4 nano-crystals was calculated through the Scherrer equation (3.3) applied at the highest diffraction peak (311). For all three samples, the MNP sizes lie in a narrow 8.6–10.3 nm range. Using Bragg's Law [18], calculations of the average lattice parameters of Fe_3O_4 are 8.403, 8.396 and 8.404 Å for $\gamma = 0.1$, 0.2, and 0.4. These values agree with those for magnetite (8.394 Å, JCPDS No. 79-0417; and 8.400 Å, COD card No. 1011084). For all three cases, TEM images at various magnifications in Figure 4.6 show that the MWNT surfaces are decorated with MNPs that have high crystallinity and a narrow crystallite size distribution around ~10 nm. Increasing γ improves the decoration density.

Because of their small sizes, the magnetite nanoparticles are superparamagnetic [92] with a high saturation magnetization. Conjugating the MNPs with the diamagnetic MWNTs retains this superparamagnetic behavior, which is evident in Figure 4.7 since the measured hysteresis loops for all of the cases indicate that there is no remanence or coercive field. The magnetic saturations $M_s = 3.03$, 7.79, 15.09 emu/g for $\gamma = 0.1$, 0.2 and 0.4. A higher M_s value translates into a stronger magnetic response for the conjugate material, which assists magnetic printing, producing a denser and more electrically continuous biosensor strip. Being superparamagnetic, dipole-dipole interactions in the conjugate material are limited in the absence of a magnetic field, for instance during storage, which reduces nanoparticle aggregation, allowing repeatable sensor printing.

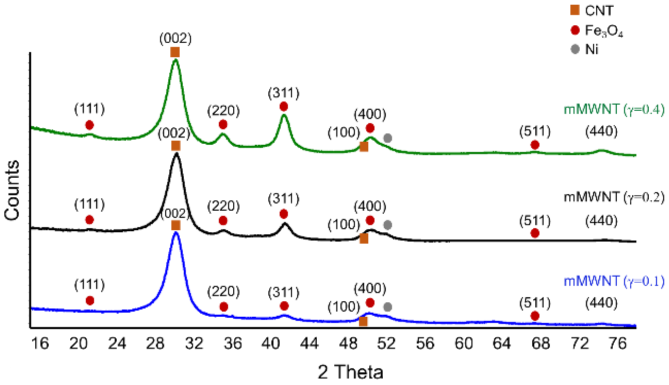

Figure 4.5: X-Ray Diffraction Analysis of mMWNTs. The XRD (Co K_α, λ=1.79 Å) patterns for magnetite:MWNTs weight ratios γ = 0.1, 0.2, and 0.4 which confirm the presence of a magnetite (Fe_3O_4) phase and a hexagonal carbon phase from the carbon nanotubes.

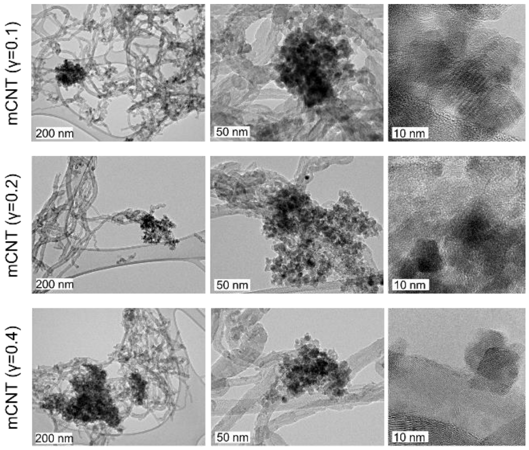

Figure 4.6: TEM images of mMWNT samples at various magnetization weight ratios γ = 0.1 to 0.4 (from top to bottom) confirm that all samples have been successfully decorated with crystalline MNPs synthesized within a narrow size distribution around ~10 nm.

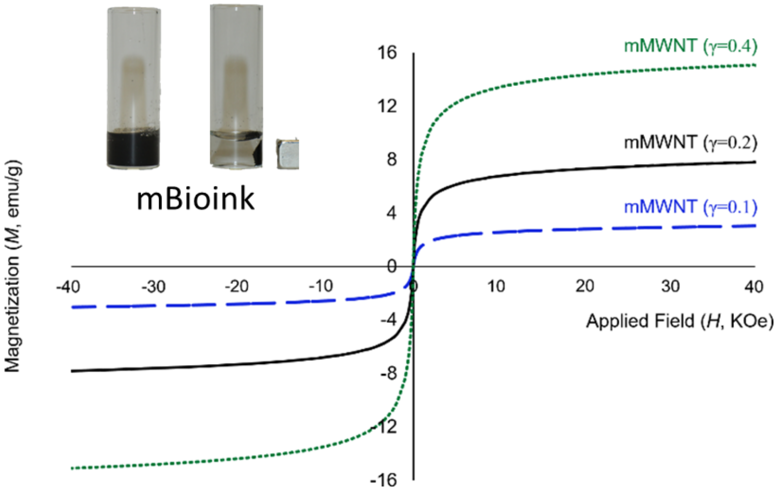

Figure 4.6: Magnetic Characterization. Magnetic hysteresis curves show that all mMWNT samples exhibit superparamagnetic behavior, but have different saturation values M_s depending on their magnetite content (γ). The greater this content, the stronger is the material response to a magnetic field.

4.4.3 Visualization of Ab Immobilization onto MWNT Surface

The MWNT surfaces are functionalized with anti-c-Myc Abs through two pathways. The relatively low MNP yield allows some active carboxylic groups to remain post magnetization. Hence, subsequent addition of anti-c-Myc allows the Ab to become covalently bonded even without intermediate reagents [244] through a condensation reaction between the Ab amine groups and the remaining carboxylic groups on the mMWNT surfaces [226, 227, 229, 255-257]. Alternately, Abs can also be physically adsorbed on this surface but, as we explain later, Ab-Ag binding kinetics cannot be determined using the biosensor in this case. The final ink preparation step involves dispersing the mMWNT-Ab hybrid nanoparticles in an aqueous solution of Tween 20 (polysorbate 20), which acts as a blocking agent, coats the MWNT surface, and prevents non-specific Ag-Ab binding.

The binding of Ab molecules to MWNTs is visualized through fluorescent microscopy. Secondary Ab, fluorescein isothiocyanate (FITC)-conjugated Donkey anti-Mouse IgG H&L, is used to create a fluorescent ink, for which the Ab:MWNT weight ratio $\beta = 2.5\times10^{-4}$. The fluorescence intensity is invariant to the Fe_3O_4:MWNT weight ratio γ in the range 0.1-0.4, as shown Figure 4.8a–c, i.e., the magnetization of MWNTs has a negligible impact on Ab immobilization on the nanotube surfaces. Hence, MWNTs magnetized with $\gamma = 0.4$, which exhibit robust magnetic response, are used to fabricate the biosensor strip.

The fluorescence images for MWNT samples with covalently bonded Abs in Figure 4.8a–c are virtually indistinguishable from the image in Figure 4.8d, which reveals Abs that are adsorbed onto as-manufactured nanotube surfaces that do not contain functional groups. Thus, for the particular Ab:MWNT weight ratio used, there appears to be no difference in Ab immobilization on nanotube surfaces corresponding to (1) mMWNTs, or (2) as manufactured MWNTs that have no surface functional groups at acid-induced defect sites. There is no fluorescence in the absence of Ab conjugation, i.e., when $\beta = 0$, see Figure 4.8e, confirming that the fluorescence sources in Figure 4.8a–d are due to FITC-labeled Abs only.

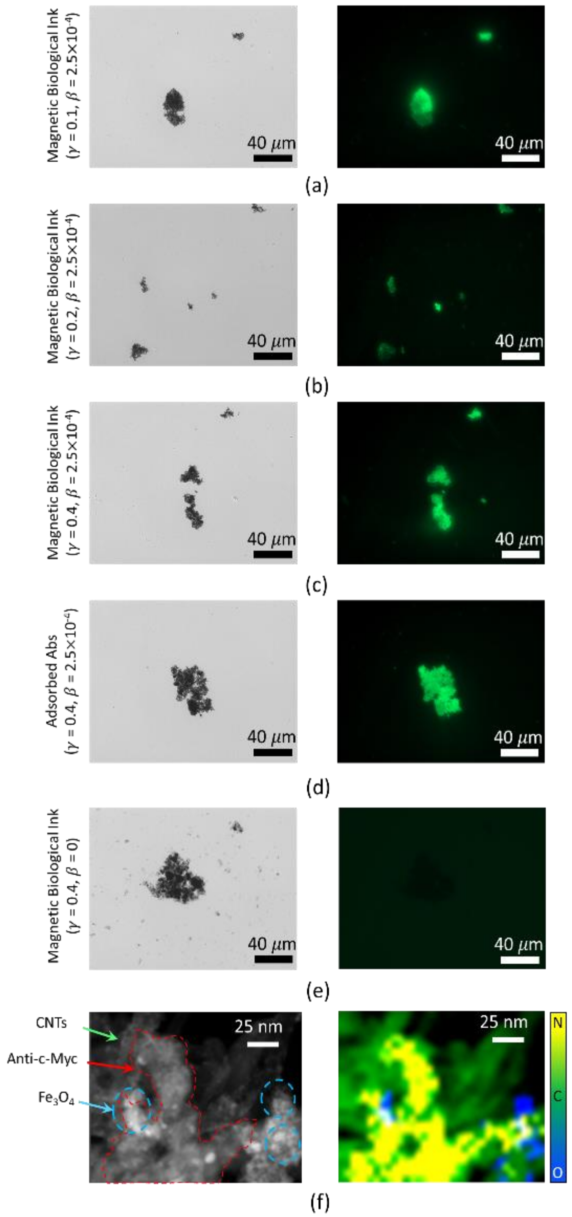

Figure 4.8: Visualization of Ab immobilization on the surface of mMWNTs. First, FITC-labeled fluorescent Abs are employed to confirm Ab immobilization on the surface of mMWNTs for an Ab: MWNT weight ratio β = 2.5×10^{-4} in an ink where Abs are covalently bonded with mMWNTs that have Fe_3O_4: MWNT weight ratios (a) γ = 0.1, (b) γ = 0.2 and (c) γ = 0.4, and (d) for an ink that contains adsorbed Abs on mMWNTs with γ = 0.4. For (e) β = 0, γ = 0.4, no fluorescence is observed from MWNTs and Fe_3O_4, confirming that the fluorescence observed in (a)-(d) originates from FITC-labeled Abs only. No visual

differences in fluorescence are detected for samples containing different weight ratios of magnetite, and those containing adsorbed and covalently bonded immobilized Abs. (f) STEM and EELS micrographs reveal the presence of elemental carbon (C), oxygen (O) and nitrogen (N). The nitrogen, which is present only in Anti-c-Myc Abs, confirms Ab immobilization on the conductive MWNT network.

Since anti-c-Myc Ab is non-fluorescent, an electron energy loss spectrum (EELS) is performed to identify Abs on the mMWNT surfaces. Figure 4.8f depicts a scanning transmission electron microscopy (STEM) micrograph and the corresponding EELS spectrum for the ink. The spectrum highlights locations where elemental C, O and N are present. Since N originates solely from the Abs and no other ink component, its map reveals anti-c-Myc locations. The micrograph uncovers a general structure that consists of a MWNT-Fe_3O_4-Ab network, where the MWNT mesh produces the electrical path and the Abs are Ag receptor sites.

4.4.3 Fabrication of the Bio-sensor

The device is fabricated as shown in Figure 4.9a. A 10 μL volume of the magnetic biological ink is deposited with a micropipette over a 7 mm length on a glass coverslip directly above one of the magnet edges, which concentrates the magnetic field locally, which dynamically self organizes the magnetized and Ab-functionalized MWNTs into a dense electrically conducting strip. After it is printed, each sensor is dried for 20 minutes at room temperature in the presence of the magnetic field, which maintains the integrity of the mMWNT-Ab conjugate. When the dispersing medium (DI Water) has evaporated, dried printed sensor strips of ~7 mm length and ~1.5 mm width remain on the coverslip, held in place by Van der Waals and electrostatic forces. Despite visual observations of cracks, strips at different times exhibit identical sensing responses to various samples.

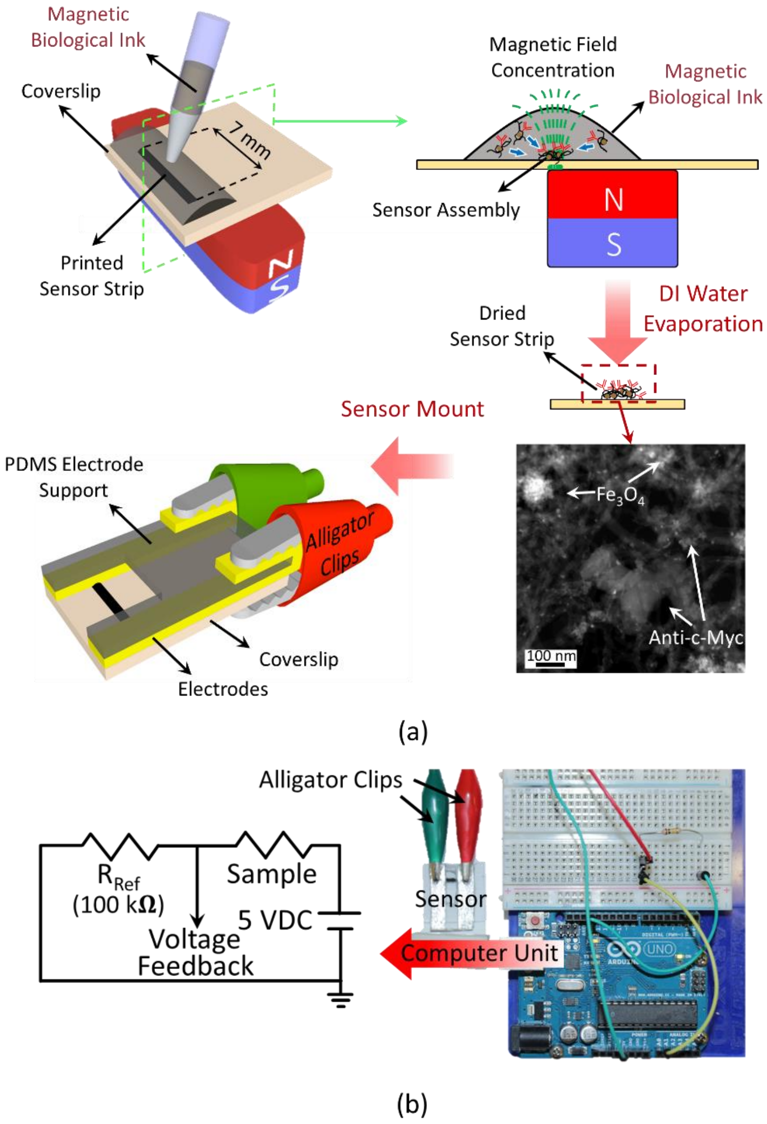

Figure 4.9: Printing technique and sensor assembly. (a) 10 µL of the magnetic bioink is deposited on top of a glass coverslip that is placed on a permanent magnet. The applied magnetic field concentrates and self organizes the functionalized mMWNTs on the substrate. After the supernatant in the ink is evaporated, a patterned strip of densely packed Ab-functionalized MWNTs remains deposited on the substrate, which forms the sensor.

The STEM micrograph identifies MNPs and anti-c-Myc that constitute the print based on the magnetic bioink. Electrodes are readily connected to either end of the strip, providing current to the sensor. (b) A voltage divider with a reference resistor R_{ref} = 100 kΩ monitors current changes that measure the biosensor responses to the various samples that are deposited on it.

Typically, each sensor consists of ~100 μg of MWNTs, ~40 μg of Fe_3O_4 and ~25 ng of anti-c-Myc Ab, i.e., the material usage per sensor is small. Hence, the material cost of a printed sensor is lower than 20 cents (Canadian). The sensor is integrated with electrodes using a polydimethylsiloxane (PDMS) support and alligator clips that connect the strip to an electrical circuit. With a reference resistance R_{ref}, an external circuit is used to measure real-time current changes when samples are deposited on the biosensor, see Figure 4.9b.

4.4.4 Sensing Measurements

Two types of tests are performed. (1) A sample is deposited once on the surface of the printed biosensor strip, and (2) equal amounts of the sample are deposited repeatedly after specific intervals on the sensor surface. Three tests are performed with every sample, each with a newly printed biosensor. Figure 4.10a presents temporal responses when 2 μL of (1) purified c-Myc with 40, 20, and 10 pM concentrations, (2) DI water, and (3) 40 pM concentration of bovine serum albumin (BSA) are placed on the biosensor. The BSA is a nonspecific Ag towards anti-c-Myc Ab and is therefore a negative control.

Figure 4.10a shows that after sample deposition at time t = 2s on an initially dry biosensor, the current i_s decreases rapidly from its initial value $i_b \approx$ 47 μA before reaching steady state. Both DI water and BSA samples induce similar decreases in the biosensor current. In contrast, i_s does not level off as quickly when c-Myc is deposited on the strip, but continues to decrease below the steady values reached for DI water and BSA. The biosensor responds differently to c-Myc sample deposition due to the Ag-Ab binding kinetics since the interaction of anti-c-Myc Ab with the specific c-Myc Ag increases the electrical resistance of the sensor, which in turn decreases i_s [258, 259]. Nonspecific interactions of anti-c-Myc with DI water and BSA do not decrease i_s as significantly below its initial value. The relatively slow Ag-Ab binding kinetics induce the gradual current reduction.

The biosensor responses shown in Figure 4.10a underscore the specificity with which the ink detects c-Myc. Increasing the Ag concentration enhances Ab binding and thus, the electrical resistance of the sensor strip, which leads to a larger current reduction and steeper temporal current gradients di_s/dt, as shown in Figure 4.10a. The values of i_s at t = 60 s for the 40, 20, and 10 pM c-Myc concentrations are 34.6±0.5, 38.8±0.4, and 40.9±0.1 μA, respectively, confirming that current reduction scales with increasing Ab concentration.

During $30 < t < 60$ s, the gradient di_s/dt is constant, which also correlates with the c-Myc concentration. Figure 4.10b presents the ratio $i_{s,a}/i_{s,a,30s}$, where $i_{s,a}$ is the temporal current at time t averaged over three repetitive tests for a sample and $i_{s,a,30s} = i_{s,a}$ at t = 30 s. Figure 4.10c reveals linear correlations between the current gradients obtained from Figure 4.10b and the c-Myc concentrations. These correlations are in agreement with reported responses for CNT-based biosensors [226, 243, 244]. By simply monitoring the sensor's transient electrical response, it is possible to rapidly identify c-Myc positive samples with different concentrations. This makes Ag monitoring feasible without using additional reagents and sophisticated electrical equipment that is typical of other biosensors [244].

Acid treatment of MWNTs provides functional groups at defect sites on the nanotube surfaces, which promote the covalent immobilization of Abs. During sample deposition, Ag-Ab interactions at defect sites, where Abs are now immobilized, restrict current transport over time significantly, amplifying Ag detection [258, 259]. Hence, when anti-c-Myc Abs are not covalently bonded to a MWNT but are instead physically adsorbed, we have determined that the Ab-Ag binding kinetics cannot be measured with the biosensor.

The response of the biosensor to successive 1 μL sample depositions is presented in Figure 4.10d for three types of biosensor strips that are printed with three different inks. These inks contain (i) covalently mMWNTs that have not yet been functionalized with Abs (ink 1), or (ii) MWNTs that have both Fe_3O_4 nanoparticles and anti-c-Myc Abs adsorbed on their surfaces (ink 2), and (iii) MWNTs that are covalently magnetized with Fe_3O_4 nanoparticles and contain both covalently bonded and adsorbed anti-c-Myc Abs on their surfaces (ink 3). The functionalized MWNTs for all three inks are dispersed in DI water containing 0.1% Tween 20.

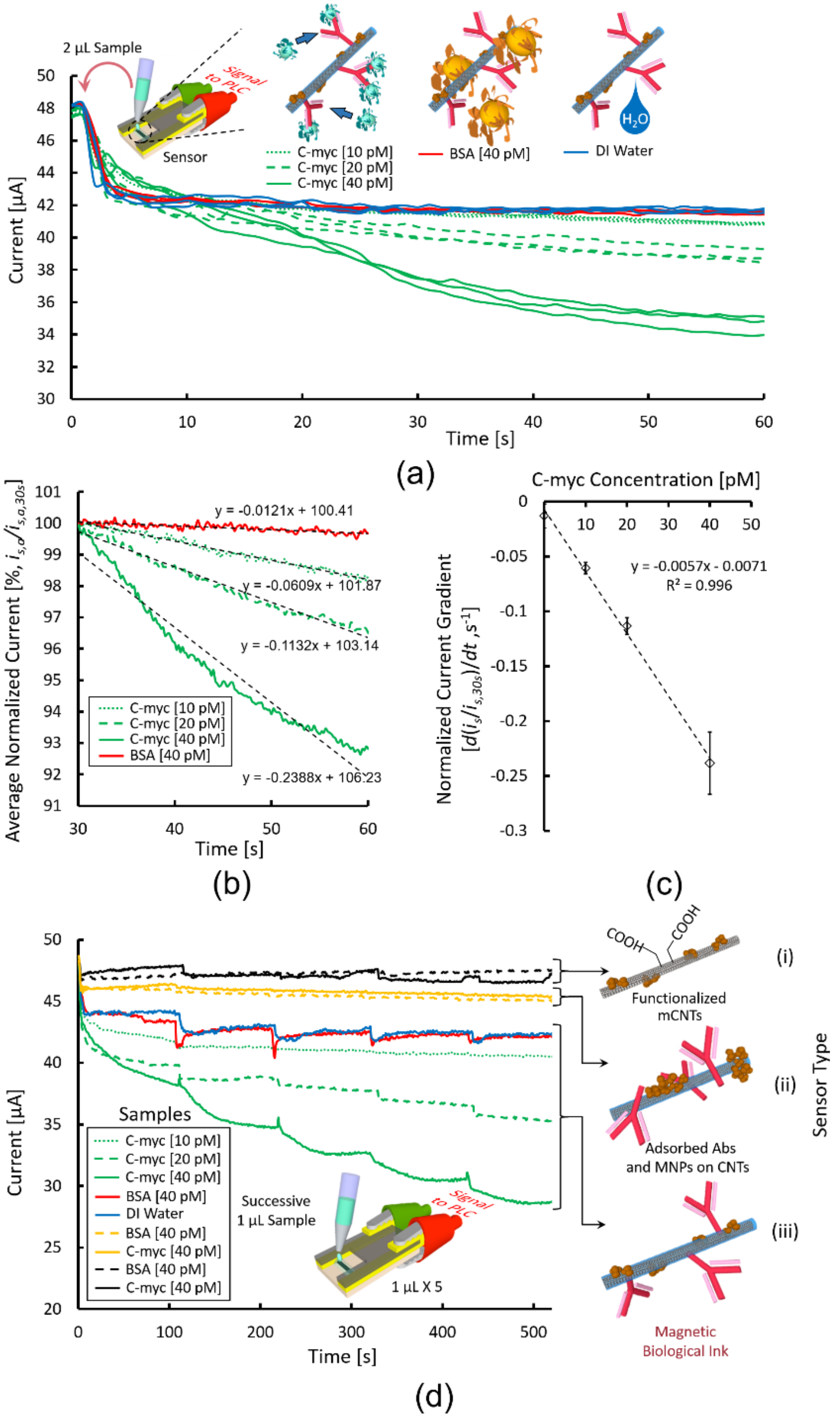

Figure 4.10: Biosensor transient response. (a) Immediately after 2 μL samples are deposited on the sensor strip, the DI water and BSA samples induce a rapid decrease in electrical current, which subsequently levels out. In contrast, since the sensor is inherently

sensitive to c-Myc Ag interactions due to the anti-c-Myc Abs that are covalently bonded to the surfaces of MWNTs, the current for all c-Myc samples decreases to levels below those measured for DI water and BSA deposition, which offers proof of targeted detection and sensor specificity to c-Myc Ags. The higher the c-Myc concentration in a sample, the larger the current decrease it induces. All of the deposited c-Myc samples produce a steady current decrease during the period 30 s < *t* < 60 s. Normalizing the average current over that duration leads to the quasi-linear response shown in (b). There is a linear correlation in (c) between the normalized current gradients in (b) and the corresponding c-Myc concentrations. **Biosensor response to successive 1 μL sample additions.** (d) Acting as a control, magnetized MWNTs that are not functionalized with Abs (i) cannot distinguish between 40 pM BSA and c-Myc samples, black dashed and solid curves respectively. When anti-c-Myc is immobilized on the MWNT surfaces through adsorption, again (ii) there is insufficient discrimination between these two samples. In contrast, a sensor fabricated using an ink in which anti-cMyc is attached to the MWNT surfaces through acid functionalization, (iii) clearly distinguishes between the two negative control samples, DI water and BSA, and the Ag of interest, c-Myc.

Biosensors printed with inks 1 and 2 do not discriminate between 40 pM c-Myc Ag and 40 pM BSA, i.e., they produce similar responses for these two samples and it is not possible to positively detect c-Myc by printing biosensor strips with these two inks. Differences between specific (c-Myc) and non-specific (BSA) samples are apparent only with biosensors that are printed with ink 3. With ink 3, the 40 pM c-Myc sample produces the largest current reduction, followed by the 20 pM and 10 pM c-Myc samples. When a 5 μL sample containing c-Myc Ags is deposited on the biosensor in 1 μL increments, the successive sample additions continue to increase the electrical resistance and decrease the sensor current.

4.5 Conclusion

MWNTs were decorated by *in situ* co-precipitation with different magnetic nanoparticles (MNPs). These magnetized MWNTs (mMWNTs) were successfully suspended to create novel and hitherto unreported magnetoresponsive conductive colloids (MCCs) that have moderate colloidal stability. The MCC synthesis merges processes used to produce ferrofluids and mMWNTs, which is another novelty. Three magnetoresponsive conductive colloids were successfully prepared using these three types of the MNPs ($\gamma=1$). All colloids have moderate suspension stability since their mean zeta potential $\zeta \approx$ -33 mV. Their electric conductivities of 150-170 mS.cm^{-1} are much higher than the conductivity of the deionized water dispersing medium that is a poor conductor. The chemical composition of the MNPs that decorate an mMWNT influences the electric conductivity of their MCC. For instance, increasing the copper content in an MNP improves the MCC electric conductivity. In summary, we have provided a novel methodology to produce stable magnetoresponsive conductive colloidal suspensions with tunable magnetic and electrical properties. These colloidal suspensions are a promising new class of material that could be used for applications where a magnetic response, or action from a distance, must be coupled with a viable material electrical conductivity.

By the adaptation of MCC’s synthesis, a biological magnetic ink is synthesized that contains Abs immobilized on the surfaces of mMWNTs that are dispersed in DI water containing Tween 20 as bio-compatible surfactant. Ink synthesis is straightforward and does not involve complex chemistry or use of intermediate reagents. An applied magnetic field dynamically self organizes the magnetized and functionalized CNTs, printing them into an electrically responsive strip that serves as a biosensor to detect specific Ags. Unlike previous methods, a magnet is not required during sensing, facilitating simple integration of the sensor into an electric circuit. The sensor detects picomolar c-Myc concentrations within a minute and distinguishes between c-Myc and BSA samples of different concentrations through decreases in the sensor current. These decreases, which occur due to real-time specific Ab-Ag binding kinetics, are larger at higher Ag concentrations. The detection technique is simpler, inexpensive and rapid as compared to typical cyclic voltammorgam analysis. Once the ink is synthesized, the time required to create a prototype sensor is less than 5 minutes, excluding ink drying time. Semi-quantitative Ag detection with picomolar sensitivity occurs within a minute after a sample is deposited on the biosensor. This proof of concept ink and sensor can be tailored to detect different Ags.

5. Magnetizing of MWNT via Non-covalent Functionalization (Ni-MWNT Hybrid Nanomaterials)

5.1 Introduction

In this chapter, an experimental investigations will be presented to highlight the magnetizing of the MWNT via non-covalent functionalization. We describe a nondestructive method to magnetize MWNTs and provide a means to remotely manipulate them through the electroless deposition of magnetic nickel nanoparticles on their surfaces. This nickel-MWNT hybrid nanomaterial was used to fabricate Ni-MWNT macrostructures and tune their morphologies by changing the direction of an applied magnetic field. These structures could find use in nano- and microscale filtration, as well as for printing electric circuits. Further, leveraging the hydrophilic Ni-MWNT outer surface, a water-based conductive ink was created and used to print a conductive paths with low electrical resistivity, illustrating the potential of this material for printing electronic circuits.

This chapter is reprinted from Material Research Express, *Fabrication of Nanoscale to Macroscale Nickel-Multiwall Carbon Nanotube Hybrid Materials with Tunable Material Properties*, 3, **Ahmed M Abdalla**, Tahereh Majdi, Suvojit Ghosh, and Ishwar K Puri, Copyright 2017, with permissions from IOP. The author of this thesis is the first author and main contributor of the above mentioned publication and has conducted all the experiments. The chapter will provide a literature review which is discussed in the background information section, followed by excerpts from the above mentioned paper.

5.2 Background Information

As uniaxial materials [99], carbon nanotubes (CNTs) must be axially aligned to fully exploit their superior electrical and mechanical properties [18, 100]. Magnetized CNTs can be manipulated and aligned using a remotely applied magnetic field [95, 96]. Coating CNTs with a magnetic metal also improves their oxidation resistance [99], electrical conductivity [139], adhesion to polymers [97], and ability to assume mechanical loads [260].

Like many other substrates, carbon nanotubes can also be coated with metals through electroless plating, a nondestructive, straightforward, and rapid method which can be performed under ambient conditions [97]. Electroless plating is applicable to any conductive or nonconductive substrate regardless of its size and shape [140]. Plating produces a coating layer of uniform thickness regardless of variations in the substrate thickness [261]. The resulting metal-CNT hybrid nanomaterial has relatively high surface area, electrical conductivity, tensile strength [141], and superior hardness, wear resistance and magnetic properties [97]. Such nanomaterials are used in sensors, electronic devices, catalytic and electrochemical technologies [141], and reinforced composites [260]. Nickel is a common ferromagnetic plating material. Electroless Ni deposition occurs through the *in situ* reduction of the metal from an ionic solution and leverages Van der Waals forces to form weak noncovalent bonds between the outer surface of the CNT and its surrounding metallic nanolayer [62].

An electroless process for plating multiwall carbon nanotubes (MWNTs) with nickel nanocrystals is schematically described in Figure 5.1 where nickel chloride is used as the metal ion source [146]. A reducing agent, sodium hypophosphite, provides electrons that reduce nickel ions (Ni^{2+}) into metallic nickel (Ni) using a catalyst [147]. To constrain the reaction on their surfaces, the MWNTs must be pre-treated with a catalyst prior to depositing Ni on their surfaces. The deposit forms a continuous Ni layer that encapsulates the MWNTs and is attached to their walls [149].

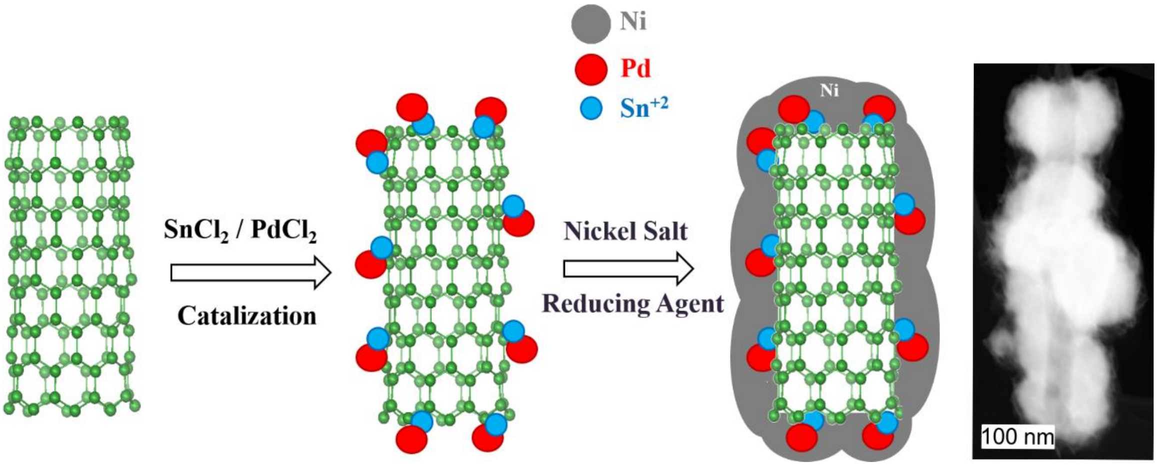

Figure 5.1: CNTs magnetized with Ni by Electroless Deposition. (a) MWNTs were catalyzed through two chemical treatment steps using acid solutions of $SnCl_2$ for sensitization and $PdCl_2$ for activation. Electroless deposition of Ni on the resulting activated MWNTs (aMWNTs) used a plating solution containing a nickel salt and a reducing agent, where nickel ions accept electrons from the reducing agent to form metallic nickel through metal reduction.

The catalysis consists of sensitizing and activating steps. Tin ions (Sn^{2+}) are used to sensitize MWNTs and palladium ions (Pd^{2+}) for activation [99, 178]. The Sn^{2+} and Pd^{2+} ions are dissolved in a dilute HCl solution, and catalysis is accelerated through sonication [147, 262]. The Sn^{2+} adsorbs on the MWNT surface during its sensitization and reduces Pd^{2+} to Pd during the subsequent activation step [178], i.e.,

$$Pd^{2+} + Sn^{2+} \rightarrow Sn^{4+} + Pd \,. \qquad (5.1)$$

As a catalyst, Pd initiates the reduction reaction that deposits Ni on MWNTs. Initially, this deposition occurs at preactivated sites, but once these are covered and shielded, subsequent accumulation occurs over existing Ni layers, which now act as new autocatalytic surfaces [263]. This form of electroless deposition is a redox process that consists of an oxidation reaction of the reducing agent and a reduction reaction of nickel ions [150], i.e.,

3. Oxidation $H_2PO_2^- + H_2O \rightarrow H_2PO_3^- + 2H^+ + 2e^-$, (5.2)
4. Recombination $H^+ + H^+ \rightarrow H_2$, and (5.3)
5. Reduction $Ni^{2+} + 2e^- \xrightarrow[CNT\ surface]{Catalyst} Ni$. (5.4)

Initially, deposition produces Ni nanoclusters, which, as the process continues, merge with neighboring clusters to produce a Ni layer over the MWNTs. When this metallic layer becomes continuous, the growth rate, expressed as volume per unit area is linear [263]. A cationic polymer can be applied as a dispersing agent to prevent the MWNTs from aggregating [149], and sodium citrate is generally used as an agent to prevents Ni from complexing [147]. Because we use sodium hypophosphite as the reducing agent, the Ni layers contain a small amount of phosphorus. While the Ni-P mixture is a good catalyst and resistant to sulfur [264], the inclusion of phosphorus is detrimental to the metal-CNT's magnetic properties [99].

We prepare Ni-MWNT hybrid nanomaterials (NiCH) with different nickel weight contents by electroless plating. The Ni:MWNT weight ratio γ (w/w) influences the morphology, thickness, and continuity of the Ni layers deposited on the MWNT, as well as the mechanical and magnetic properties of the NiCH that is produced. Plating a MWNT with the electrically conducting metallic layer decreases its contact resistance since the continuous Ni layer behaves as a conducting bridge connecting adjacent CNTs for $\gamma \geq 7$. A micro-composite structure is formed for $\gamma = 14$ and 30. The deposited Ni acts as a matrix, and the MWNTs are the reinforcing filler material. The as-prepared NiCH could have applications as a mesoporous material [141] although our future interest is to incorporate it into polymeric materials to produce composites with enhanced electrical and thermal conductivities, and electromagnetic interference shielding [146]. The magnetically susceptible nanostructures were fabricated into macroscale Ni-MWNT composites, where their structures were tuned by changing the direction of the magnetic field. The hydrophilic Ni surface improves the dispersion of the MWNTs in de-ionized water, which allowed us to create a conductive ink that rapidly prints an electrical circuit. Other applications of the material include nano- and microscale filtration, energy storage, and composite nanomaterials [265-268].

5.3 Methodology

5.3.1 Materials and Reagents

We used MWNTs produced by chemical vapour deposition (US Research Nanomaterials Inc.) with purity > 95%, outer diameter of 20-30 nm, inner diameter of 5-10 nm, and length between 0.5-2.0 μm as specified by the manufacturer. The other reagents used were nickel (II) chloride ($NiCl_2$, 98%, Alfa Aesar), nickel (II) sulfate hexahydrate ($NiSO_4{\cdot}6H_2O$, 99%, Sigma-Aldrich), sodium hydroxide (NaOH, 97%, Caledon Laboratory Chemicals), hydrochloric acid (HCl, 36.5-38%, Caledon), stannous chloride dihydrate ($SnCl_2 \cdot 2H_2O$, 98%, Caledon), ammonium chloride (NH_4Cl, ACS grade, BDH/VWR International), sodium citrate dihydrate ($Na_3C_6H_5O_7 \cdot 2H_2O$, 99%, EMD chemicals Inc.), sodium hypophosphite monohydrate ($NaH_2PO_2 \cdot H_2O$, lab grade, Anachemia Canada Co.), and palladium (II) chloride ($PdCl_2$, 100%, Artcraft chemicals Inc.). All reagents were used as received without further purification.

5.3.2 Catalyzing Carbon Nanotubes

The MWNTs were catalyzed through two steps [97, 141, 147, 263]. First, sensitized MWNTs were produced with 100 ml of stannous chloride solution consisting of 2g $SnCl_2$, 10ml HCl and 90ml deionized (DI) H_2O per each g of MWNTs. The sensitisation proceeded under sonication with a probe sonicator (Qsonica, LLC, Model: Q500 with 1/4″ micro-tip at 35% power) for 30 min. The sample was then filtered, washed with DI water, and finally dried in a vacuum oven at 70 °C for one hr. Next, each gram of sensitized MWNTs was activated with 100 ml of palladium chloride solution consisting of 0.03g $PdCl_2$, 2ml HCl and 98ml DI water. Again, activation proceeded with identical sonication. The sample was finally filtered, washed with DI water, and dried as before.

5.3.3 Synthesis of NiCH Nanostructures

Electroless plating of activated MWNTs proceeded by depositing nickel nanocrystals under stoichiometric conditions for the chemical reduction process designed to obtain $\gamma = 1$ (w/w) for Ni-plated CNTs (Ni: MWNTs) [147, 149, 262]. A gram of activated MWNTs was dispersed in 100 ml of DI water and sonicated with the probe sonicator (using the 1/4″ micro-tip at 35% power) for 20 min. Next, the plating solution (1.7g $NiCl_2$, 1.1g $NiSO_4 \cdot 6H_2O$, 5.5g NH_4Cl, 4g $Na_3C_6H_5O_7 \cdot 2H_2O$, 5g $NaH_2PO_2 \cdot H_2O$ and 100 ml DI water) was added, and the sonication continued for 60 mins. Sodium hydroxide solution (2N) was introduced during the sonication process to maintain a pH ≈ 9 during the plating process. After plating for 60 min, the sample was quickly filtered, washed with DI water, and dried in an oven at 200 °C for two hr. Employing the electroless plating process described above, stoichiometric calculations for samples SN1, SN2, and SN3 were implemented to respectively obtain $\gamma = 1$, 7, and 14 to explore the influence of γ.

5.3.4 Fabrication of NiCH Macrostructures

NiCH nanostructures with $\gamma = 1$ were dispersed in DI water using a probe sonicator. A strong magnetic field was applied to force their settling and alignment into two compact configurations, vertically (DM1) and horizontally (DM2), as shown in Figure 5.5. These configurations led to differently oriented Ni-MWNT macrostructures. Next, the plating solution was prepared as described in section 5.3.3 for a stoichiometric calculation for $\gamma =$ 30. Finally, the plating solution was slowly poured onto either aligned configuration under an applied magnetic field with no sonication applied while the pH was adjusted to 9 Electroless deposition was stopped after 60 min.

5.3.5 Ni-MWNT Water Based Conductive Inks

MWNTs are hydrophobic while nickel is hydrophilic. Hence, the Ni coating provides new functionality for the MWNTs by facilitating their compatibility with polar media [20]. This allowed us to prepare water-based conductive Ni-MWNT inks for rapid printing of electrical circuits (Figure 5.8a).

The preparation process is simple and rapid. A synthetized Ni-MWNT (γ=7) sample was dispersed in DI water using a probe sonicator. Different inks with varying volume contents of Ni-MWNT (γ=7) (i.e. 1, 2, 4, and 8 vol%) were prepared by dispersing the equivalent weight into the intended volume of water (where the material density was approximated as 8.05 g cm^{-3}). During printing, the inks were poured into a plastic mould (acrylonitrile butadiene styrene) with dimensions of 1 mm×1 mm×10 mm with and without the assistance of a magnet. The printed lines were dried over a hot plate at 60 °C. An MWNT-based ink was prepared with a volume content of 2% to compare with the Ni-MWNT-based inks.

5.3.6 Characterization Methods

X-Ray Diffraction (XRD) analysis of NiCH powder samples was performed using a Bruker D8 Discover instrument comprising a Davinci^{TM} diffractometer operating at 35 kV and 45 mA using Co-K_α radiation (λ_{avg} = 1.79026 Å). Bruker’s DIFFRAC.Eva V3.1 software was employed for qualitative analysis of the constituent phases. Scanning transmission and transmission electron microscopy (dark field STEM/TEM) and energy dispersive X-ray

(EDX) spectroscopy were conducted with a JEOL 2010F field emission microscope. For STEM/TEM, the samples were suspended in ethanol, dropped onto a TEM copper grid, then wicked off with a Kimwipe. Scanning electron microscopy (SEM) was conducted with a JEOL 7000F microscope equipped with a Schottky Field Emission Gun (FEG) filament. For SEM, the samples were suspended in ethanol and dripped onto a carbon tape on an aluminum stub. Magnetization measurements were performed using superconducting quantum interference device **(**SQUID) magnetometry (Quantum Design Inc.) at room temperature. Atomic Force Microscopy (AFM Bruker, Multimode 8 with ScanAsyst, NanoScope 9.1 software) was used to determine the elastic modulus. The AFM tip (TAP 525 A) with measured tip radius and deflection sensitivity of 10 nm and 121.3 nm/V (using the built-in Ramp mode), was calibrated with a reference material (Sapphire−12M, Bruker test sample kit) that had a known elastic modulus of 350 GPa. The natural frequency f_o and the spring constant k of the tip were calculated from the thermal tuning data to be 520 Hz, and 192.3 N/m, values which are in good agreement with standard values of 525 Hz and 200 N/m provided by the manufacturer. All measurements were performed using NanoScope Analysis 1.5 software. The samples were suspended in ethanol using a probe sonicator, dropped onto a stainless steel disc, and dried in vacuum oven.

5.4 Results and Discussion

5.4.1 Material Phases

The XRD analysis presented in Figure 5.2a shows that all NiCH samples contain the anticipated material phases and are devoid of other phases. All three samples contain crystalline nickel (Ni, PDF No. 00-004-0850) and hexagonal carbon (C_6, PDF No. 00-058-1638). Due to its relatively low content, the diffraction peaks of phosphorous (P, PDF No. 01-075-0577) could not be distinguished from noise. We found no evidence of the Ni/P alloy Ni_3P, which is reasonable since the samples were treated at a relatively low temperature of 200°C. The analysis confirmed the existence of Cassiterite (SnO_2, PDF No. 00-041-1445) in the samples, which likely formed due to the oxidation of Sn^{2+} to Sn^{4+} during the reduction of Pd^{2+} to Pd. Since a small quantity of $PdCl_2$ was used during the activation process, the Pd contained in the samples is lower than the instrument detection threshold.

The EDX/TEM results presented in Figure 5.2b confirm the existence of elemental C, Ni, P, Cu, Sn, and O. The copper arises from the TEM grid and Sn is detected in all three samples with a relatively small contribution. These results identify phosphorus as a byproduct in the Ni layer. Figure 5.2c presents EDX/ dark field STEM line-scanning results for the NiCH samples, which provide evidence of a uniform Ni coating around the MWNTs and the wavy features. The elemental composition is again confirmed to include carbon and nickel. As expected, the C:Ni ratio of these two elements decreases as γ increases.

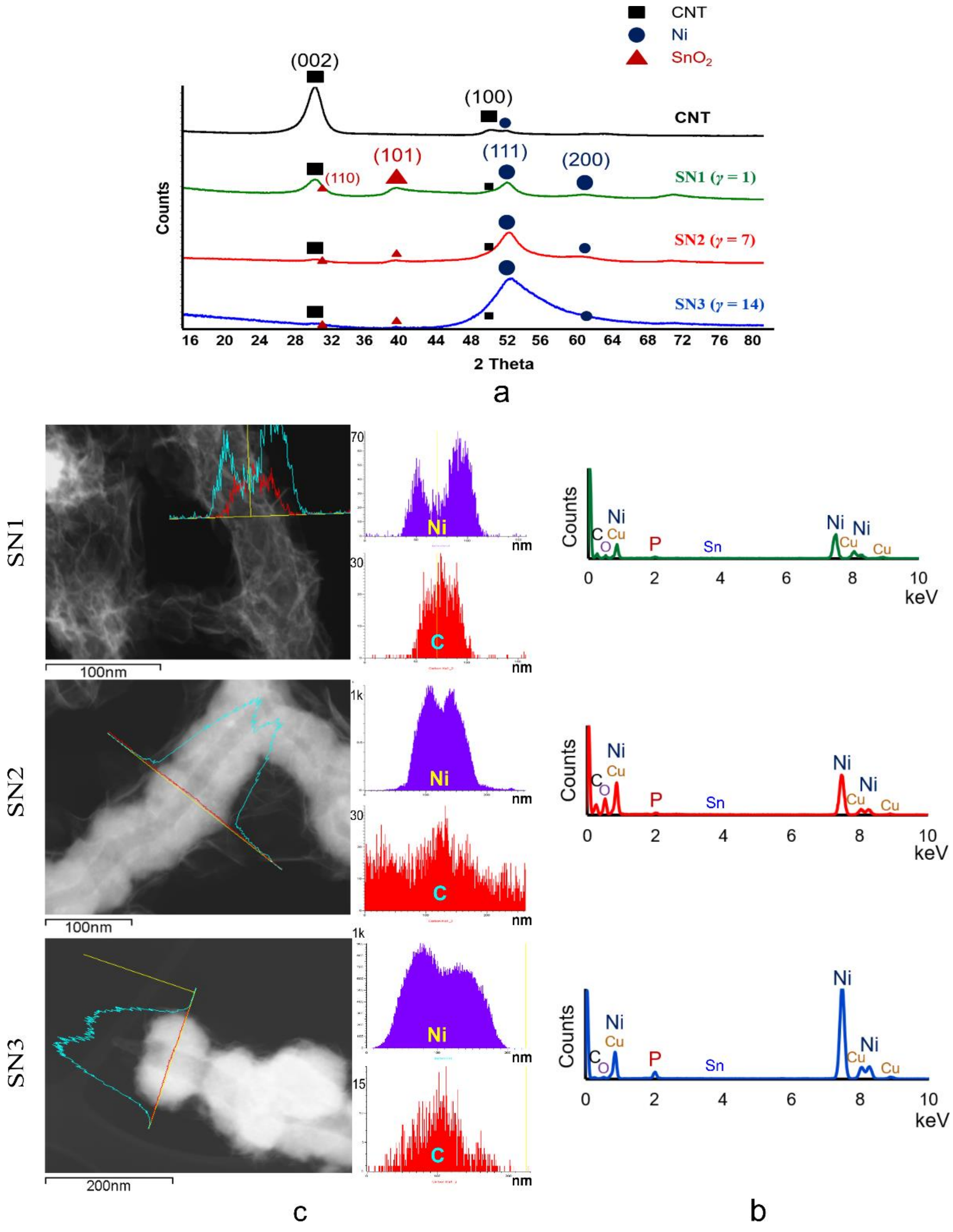

Figure 5.2: Phases analysis of the Ni-CNT (NiCH) hybrid nanomaterials. (a) The XRD (Co K_α) patterns for samples SN1, SN2 and SN3 show that a nanocrystalline nickel phase formed on the MWNT surfaces. Oxidation of Sn^{2+} to Sn^{4+} was inferred since no foreign phases were detected. There is also no evidence for the formation of a crystalline Ni_3P phase. Symbol sizes are varied to improve illustration. (b) The EDX analysis for SN1-SN3

shows a small phosphorous content as the reaction byproduct. (c) EDX/Dark Field STEM Line Scanning. Nickel forms a wavy coating around MWNTs with slight variations in the layer thickness and density. The measurements confirm the existence of MWNTs inside the coating layer and Ni as the major component of the outer coating.

The weight ratios,

$$\gamma = \frac{(\text{wt of Ni} - \text{MWNT hybrid}) - (\text{wt of aMWNT})}{\text{wt of aMWNT}}, \tag{5.5}$$

were calculated to be 1.1, 6.6, and 14.2 for SN1, SN2, and SN3, respectively, which vary slightly from the intended ratios of 1, 7, and 14. This indicates that even after activated MWNTs (aMWNTs) are fully coated with Ni, plating continues until all Ni in the source material is consumed, implying that while the Pd catalyst initiates the reaction, the plating becomes autocatalytic afterward.

Dark field STEM and TEM images at various magnifications (Figure 5.3) help visualize the NiCH produced for different γ. All images provide evidence of complete Ni coating on MWNTs and a certain coating thickness for a specific γ. Increasing γ increases the average thickness of the Ni layer, which is 10-15, 40-60, and 100-150 nm for γ = 1, 7, and 14, respectively. Increasing γ increases the Ni connections between plated MWNTs so that the sparse MWNT network for γ = 1 is much denser at γ = 14 when microscale NiCH structures are produced. In these latter microstructures, Ni is a conductive metallic matrix that contains MWNTs as the reinforcing filler.

High-resolution TEM images confirm that the plated Ni layer is crystalline, and the coating is in direct contact with the MWNT surfaces. SEM images of samples SN1 and SN3 (Figure 5.4) indicate that micron-size MWNT networks become interconnected as the nickel deposited on adjacent MWNTs merges. Thus, the conductive NiCH composite contains nanostructures for $\gamma = 1$ which become bulk structures when $\gamma = 14$.

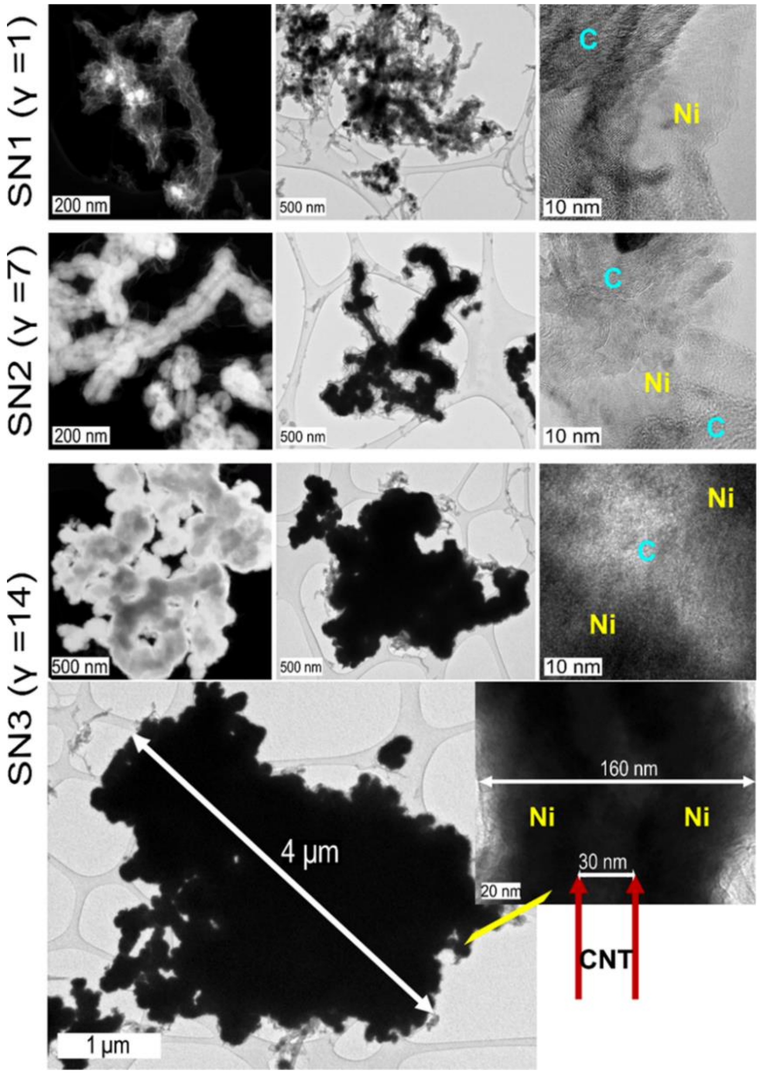

Figure 5.3: Dark field STEM/TEM images of samples SN1, SN2, and SN3 at different magnifications visualize the NiCH hybrid nanomaterial prepared through electroless plating for different weight ratios γ =1, 2, and 3. The average thickness of the Ni coating layer increases from 10 to 150 nm when γ increases from 1 to 14 in the three samples. All samples show continuous coating of Ni on the CNTs. Sample SN1 has a smaller Ni layer thickness and higher coating layer porosity while the coatings for samples SN2 and SN3

have larger thickness and better layer continuity. The Ni connections between MWNTs are more obvious for SN3, which is a microcomposite with Ni forming a conductive metallic matrix around reinforcing MWNTs.

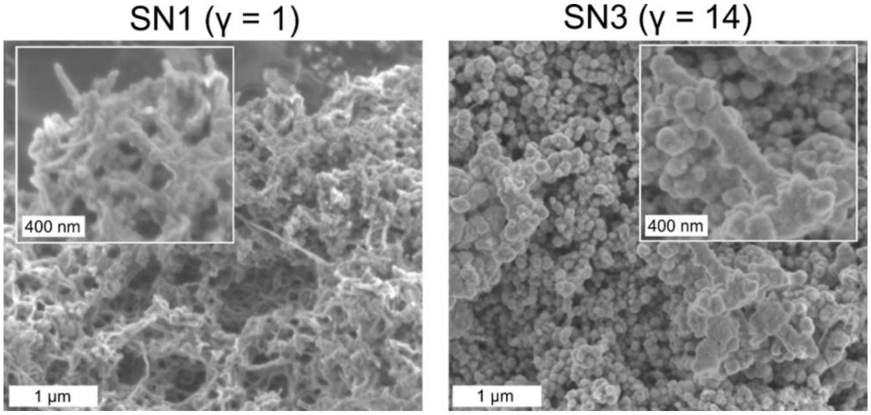

Figure 5.4: SEM images of samples SN1 and SN3 at two magnifications confirm the deposition of nickel in the form of merged Ni nanolayers that cover the outer surfaces of the MWNTs. Nickel links the MWNTs through conductive connections to produce micron-size networks.

5.4.2 Elastic Modulus

Using an AFM, the average elastic modulus *E* was measured in the radial direction for the pure MWNTs (S0) and for NiCH samples for γ =1 and 7 (SN1, and SN2 respectively). These three measurements were performed under similar AFM calibration conditions so that the resulting values are relative to the elastic modulus (*E* = 350 GPa) of the standard sapphire sample. Figure 5.5 shows AFM measurements over 1 μm square lateral cross-sections of S0 and SN1 and a 3 μm square lateral cross-section of SN2. Pure MWNTs have average *E* (*N*=20) ~ 12.5 ± 2.0 GPa, while samples SN1, and SN2 have larger *E* (N=20) ~ 18.3 ± 6.3, and 58.7 ± 22.1 GPa, respectively. This increase in the elastic modulus is attributed to the increase in the nickel content (γ from 0 to 7) and thickness (from 0 to 60 nm). Increasing the Ni:MWNT weight ratio γ from 0 (S0), to 1 (SN1), and finally to 7 (SN2) significantly increases E, showing that γ provides control and tunability over the NiCH elastic modulus.

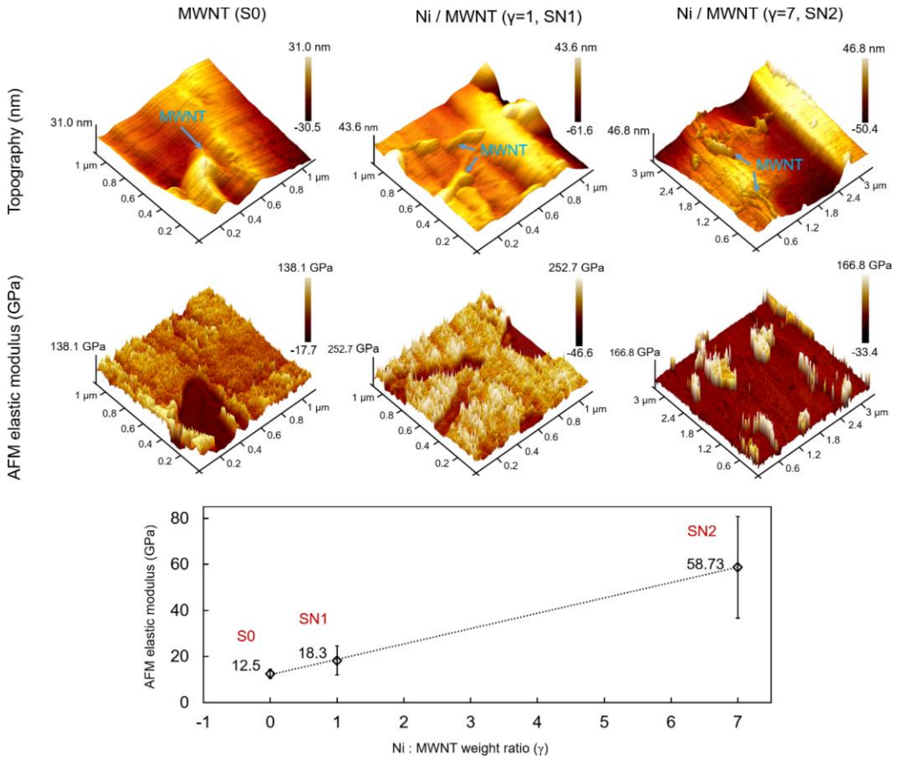

Figure 5.5: AFM topographical and mechanical sketch up of samples S0, SN1 and SN2. Pure MWNTs (S0) had an average elastic modulus $E \sim 12.5$ GPa while Ni-MWNT samples for $\gamma = 1$, and 7 had values of $E \sim 18.3$ (46% increase) and 58.7 GPa (370% increase), respectively. Increasing Ni:MWNT weight ratio γ enhances the measured modulus.

5.4.3 Magnetic Properties

Since pure MWNTs are diamagnetic [57, 58], those magnetized with ferromagnetic Ni are expected to exhibit a saturation magnetization M_S intermediate between the two materials [269], which is determined using SQUID magnetometry, as reported in Figure 5.6.

Magnetic nanoparticles typically exhibit superparamagnetic behavior when their sizes are smaller than a critical dimension [92]. The hysteresis data of Figure 5.6 indicates that all samples show small departures from superparamagnetic behavior, since they show a remanence $M_r < 1$ emu/g and a coercive field $H_c < 30$ Oe. This is attributed to the Ni layer thickness of 10-150 nm and length of 0.5-2 μm that are larger than the critical superparamagnetic dimension which is a few nanometers for Ni [270].

Increasing γ increases the Ni coating layer thickness with the consequence that the Ni grain size increases. Raising γ from 1 to 7 for samples SN1 and SN2, respectively, increases M_s from 4.1 to 9.5 emu/g and M_r from 0.51 to 1.01 emu/g, while H_c remains unchanged at 30 Oe. This improvement in magnetic properties, when is raised, is explained through the associated increase in the average Ni layer thickness γ from 10 to 60 nm. Although both dimensions are higher than the critical superparamagnetic dimension, they lead to single magnetic domains. Further increase in γ to 14 for sample SN3 is accompanied by an increase in the Ni layer average thickness to 100-150 nm. This larger Ni domain size increases the magnetostatic energy, which decreases when the larger domain is divided into several smaller domains. The division of the larger domain creates domain walls where adjacent molecules have net magnetic moments with different directions. These multi-magnetic domains have lower coercivity and remanence than does a single domain [87]. Therefore, the results show that the magnetic properties for SN3 are inferior to those for SN2 since M_s decreases to 6.6 emu/g while M_r and H_c are almost zero. Another observation supporting the formation of domain walls in SN3 is the presaturation region in the magnetization curve, which is a region of reversible domain wall motion. The magnetization curve of SN3 shows a higher curvature than for the other two samples. This indicates that molecules are present at domain walls, which requires higher field strength to align their magnetic moments and allow whole material saturation [87].

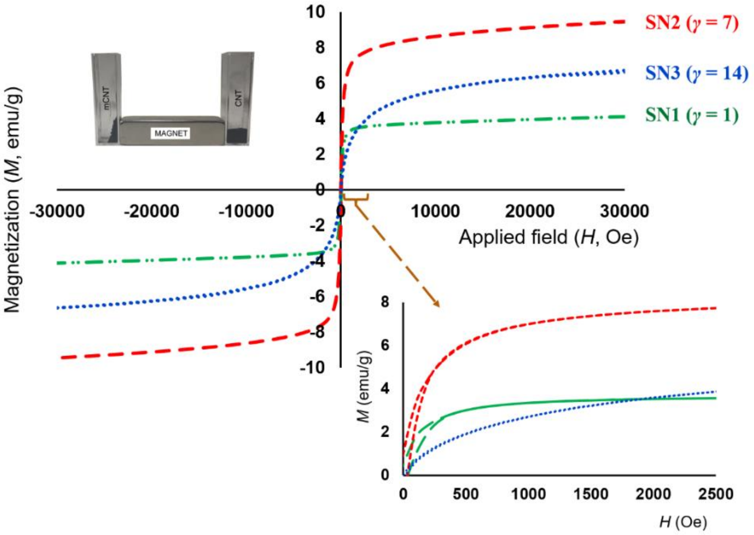

Figure 5.6: Magnetic Characterization. Magnetic hysteresis curves show that samples SN1-SN3 deviate from superparamagnetic behavior at room temperature ($M_r < 1$ emu/g and $H_c < 30$ Oe). For samples SN1 and SN2, γ increases from 1 to 7, but H_c remains constant at 30 Oe while M_s and M_r increase from 4.1 and 0.51 emu/g to 9.5 and 1.01 emu/g. For SN3, corresponding to $\gamma = 14$, single magnetic domains are transformed into multimagnetic domains since the nickel coating thickness increases to 100-150 nm.

Therefore, changes in magnetic behavior are attributed to the magnetic domains within the Ni coating. As the thickness of the coating increases from SN1 to SN2, the domain size increases while the number of magnetic domains does not change so that magnetization rises. However, the Ni thickness for SN3 is even larger. Consequently, more magnetic domains are created, which deviate its behavior from superparamagnetism, leading to a significant decline in their magnetization.

5.4.4 Tuning the NiCH Macrostructure Morphology

In the presence of an external magnetic field, NiCH (γ=1) nanostructures configure and align along the magnetic field lines. Since further Ni growth can be initiated on the catalytic surfaces of the MWNTs, the alignment of the nanoscale NiCH structures influences the morphologies of the micro- and macroscale NiCH structures. Figure 5.7 shows Ni-MWNT macrostructures fabricated with the magnetic field in the vertical (DM1) and horizontal (DM2) directions. The DM1 macrostructure was porous while DM2 was denser and flatter. Both Ni-MWNT macrostructures could be utilized in applications such as nano- and microscale filtration (for DM1) and to print electric circuits (DM2) [265-267].

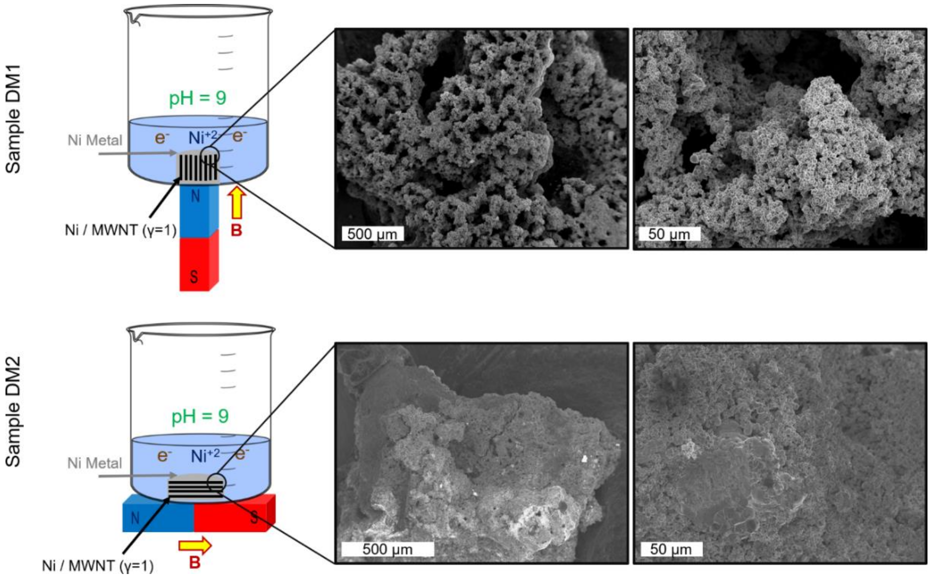

Figure 5.7: Fabrication of Nickel-MWNT Macrostructures. Nickel deposition on the vertically aligned Ni-MWNT hybrid nanomaterial (SN1, γ = 1) results in a porous 3D macrostructure (DM1). With horizontal alignment, the resulting macrostructure (DM2) is denser and flatter.

4.4.5 Conductive Inks for Circuit Printing

Figure 5.8a illustrates the preparation of water-based conductive inks, which use hydrophilic Ni-MWNTs (γ=7) as their conductive filler that is readily dispersed in water. The morphologies of lines printed with MWNT-only and Ni-MWNT based inks (2 vol%) are presented in Figure 5.8b1 and b2**,** respectively. Lines that were printed with the hydrophobic MWNT-based ink (Figure 5.8b1) contained macroscale cracks due to MWNT agglomeration after drying that destroyed their electrical continuity, producing an open circuit for DC electrical measurements. In contrast, agglomeration of hydrophilic Ni-MWNTs was far less severe and they produced a printed line (Figure 5.8b2) containing only small microscale cracks.

Figure 5.8c presents the measured electric resistivity of lines that were printed with and without magnetic assistance using inks containing different volume concentrations of Ni-MWNTs. As expected, the electric resistivity decreases with increasing Ni-MWNT concentration. When a magnet is not used to facilitate printing, the electric resistivity of the printed lines decreases from 2420 to 5.9 Ωm by increasing the volume loading of the Ni-MWNTs from 1 to 8%. The corresponding lines printed with the assistance of a magnetic showed a similar decrease from 2197 to 4.6 Ωm. Hence, magnetic assistance during printing led to a greater reduction in electrical resistivity for a lower Ni-MWNT concentration (i.e. <4 vol%) ink, where the resistivity was reduced for the 1 and 2 vol% inks by 223.8 and 313.1Ωm, respectively. Use of a magnet concentrated the relatively low Ni-MWNT content in these inks. However, magnetic assistance was less effective for inks with a higher Ni-MWNT content that also have a higher viscosity.

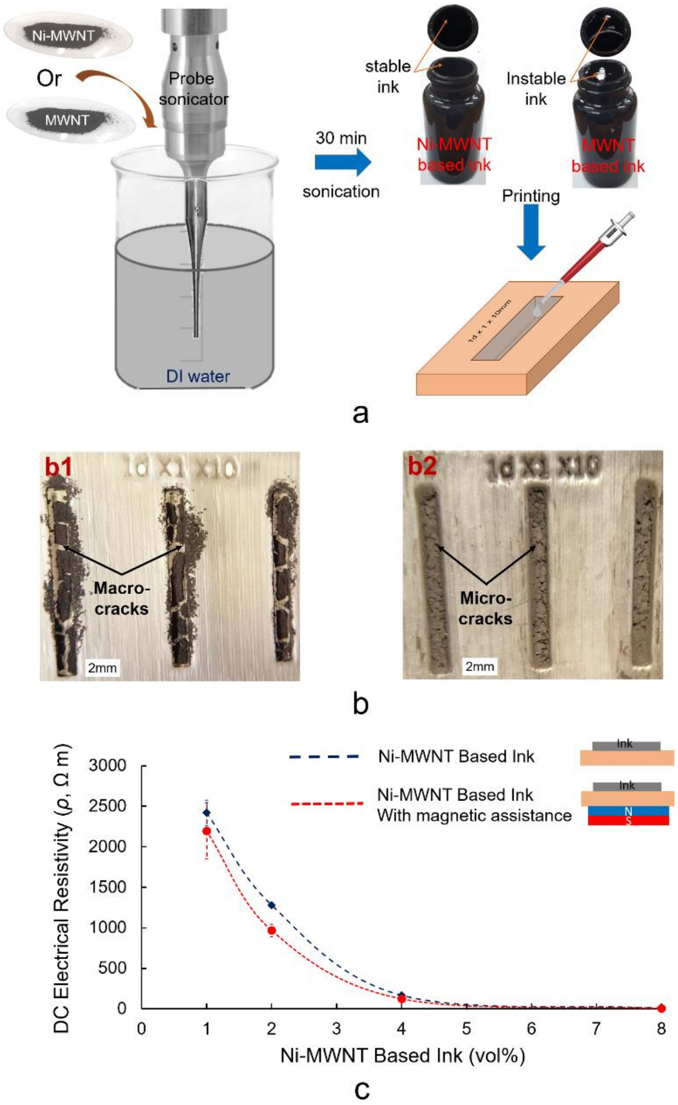

Figure 5.8: Water based conductive inks. (a) The procedure for ink preparation. Ni-MWNTs or MWNTs are dispersed in DI water using a probe sonicator and the ink poured into a plastic template. (b) Post drying, optical images show the morphology of the printed lines created by either MWNT or Ni-MWNT based inks (2 vol%). Macroscale cracks are clearly observed in the case of MWNTs, while smaller microscale cracks are observed for the other case. (c) The measured electric resistivity of the lines printed by Ni-MWNT based inks for different volume loadings with and without magnetic assistance.

These experiments provide evidence of the importance of surface modification of MWNTs during the printing of electrical circuits. Coating of MWNTs with nickel enhances their compatibility with polar solvents and polymers, and improves their mechanical and magnetic properties. Besides circuit printing, we envisage potential applications for polymeric composite materials and energy storage.

5.5 Conclusion

Nickel nanocrystals were deposited on MWNTs with electroless plating that used a chemical metal reduction method for different weight ratios $\gamma = 1, 7, 14$, and 30. Once Ni was deposited on palladium catalyst particles, it formed nanoclusters on the MWNT surfaces. When the Ni content was increased, neighboring nanoclusters merged to produce a continuous Ni coating layer that encapsulated the MWNT. For larger γ, despite Ni coverage over the palladium catalyst, deposition continued through autocatalysis by the deposited nickel. All NiCH hybrid material samples contained encased MWNTs that were connected by Ni networks. Increasing γ improved metallic connections between plated MWNTs so that the sparse MWNT network for $\gamma = 1$ became denser when $\gamma = 14$ as microscale NiCH structures were produced. In these structures, Ni formed a conductive metallic matrix that contained MWNTs as the reinforcing filler material. The Ni-MWNT hybrid material with $\gamma = 1$, and 7 had higher $E \sim 18.3$ and 58.7 GPa than pure MWNTs ($E \sim 12.5$ GPa), i.e., increasing γ improved the elastic modulus. The magnetic properties of the NiCH are superior to those of the original diamagnetic MWNTs (e.g., M_s increases), and improve with increasing γ. This electroless plating method is promising for improving the mechanical and magnetic properties of MWNTs and reducing their electrical resistance.

We also fabricated Ni-MWNT macrostructures with controlled morphologies using the NiCH. Nickel deposition on the Ni-MWNT sample that was hybrid vertically-aligned with a magnetic field (SN1, $\gamma = 1$) resulted in a porous 3D macrostructure while deposition on the horizontally-aligned hybrid produced denser and flatter macrostructures. These macrostructures could be utilized for nano- and microscale filtration, as well as for printing electric circuits.

Since the hydrophilic nickel outer layer enhances Ni-MWNT dispersion, electrically conductive inks were synthetized by simply dispersing different concentrations of Ni-MWNT ($\gamma = 7$) samples in water. An ink with a low 8% volume concentration has a relatively low electrical resistivity of 5.9 Ωm. Using a magnet to print inks containing such low Ni-MWNT concentrations reduced the electric resistivity of the printed lines by 200-300Ωm.

6. Tailoring the Properties of a Ni-MWNTs Based Polymer Nanocomposite Using a Magnetic Field

6.1 Introduction

In this chapter, an experimental investigations will be presented to highlight how to tailor the properties of nanocomposites by organizing nanoparticles (Ni-MWNTs) within the polymer matrix, e.g., for potential engineering applications. These magnetized nanoparticles are introduced into an epoxy matrix at low 0.25-1% volume fractions and aligned along the direction of an applied magnetic field, which produces anisotropic bulk properties. However, nanoparticles aligned in perpendicular directions in sequential layers result in an effectively isotropic composite material. By changing this alignment, it becomes possible to tailor the properties of the resulting composite material. This chapter is reprinted from a manuscript entitled, *Tailoring the Properties of a Polymer Nanocomposite using a Magnetic Field* by **Ahmed M Abdalla**, Rakesh P. Sahu, and Ishwar K. Puri, submitted to Composites part B: Engineering for possible publication. The author of this thesis is the first author and main contributor of the above mentioned publication and has conducted all the experiments. The chapter will provide a literature review which is discussed in the background information section, followed by excerpts from the above mentioned paper.

6.2 Background Information

The properties of natural nanocomposites, such as abalone shell [271], bone, insect wings [272] and fish tails [273] are influenced by the orientation and layering of their constituent nanomaterials. Likewise, polymer nanocomposites contain nanoscale fillers, such as nanoparticles, nanosheets and nanofibers, which can be aligned and layered within their surrounding polymer matrix. When these nanomaterials are introduced into the matrix, their high surface area to volume ratio helps enhance the mechanical, thermal, electrical, optical or magnetic properties of the resulting composite material [53, 274]. For instance, the anisotropic one-dimensional structure of a carbon nanotube (CNT) and its superior mechanical, thermal and electrical properties makes it suitable for inclusion in high-performance nanocomposites.

However, it is difficult to disperse CNTs homogeneously within the matrix due to their hydrophobicity and low wettability, which restricts their use in nanocomposite applications [35]. This limitation on dispersion must be overcome to fabricate ordered nanocomposites in which the CNT-matrix interface is effectively bonded [53]. Methods to improve CNT dispersion include ultrasonication, where high intensity ultrasound waves isolate the nanotubes from agglomerated bundles by continuously collapsing them with nucleated microbubbles. The nanotubes can instead be chemically functionalized to introduce active chemical groups containing unsaturated bonds on their surfaces. These groups increase the repulsion between adjacent CNTs [98]. However, ultrasonication alone is unable to produce a homogeneous and stable dispersion while chemical functionalization using acids produces significant CNT surface destruction, thus diminishing the nanotube properties.

The alignment of CNTs along particular directions in a polymer matrix [53-55] can be accomplished by applying external electric and magnetic fields [95, 199, 220, 268], or by leveraging the fluid drag force on the nanoparticles as they are being dispersed in the uncured matrix [98, 168, 172, 173]. Since CNTs have a poor magnetic susceptibility, this necessitates the application of a relatively strong external magnetic field during alignment to produce a force that exceeds the thermal energy and viscous resistance of the uncured polymer [55, 134]. Therefore, the nanotubes must be first magnetized if realistic magnetic fields are to be employed [168, 172, 174], e.g., by wrapping polymers functionalized with iron oxide nanoparticles [172]. These nanoparticles can also be decorated with nickel, maghemite and magnetite nanoparticles and aligned under a relatively weak field [18, 174, 275]. The decorations occur through chemical methods that destroy the CNT surfaces, do not improve their hydrophobicity, or increase their electrical contact resistance [18].

Typically, the introduction of a small amount of CNTs into a polymer matrix increases its electrical and thermal conductivities at the expense of a minor density increase [54, 168]. For instance, a small 0.021 wt% introduction of CNTs improves the electrical and thermal conductivities of an insulating polymer [53]. Including 1 wt% of multiwall carbon nanotubes (MWNTs) in polyvinyl alcohol increases the elastic modulus and hardness of the resulting composite by 80% and 60%, respectively [169]. Composites with aligned CNTs exhibit higher electric [134] and thermal [171] conductivities than those that contain randomly dispersed CNTs and, as expected, this enhancement is a function of the nanomaterial weight content [134]. The percolation threshold for CNTs in a typical polymer lies within a wide 0.5-10 wt% range. The threshold is influenced by several factors, such as degree of alignment, dispersion homogeneity, polymer type and processing method [98].

Here, we demonstrate a method to readily disperse and align commercially available MWNTs in a polymer nanocomposite. The entire surface of the MWNTs is coated with a nickel layer through nondestructive electroless plating [19, 276]. The resulting Ni-MWNTs are magnetic, have far better dispersion and stability in the polymer matrix than MWNTs alone, and enhance the properties of the composite over what MWNTs can alone provide. This hybrid nanomaterial is aligned in multiple directions within the polymer matrix with a magnetic field to investigate the influence of nanoparticle anisotropy on the bulk composite properties. The fabrication method is simple, cost effective and scalable in contrast to typical laboratory methods that are limited to millimeter dimensions.

6.3 Methodology

6.3.1 Materials and Reagents

Commercially available MWNTs purchased from US Research Nanomaterials Inc. with purity > 95%, outer diameter of 20-30 nm, inner diameter of 5-10 nm, and length between 0.5-2.0 µm and true density ~2.1 g cm^{-3}, as specified by the manufacturer, are used. Other reagents include nickel (II) chloride ($NiCl_2$, 98%, Alfa Aesar), nickel (II) sulfate hexahydrate ($NiSO_4 \cdot 6H_2O$, 99%, Sigma-Aldrich), sodium hydroxide (NaOH, 97%, Caledon Laboratory Chemicals), hydrochloric acid (HCl, 36.5-38%, Caledon), stannous chloride dihydrate ($SnCl_2 \cdot 2H_2O$, 98%, Caledon), ammonium chloride (NH_4Cl, ACS grade, BDH/VWR International), sodium citrate dihydrate ($Na_3C_6H_5O_7{\cdot}2H_2O$, 99%, EMD chemicals Inc.), sodium hypophosphite monohydrate ($NaH_2PO_2{\cdot}H_2O$, lab grade, Anachemia Canada Co.), and palladium (II) chloride ($PdCl_2$, 100%, Artcraft chemicals Inc.). Epoxy Resin and hardener (West System 105, Plastic World Co.) are used to form the matrix of the polymer composite. All reagents are used as received without further purification.

6.3.2 Electroless Plating of MWNTs with Nickel

The MWNTs are plated with nickel to produce Ni-MWNTs through electroless deposition, as described in section 5.3.3 [19]. Briefly, palladium is adsorbed onto the surface of MWNTs during two treatment steps, first with stannous chloride solution and then with palladium chloride solution [19, 97, 141, 147, 263]. Then, nickel ions (Ni^{+2}) are reduced to nickel metal on the catalyzed surface through the electrons provided by the reducing agent (sodium hypophosphite, NaH_2PO_2) [19, 147, 149, 262, 263]. The MWNTs are plated with Ni for a Ni:MWNT weight ratio $\gamma = 7$. A gram of MWNTs requires a plating solution that consists of $NiCl_2$ (11.9g), $NiSO_4{\cdot}6H_2O$ (7.7g), NH_4Cl (38.5g), $Na_3C_6H_5O_7{\cdot}2H_2O$ (28g), $NaH_2PO_2{\cdot}H_2O$ (35g) and deionized water (700 ml) [19].

6.3.3 Preparation of Epoxy Nanocomposites

Epoxy nanocomposites are prepared by dispersing either MWNTs or Ni-MWNTs in epoxy resin and subsequently sonicated with a probe sonicator (Qsonica, LLC, Model: Q500 with 1/8″ micro-tip at 35% power) for 15 min. The dispersion is kept inside a desiccator under partial vacuum of -0.1 MPa for 10 min to remove bubbles introduced during the sonication stage. A curing agent with a hardener-resin volume ratio of 1:10 is subsequently added to the dispersion and stirred for a minute. The mixture is poured into a template that has inner dimensions of 6cm × 6cm × 1cm, where it is left to be cured over 24 h (see Figure 6.1).

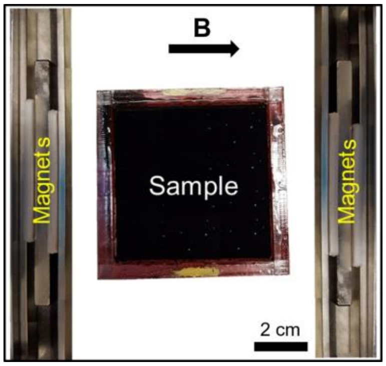

Figure 6.1: Alignment of homogeneously dispersed Ni-MWNTs in epoxy matrix using magnet sets placed on either side of a 6cm × 6cm × 1cm template containing the nanocomposite. The arrow denotes the direction of the magnetic field **B**.

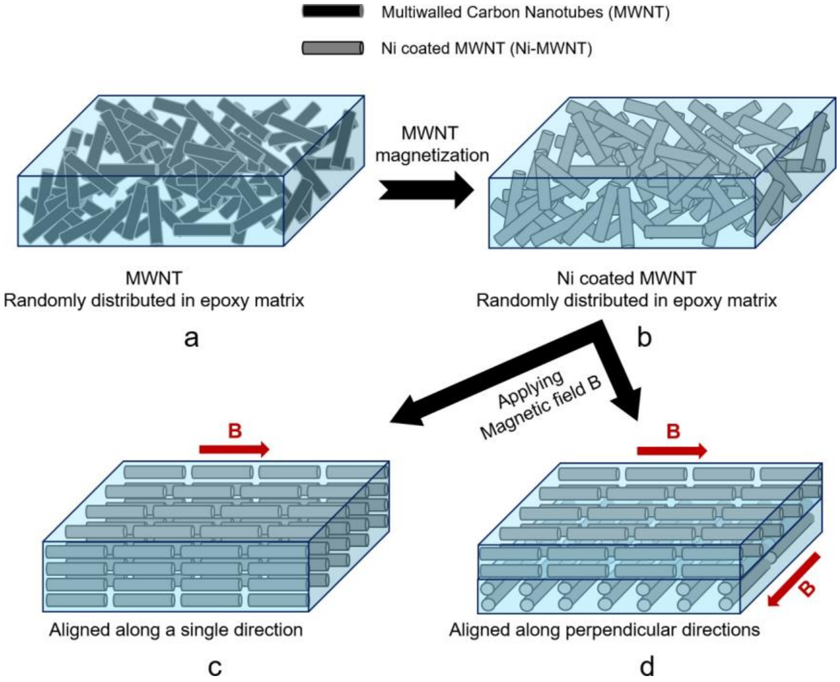

Figure 6.2: Preparation of different epoxy nanocomposites. The samples contain (a) randomly dispersed MWNTs or $MWNT_{random}$, (b) randomly dispersed Ni-MWNTs, or *Ni-*

$MWNT_{random}$ (c) Ni-MWNTs aligned along a single direction in separate layers or *Ni-$MWNT_{aligned,1D}$*, and (d) Ni-MWNTs aligned along perpendicular directions in separate layers or *Ni-$MWNT_{aligned,2D}$*.

In addition to the pure epoxy polymer sample, four other nanocomposite samples are prepared, each with a 0.25 % nanoparticle volume fraction (Figure 6.2). The equivalent weight content corresponding to this volume fraction for MWNTs is ~0.5 wt% and for Ni-MWNTs ~2 wt%. The thickness of all of these epoxy-based samples is 4 mm. The nanocomposite sample prepared with randomly dispersed MWNTs is denoted as *$MWNT_{random}$* in Figure 6.2a. The other three samples prepared with Ni-MWNTs are (i) randomly dispersed Ni-MWNTs, denoted *Ni-$MWNT_{random}$* (Figure 6.2b), (ii) Ni-MWNTs aligned along a single direction, denoted *Ni-$MWNT_{aligned,1D}$* (Figure 6.2c), and (iii) Ni-MWNTs aligned along two perpendicular directions, denoted *Ni-$MWNT_{aligned,2D}$*, as shown in Figure 6.2d.

For the latter two samples that contain aligned nanoparticles, the template is placed between two sets of NdFeB-N42 magnets (purchased from K&J Magnetics) that establish an external magnetic field to align the Ni-MWNTs through action from a distance, as shown in Figure 6.1. The liquid polymer precursor is poured two times to create sequential 2 mm thick layers, where the second 2 mm layer is poured 5 h after the first. This allows sufficient time for the first layer to become appropriately viscous and partially cured so as to hold the aligned Ni-MWNTs in place before the second layer is poured on top of it. The mid-plane of the magnet set is aligned with the nanocomposite layer. The magnets are raised by 2 mm after the first layer has partially cured. Pouring the nanocomposite into two layers allows multi-directional alignment if the magnetic field is rotated by 90° during the second pouring. Finally, 1 vol% samples are also prepared for the $Ni\text{-}MWNT_{aligned,2D}$ and $MWNT_{random}$ cases to investigate the influence of raising nanoparticle content on the sample electrical resistivity.

6.3.4 Characterization Methods

Scanning transmission electron microscopy and transmission electron microscopy (dark field STEM/TEM) are conducted with a JEOL 2010F field emission microscope. The samples are suspended in ethanol, dropped on a TEM copper grid and then wicked off with a Kimwipe. Magnetization measurements are performed at room temperature using superconducting quantum interference device **(**SQUID) magnetometry (Quantum Design Inc.). The actual magnetic field is simulated with finite element method magnetics (FEMM) software (version 8 under terms of the Aladdin free public license). Optical imaging is conducted with a VWR stereo zoom trinocular microscope. The tensile strength of the prepared polymer composite is measured with an Instron dual column testing system (Model No. 5967, 30 kN capacity, wedge action grips). Atomic force microscopy (AFM Bruker, Multimode 8 with ScanAsyst, NanoScope 9.1 software) is used to determine the elastic modulus. The AFM tip (TAP 525 A) with measured tip radius and deflection sensitivity of 5 nm and 82.6 $nm.V^{-1}$ (using the built-in Ramp mode) is calibrated with a reference material (Sapphire−12M, Bruker test sample kit) that has a known elastic modulus of 350 GPa. The natural frequency and the spring constant of the tip are calculated from thermal tuning data to be 520 Hz and 204.2 $N.m^{-1.}$ These values are in good agreement with standard values of 525 Hz and 200 N/m provided by the manufacturer. All measurements are performed using NanoScope Analysis 1.5 software. The AC electrical resistivity is measured using an ultra-precision capacitance bridge (Andeen Hagerling) at a frequency of 1 kHz. To avoid interference with surroundings, the sample is mounted inside a Pomona box, as shown in Figure 6.3.

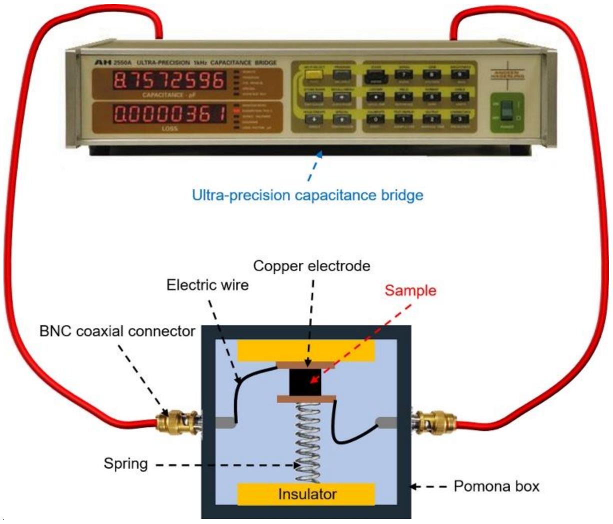

Figure 6.3: Schematic of AC electrical resistivity measurements using an ultra-precision capacitance bridge at 1 kHz.

6.4 Results and Discussion

6.4.1 Nickel-Coated MWNTs

We have presented detailed phase and morphology analyses of Ni-MWNTs in section 5.4.1 [19]. Figure 6.4a presents a TEM image of as prepared MWNTs. The dark-field STEM image presented in Figure 6.4b confirms complete coating of nickel over MWNTs. The thickness of the Ni coating is measured to be ≈40-60 nm. Pure MWNTs are diamagnetic [57, 58] but coating them with a ferromagnetic Ni layer results in a hybrid nanomaterial that exhibits superparamagnetic behavior. Therefore, the synthesized Ni-MWNTs exhibit improved response toward the magnets (Figure 6.4c). The magnetic hysteresis loop confirms the magnetic saturation of the Ni-MWNTs whereas pure MWNTs are nonmagnetic. The magnetic saturation of the Ni-MWNT is determined to be 9.5 emu g^{-1} using SQUID magnetometry, as shown in Figure 6.4d. The improved magnetization of Ni-MWNTs allows the material to align readily along the direction of an external magnetic field.

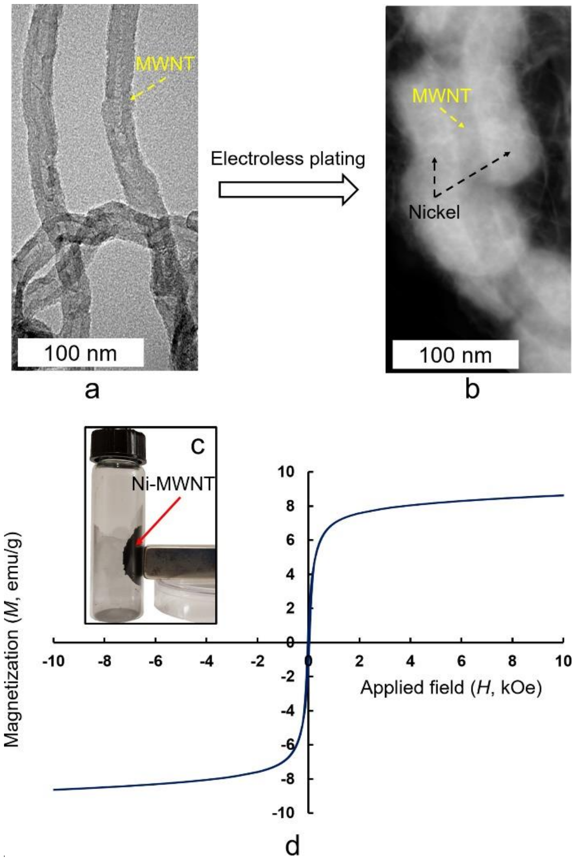

Figure 6.4: Phase and morphology of the synthesized Ni-MWNT samples. (a) TEM image of the as prepared MWNTs, (b) dark field STEM image of an Ni-MWNT, (c) magnetic response of the prepared Ni-MWNTs towards a magnet, and (d) the magnetic hysteresis curve that shows that Ni-MWNTs exhibit quasi-superparamagnetic behavior at room temperature ($M_s \sim 9.5$ emu g^{-1}).

6.4.2 Alignment of Ni-MWNT in the Epoxy Matrix

A magnetic field with a relatively low ~0.1 T strength is used to align the Ni-MWNTs within the epoxy. In Figure 6.5a, two-dimensional simulations of the experiments using FEMM software show the magnetic lines of force and field magnitudes generated during the experiment. There is a slight variation in field strength along *x* and *y* axes of the sample domain, from 0.098-0.103 T and 0.103-0.107 T, respectively (Figure 6.5b & 6.5c). This quasi-uniform **B** field effectively aligns Ni-MWNTs along a single direction.

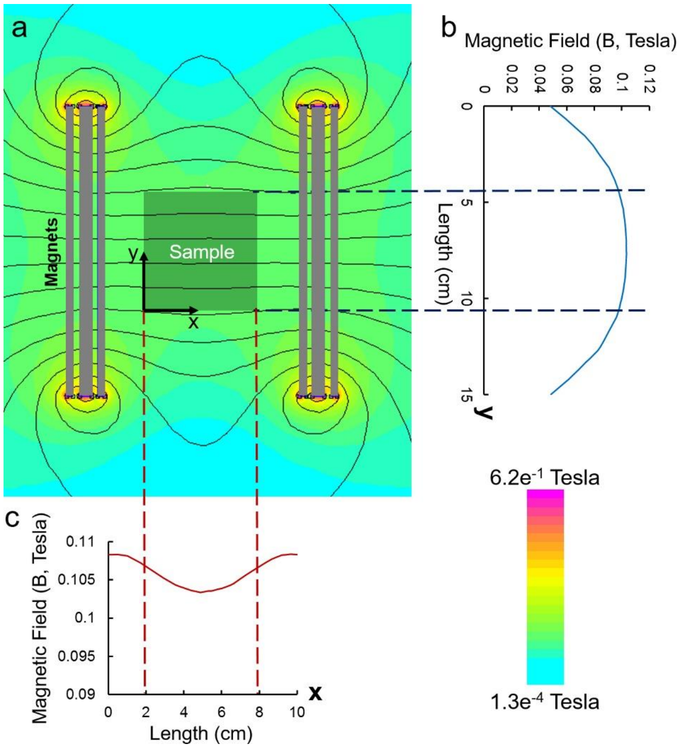

Figure 6.5: Simulated characteristics of the magnetic field within the sample. (a) A 2-D simulation showing the topology of the magnetic lines of force and the field magnitude within the sample along its (b) *x* and (c) *y* axes. The simulation is conducted with the dimensions of the experimental setup and the magnet type and size employed.

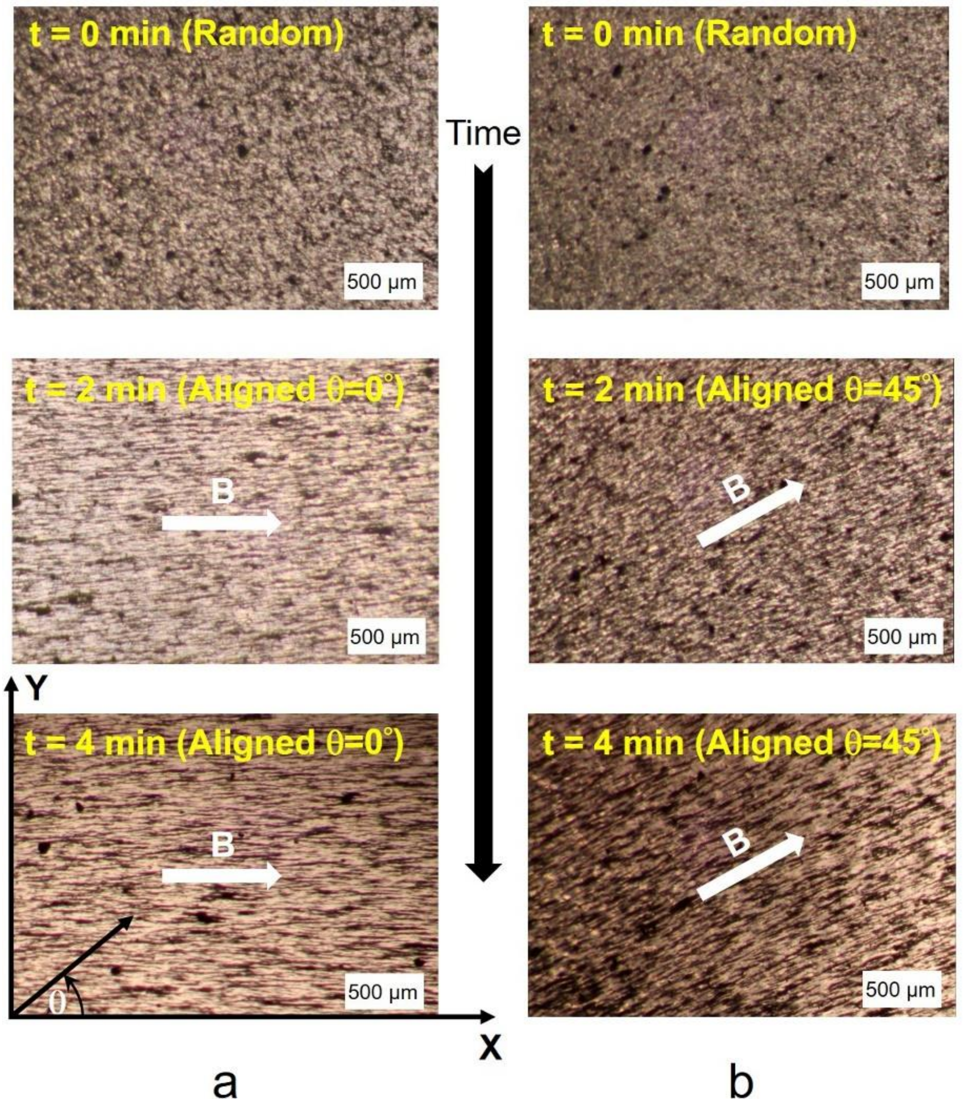

Figure 6.6: Optical microscope images obtained at different times confirm Ni-MWNT nanoparticle agglomeration into clusters that finally the align after 4 min along the direction of the applied magnetic field oriented at (a) 0° and (b) 45° with respect to an arbitrary axis.

The alignment of Ni-MWNTs under the influence of the external magnetic field is visualized under an optical microscope for a very low nanoparticle volume fraction (0.01%) in the epoxy matrix. We observe that Ni-MWNT clusters align along the direction of the imposed magnetic field. Visualizations are for ~ 0.1 T magnetic field orientations of 0° and

45° with respect to an arbitrary axis, as shown in Figure 6.6a and 6.6b, respectively**.** Figure 6.6 shows the different stages of alignment at three different times, namely, 0, 2 and 4 min after the application of the magnetic field. During alignment, Ni-MWNTs first agglomerate into microscale clusters that orient along the magnetic field direction but, after ~4 minutes, these clusters become fully aligned along this direction.

6.4.3 Tensile Strength of the Nanocomposites

Tensile tests are conducted at room temperature and humidity with a cross-head speed of 0.1 mm.min^{-1}. For each tensile strength experiment, four identical samples are prepared. The samples are polished with an emery cloth to ensure that the Instron sample holder can properly grip them. Sample stretching continues until complete failure occurs. The maximum stress on a sample is used to calculate its ultimate tensile strength (referred to as tensile strength hereafter).

The tensile strengths for five cases with the same 0.25 % nanoparticle volumetric fraction are presented in Figure 6.7. This strength decreases by ~26.5% from 43.4 MPa for pure epoxy to 31.9 MPa when 0.25 vol% of pure MWNTs are added to the matrix. The MWNTs have a non-polar surface that is incompatible with the epoxy matrix, which leads to their weak adhesion with polymer chains [53]. The multiwall nanotubes also disperse poorly, agglomerating into microsize bundles [98], which initiate microscale cracks inside the cured epoxy that diminish its tensile strength. The tests for the $MWNT_{random}$ samples therefore have a relatively large standard deviation of ~6.6 MPa, which is attributed to their poor nonuniform dispersion in epoxy. Depositing a nickel layer over the non-polar carbon surface significantly improves MWNT dispersion in the matrix. Consequently, *Ni-MWNT$_{random}$* samples have a higher mean tensile strength of ~41.6 MPa. While this strength is slightly lower than that of pure epoxy by ~4.1%, it also shows a large standard deviation of ~6.7 MPa, which we again attribute to nonuniform nanoparticle agglomeration.

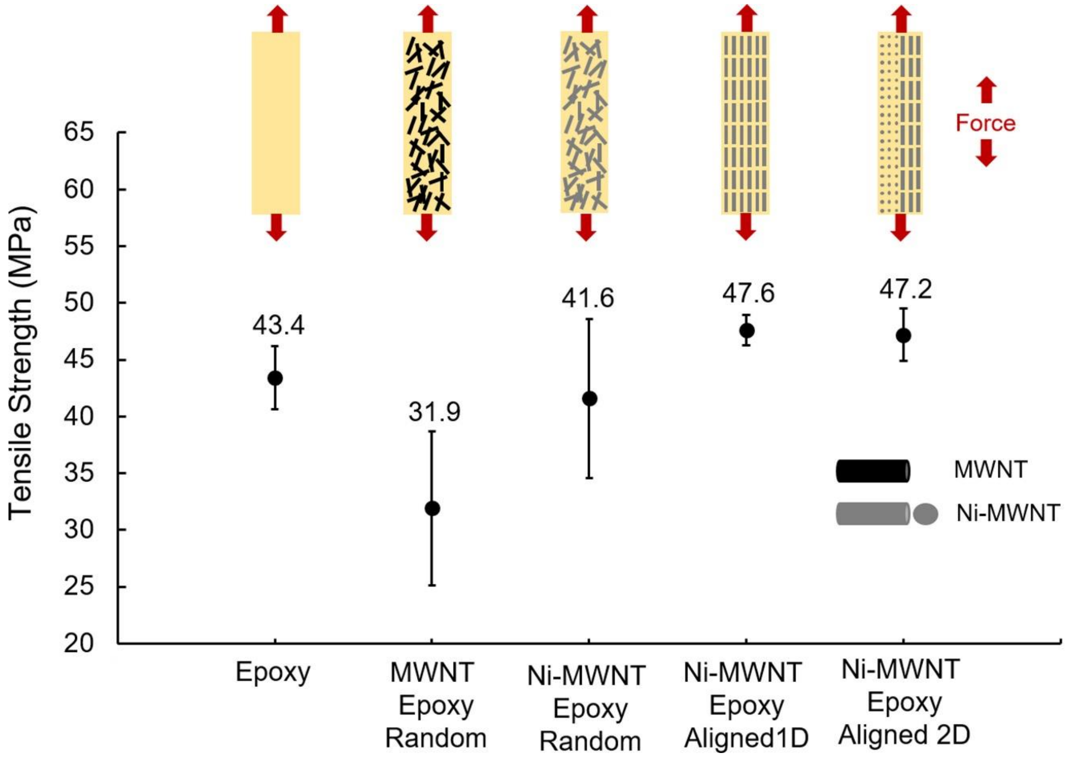

Figure 6.7: Tensile strengths for different epoxy nanocomposites. The nanoparticle volume fraction for all nanocomposites is 0.25%. The organization of the nanoparticles within the epoxy matrix is also illustrated.

Aligning Ni-MWNTs along specific field directions during curing produces anisotropic organization and improves directional dispersion. Both *Ni-MWNT$_{aligned,1D}$* and *Ni-MWNT$_{aligned,2D}$* tensile strength tests therefore have much lower standard deviations of ~1.8 MPa, and 2.3 MPa, respectively, than do the random samples. These aligned samples reveal a slight increase in the average tensile strength to ~47.6, and 47.2 MPa, respectively, both values being close to the upper standard deviation limit for the $Ni\text{-}MWNT_{random}$ sample. The effect of Ni-MWNT alignment coupled with better directional dispersion improves the load bearing capability of the nanocomposite. These results clarify that nanoparticle organization can be used to tailor the mechanical properties of a nanocomposite [96, 241].

6.4.4 Elastic Modulus E

The mean elastic modulus E of the samples is measured using AFM with the same tip and under similar AFM calibration conditions so that the resulting values are relative to the elastic modulus (E = 350 GPa) of a standard sapphire sample. In the case of samples containing aligned Ni-MWNTs, probing with the AFM tip is conducted perpendicular to the direction of alignment.

An epoxy sample and three nanocomposite samples, namely, $MWNT_{random}$, $Ni\text{-}MWNT_{random}$, and $Ni\text{-}MWNT_{aligned,1D}$, are probed. Since probing with the AFM tip provides a surface property, it is not possible to investigate the effect of alignment in perpendicular directions on the elastic modulus of the $Ni\text{-}MWNT_{aligned,2D}$ sample. The AFM is also less suitable for investigating the effect of alignment because the scanning area is limited to a few μm^2. Probing a larger area with a lower scan rate would be more accurate but this requires several hours of probing which deteriorates the AFM tip with the result that the same tip cannot be used to probe all samples. The nanocomposite samples are polished with emery cloth prior to the AFM measurements. The surface roughness of all samples is within 1.5-2 μm, as shown in Figure 6.8a.

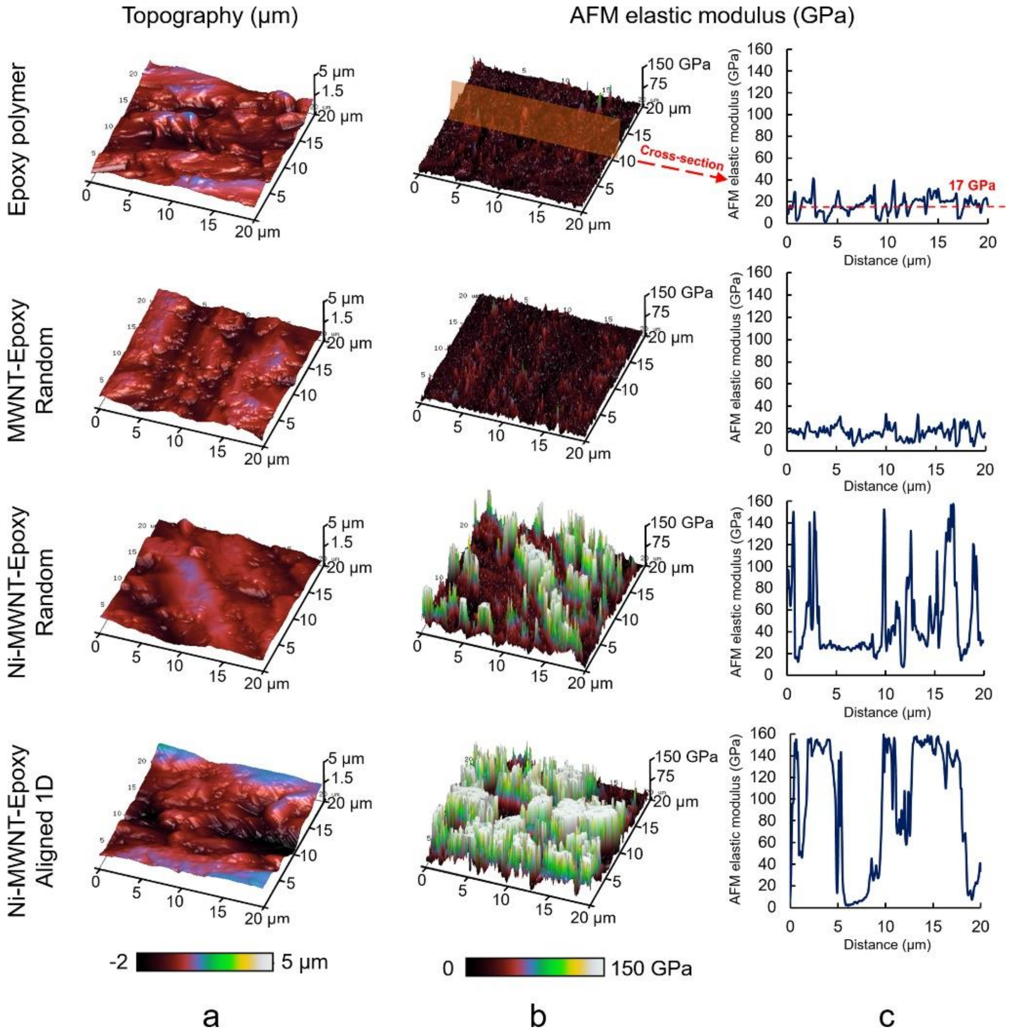

Figure 6.8: AFM characterization of the cured polymer and its three nanocomposites, *$MWNT_{random}$*, *$Ni\text{-}MWNT_{random}$*, and *$Ni\text{-}MWNT_{aligned,1D}$*. (a) Surface topography, (b) elastic modulus and (c) line scans of the elastic modulus. The nanocomposites are prepared with a 0.25 vol% nanoparticle loading. While epoxy has an average elastic modulus E ~ 17 GPa, which is similar to that for the *$MWNT_{random}$* sample, both Ni-MWNT composites reveal higher E up to ~ 150 GPa.

We have previously reported that, for γ=7, Ni-MWNTs have a ~5 times higher average elastic modulus than pure MWNTs (~ 12.5 GPa) [19]. As shown in Figure 6.8, similar behaviour is observed for these two types of nanoparticles when they are dispersed in epoxy. AFM measurements over a 20 μm^2 cross-section of the nanocomposite samples are presented in Figure 6.8b. The average elastic modulus E of pure epoxy composite is measured to be 17 GPa (Figure 6.8c), which is slightly higher than for the as-prepared commercially purchased MWNTs. This explains why E for the $MWNT_{random}$ sample is similar to that for the pure epoxy sample. The $Ni\text{-}MWNT_{random}$ sample containing the same volume fraction of Ni-MWNT nanoparticles has a significantly higher E (Figure 6.8c). At certain locations, E reaches a maximum value of 150 GPa for both the $Ni\text{-}MWNT_{random}$ and $Ni\text{-}MWNT_{aligned,1D}$ samples, but a typical E value across a line scan fluctuates between 60-100 GPa. The density of hot spots characterized by local E peaks increases when Ni-MWNTs are aligned, as shown in Figure 6.8c. This result is in agreement with the optical images in Figure 6.6 where Ni-MWNT agglomeration is observed to organize into local clusters aligned with the applied magnetic field.

6.4.5 AC Electrical Resistivity ρ

The electrical resistivity ρ of the pure epoxy and the nanocomposite samples, all with the same nanoparticle loading, are presented in Figure 6.9a. The 1×1×0.4 cm samples are placed between two copper electrodes and measurements made under an AC current of frequency of 1 kHz. A thin layer of silver paste is applied to both edges of the sample, which is then placed between spring loaded electrode contacts. The $Ni\text{-}MWNT_{aligned,1D}$ sample contains two 2 mm thick layers in which Ni-MWNTs are aligned along one direction. Hence, two separate measurements are conducted, one along the direction of alignment and another perpendicular to it. The $Ni\text{-}MWNT_{aligned,2D}$ sample contains sequential 2 mm layers in which the nanoparticles are aligned along perpendicular directions in the two layers. The measurements are similar across different sides of this sample because, during each experiment, although the second layer contains Ni-MWNTs aligned along the perpendicular direction, one of the layers contains Ni-MWNTs aligned along the measurement direction. Six measurements are made for each case. The mean ρ and its standard deviation are presented in Figure 6.9.

Pure epoxy with a mean ρ = 329.3 MΩ m (Figure 6.9a) behaves as an insulator. When 0.25 vol% of Ni-MWNTs are randomly dispersed within epoxy, ρ decreases by 28.3% to 236 MΩ m. The alignment of Ni-MWNTs in a single direction induces anisotropic bulk behaviour in the $Ni\text{-}MWNT_{aligned,1D}$ nanocomposite. The resistivity reduces significantly along the anisotropic alignment direction to 188.1 MΩ m, while ρ = 237.4 MΩ m in the perpendicular direction, i.e., across the nanotubes. This latter resistivity is similar to that for the sample containing randomly distributed Ni-MWNTs. While ρ decreases by 28.3% when Ni-MWNTs are randomly dispersed in pure epoxy, nanoparticle alignment decreases the resistivity by 42.9% from that of pure epoxy.

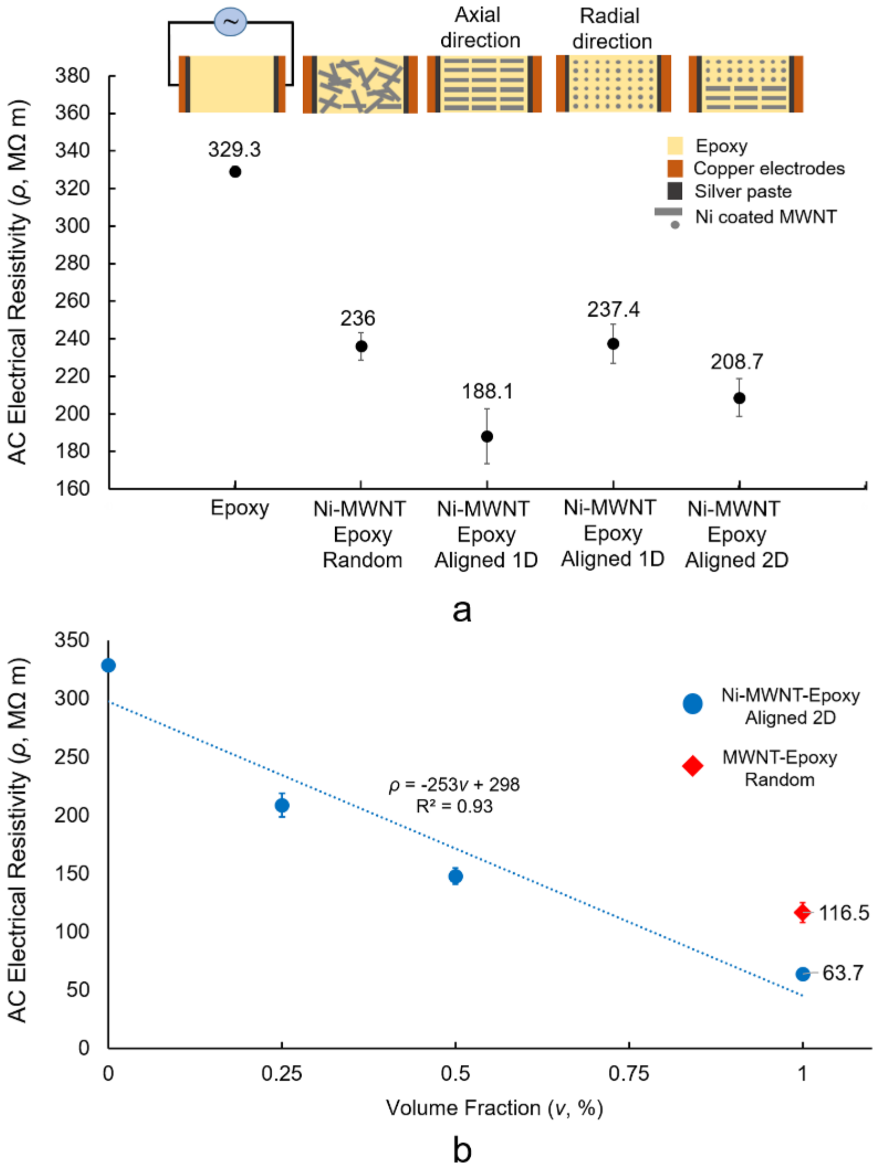

Figure 6.9: AC electrical resistivity ρ measured at a frequency of 1 kHz. (a) Effect of nickel coating and alignment on the resistivity of nanocomposites prepared with the same 0.25% volumetric nanoparticle loading along with pictorial representations of how the nanoparticles are organized within the epoxy matrix. (b) Change in resistivity with volumetric loading for the $Ni\text{-}MWNT_{aligned,2D}$ composite. A nanocomposite prepared with randomly distributed MWNTs at a 1% volume loading is used as reference sample for comparison.

The alignment of Ni-MWNT along perpendicular directions in the two adjacent layers in the $Ni\text{-}MWNT_{aligned,2D}$ sample produces a higher value for ρ than of the $Ni\text{-}MWNT_{aligned,1D}$ sample measured along the alignment direction. This is to be expected since the Ni-MWNT volume fraction that is aligned along the direction of measurement is now halved in comparison to the fraction contained in the entire $Ni\text{-}MWNT_{aligned,1D}$ sample. With nanoparticles in only one of the two layers aligned along the measurement direction, the decrease in ρ (~36.6%) is higher than that induced by the randomly organized $Ni\text{-}MWNT_{random}$ sample and along the radial direction of the $Ni\text{-}MWNT_{aligned,1D}$ sample . Thus, perpendicular alignment of Ni-MWNTs in the two adjacent layers of the $Ni\text{-}MWNT_{aligned,2D}$ sample appears to produce an overall isotropic material. These results show how Ni-MWNT alignment can be varied to tailor the degree of anisotropy in a bulk composite material.

We examine the influence of volume fraction on ρ in light of the equivalent isotropic behaviour of the $Ni\text{-}MWNT_{aligned,2D}$ composite in Figure 6.9 where the Ni-MWNT fraction is varied between 0 (pure epoxy) to 1 vol%. As expected, ρ decreases with increasing Ni-MWNT fraction. A minimum 63.7 MΩ m value measured at the 1 vol% loading, representing an 80.7% reduction in ρ over pure epoxy. When the matrix is loaded with the same 1 vol% of as prepared randomly distributed MWNTs, ρ = 116.5 MΩ m, which is a ~64.6% reduction over the pure epoxy value. For the two-layer case with differently aligned Ni-MWNTs, a single layer conducts electricity far more effectively since nanoparticles in the other layer lie orthogonal to the measurement direction. At the same 1 vol%, loading, the electrical resistivity of the quasi-isotropic $Ni\text{-}MWNT_{aligned,2D}$ sample is roughly half that of its $MWNT_{random}$ counterpart, revealing how ρ is reduced by coating MWNTs with nickel to reduce the matrix-nanoparticle interfacial contact resistance.

6.5 Conclusion

Electroless metal plating of commercially available MWNTs is a simple, direct, inexpensive and scalable method to improve the mechanical and electrical properties of a nanocomposite. Since the resulting Ni-MWNTs are magnetic nanoparticles, an external magnetic field can be applied in the form of action from a distance to align these nanoparticles within a nanocomposite. This alignment enhances the properties of the composite, such as its tensile strength, elastic modulus and AC electrical resistivity. Deposition of nickel over MWNT also improves the interfacial bonding between the resulting Ni-MWNT hybrid nanoparticles and the surrounding polymer matrix. The tensile strength of a nanocomposite containing 0.25% volume fraction of aligned Ni-MWNTs is ~9% higher than of pure epoxy and ~47% higher than a composite containing a similar volume fraction of randomly dispersed nanoparticles. Nanoparticle alignment reduces the variability in tensile strength measurements since the dispersion homogeneity in different samples is improved along the direction of the magnetic field. With a 0.25 vol% of aligned Ni-MWNTs, the AC electric resistivity along the alignment direction is ~40% lower than of pure epoxy and ~20% lower than of the composite containing a similar fraction of randomly dispersed nanoparticles. We demonstrate for the first time how anisotropic nanoparticles can be aligned in multiple directions in a polymer matrix to produce an effectively isotropic nanocomposite. The AC electrical resistivity of an epoxy nanocomposite fabricated with 0.25 vol% Ni-MWNTs aligned in perpendicular directions in two sequential layers is effectively isotropic and ~11.6% lower than for the composite containing a similar fraction of randomly dispersed Ni-MWNTs. Therefore, aligning Ni-MWNTs along multiple directions enables the tailoring of the physical properties of their epoxy composites, as well as their direction-dependent bulk behaviour, which is potentially useful for many engineering solutions, e.g., potential aerospace, automobile and infrastructure applications.

7. Supercapacitor Based on Nickel Oxide Nanotubes Synthesised From Ni-MWNT Hybrid Nanomaterials

7.1 Introduction

In this chapter, an experimental investigations will be presented to highlight a novel approach for the fabrication of nickel oxide nanotubes based on multiwalled carbon nanotubes as a sacrificial template. Electroless deposition is employed to deposit nickel on carbon nanotubes. Subsequent annealing of the product in the presence of air oxidizes nickel to nickel oxide whereas carbon is released as gaseous carbon dioxide, leaving behind nickel oxide nanotubes. New chelating polyelectrolytes are used as dispersing agents to achieve high colloidal stability both for nickel coated carbon nanotubes and nickel oxide nanotubes. An electrode for supercapacitor was fabricated using nickel oxide nanotubes as the active element and nickel coated carbon nanotubes as a conductive filler. This chapter is reprinted from Nanotechnology, *Nickel Oxide Nanotubes Synthesis using Multiwalled Carbon Nanotubes as Sacrificial Templates for Supercapacitor Application*, 28 (7), **Ahmed M Abdalla**, Rakesh P. Sahu, Cameron J. Wallar, Ri Chen, Igor Zhitomirsky, and Ishwar K. Puri, with permissions from IOP. The chapter will provide a literature review which is discussed in the background information section, followed by excerpts from the above mentioned paper. The author of this thesis is the first author and main contributor of the above mentioned publication and has conducted all the experiments except the electrochemical characterization section.

7.2 Background Information

Carbon neutral solutions require not only renewable energy generation but also efficient energy storage devices. Novel synthesis processes that produce novel active materials for these devices will improve their affordability and performance. Quasi one-dimensional (1D) nanostructures, such as nanoparticles, nanotubes and nanowires, have intrinsically large surface area to volume (hence mass) ratios, short diffusion lengths for charge and mass transport, and substantial volume change capacities, which makes them suitable for next generation energy storage devices [277]. Many nanostructures also exhibit superior electrochemical performance [278, 279].

Pseudocapacitors are a class of supercapacitors that store Faradaic current through charge transfer between an electrode and an electrolyte [280, 281]. Conducting polymers and transition metal oxides, such as ruthenium oxide (RuO_2), iridium oxide (IrO_2), manganese dioxide (MnO_2), bismuth oxide (Bi_2O_3), cobalt oxide (Co_3O_4), iron oxide (Fe_3O_4), and nickel oxide (NiO), are candidate electrode materials for pseudocapacitors,[282] although fabrication cost is an issue. Among transition metal oxides with p-type semiconducting properties, NiO exhibits higher theoretical capacitance, charge density, and chemical stability [283-287]. The gravimetric specific capacitance of metal oxide based electrodes decreases with increasing electrode mass [282, 288-291]. The charge in pseudocapacitors is stored mostly on the surface of the active material, reducing the active mass, which is favorable for electrochemical performance [292, 293] and thus decreasing the specific capacitance [278, 283, 294, 295]. Supercapacitor electrodes containing active materials and conductive additives also benefit from tubular and fibrous microstructures [295-297] that enhance charge transfer and electrolyte access to the active material, and reduce the amount of binder that is introduced.

Due to their small crystal size, high aspect ratio and hollow microstructure, nickel oxide nanotubes (NiONT) show promise for sensing [285, 298], catalysis [299], energy storage applications such as batteries [284, 300-302] and supercapacitors [303, 304]. The performance of NiO-based supercapacitors [282, 288, 305-307] is enhanced by fabricating electrodes that have high NiO mass loadings. Practical applications require high specific capacitance for a mass loading of 10-20 mg cm^{-2} [308]. Hence, NiO and other charge storage materials are typically combined with conductive additives, such as Ni, multiwalled carbon nanotubes (MWNT) and graphene to fabricate composite electrodes that show improved electronic conductivity [288, 289, 295].

Since NiONT applications are limited by the lack of simple and low cost fabrication methods, we propose a new scalable method to overcome this limitation. We encapsulate MWNTs with Ni by depositing the metal through electroless deposition to synthesize the Ni-MWNT hybrid material (the process was detailed in chapter 5) [19, 140, 141, 144, 147, 262]. These encapsulated nanotubes are annealed in air at temperatures much lower than the melting temperature of Ni so that the metal and carbon in MWNTs oxidizes to NiO and CO_2. Release of the gaseous carbon dioxide results in a tubular vacancy where the MWNT existed previously. Thus, the residual NiO retains the shape of the (now oxidized) underlying MWNT template, producing a NiONT. The wall thickness of this nanotube may be controlled by varying the mass of Ni deposited, which could allow control over the dimensions of the synthesized NiONTs. We investigate NiONT charge storage by using these nanotubes in the electrode of an electrochemical supercapacitor.

7.3 Methodology

7.3.1 Materials and Reagents

Commercially available MWNTs purchased from US Research Nanomaterials Inc. with purity > 95%, outer diameter of 20-30 nm, inner diameter of 5-10 nm, and length between 0.5-2.0 µm as specified by the manufacturer are used. Other reagents included nickel (II) chloride ($NiCl_2$, 98%, Alfa Aesar), nickel (II) sulfate hexahydrate ($NiSO_4 \cdot 6H_2O$, 99%, Sigma-Aldrich), sodium hydroxide (NaOH, 97%, Caledon Laboratory Chemicals), hydrochloric acid (HCl, 36.5-38%, Caledon), stannous chloride dihydrate ($SnCl_2 \cdot 2H_2O$, 98%, Caledon), ammonium chloride (NH_4Cl, ACS grade, BDH/VWR International), sodium citrate dihydrate ($Na_3C_6H_5O_7 \cdot 2H_2O$, 99%, EMD chemicals Inc.), sodium hypophosphite monohydrate ($NaH_2PO_2 \cdot H_2O$, lab grade, Anachemia Canada Co.), and palladium (II) chloride ($PdCl_2$, 100%, Artcraft chemicals Inc.). Poly(4-styrenesulfonic acid-co-maleic acid) sodium salt (PSSA, M_w=20 kDa), Poly[1-[4-(3-carboxy-4-hydroxyphenylazo)benzenesulfonamido]-1,2-ethanediyl, sodium salt] (PAZO, M_w=65-100 kDa) and Poly(vinyl butyral-co-vinyl alcohol-co-vinyl acetate) (PVB, M_w=50–80 kDa) were obtained from Sigma Aldrich. Ni foams with a porosity of 95% were supplied by Vale Company. All reagents were used as received without further purification.

7.3.2 Synthesis of Nickel Oxide Nanotube (NiONT)

The synthesis of the nickel oxide nanotubes is schematically illustrated in Figure 7.1a. Initially, MWNTs were sensitized with stannous chloride solution and then catalyzed with palladium through treatment with palladium chloride solution [19, 97, 141, 147, 263], in both cases under ultra-sonication with a probe sonicator (Qsonica, LLC, Model: Q500 with 1/4″ micro-tip at 35% power) for 30 min. The catalyzed MWNTs were washed with water and dried in vacuum oven after each treatment step. The catalyzed MWNTs were electrolessly plated with nickel nanocrystals through the chemical reduction of Ni^{+2} contained in the plating solution by electrons provided by sodium hypophosphite (NaH_2PO_2), which acted as a reducing agent. Since the reaction was constrained to the catalytic surfaces of the MWNTs, a continuous nickel layer was deposited that encapsulated the entire MWNT [19, 147, 149, 262]. The autocatalytic Ni surface continued to facilitate nickel deposition even after the original MWNT surface was completely encapsulated [263]. The details of the catalyzing process of MWNT are presented in section 5.3.2.

The Ni layer thickness was changed by varying the Ni:MWNT weight ratio (γ = 1 and 7), see section 5.3.3. As a summery, for each gram of MWNTs desired, a plating solution was prepared [19]. For two particular experiments, the solution consisted of $NiCl_2$ (1.7g), $NiSO_4 \cdot 6H_2O$ (1.1g), NH_4Cl (5.5g), $Na_3C_6H_5O_7 \cdot 2H_2O$ (4g), $NaH_2PO_2 \cdot H_2O$ (5g) and DI water (100 ml) for γ = 1, and $NiCl_2$ (11.9g), $NiSO_4 \cdot 6H_2O$ (7.7g), NH_4Cl (38.5g), $Na_3C_6H_5O_7 \cdot 2H_2O$ (28g), $NaH_2PO_2 \cdot H_2O$ (35g) and DI water (700 ml) for γ = 7. The electroless deposition of Ni over MWCNT was conducted at pH ~ 9-10. Sodium hydroxide solution (2N) was added dropwise to maintain the reaction pH, which was monitored with a pH meter at 5 min intervals and a probe sonicator simultaneously used to continuously sonicate the medium for 60 min. The reaction products were immediately washed and dried to obtain Ni-MWNTs.

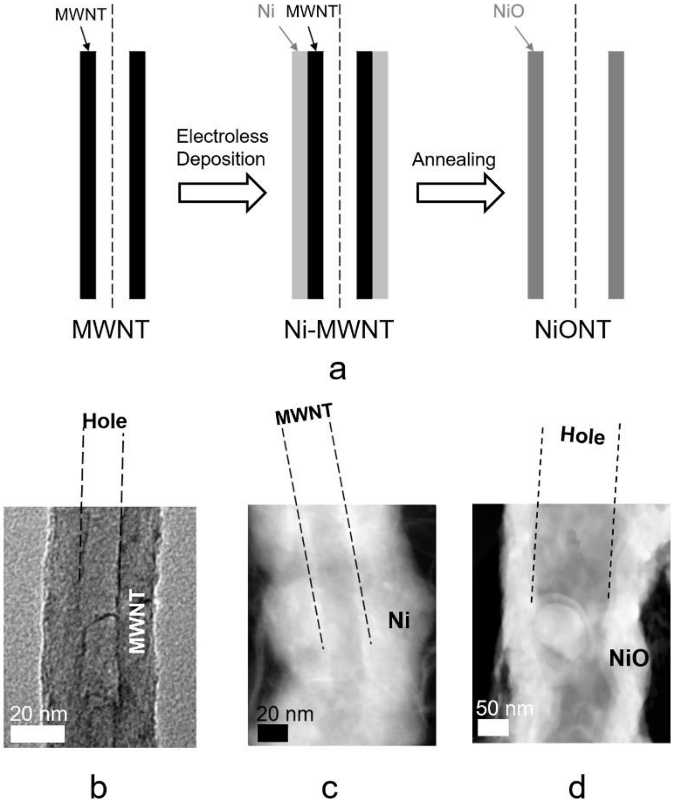

Figure 7.1: Synthesis of nickel-oxide nanotubes. (a) Schematic of the synthesis process for nickel oxide nanotubes (NiONTs). It involves the electroless deposition of Ni on MWNT, oxidation of Ni to NiO, and carbon of the MWNT to gaseous CO_2. The carbon dioxide is released, producing a tubular vacancy in the NiO bulk where the MWNT originally existed. (b) TEM image of a MWNT, (c) dark field STEM image of a Ni-MWNT, and (d) dark field STEM image of a NiONT.

The two Ni-MWNT samples for $\gamma = 1, 7$ were annealed at ≈500 °C for 2 hours in the presence of air to oxidize Ni to NiO and the MWNT carbon content to CO_2. Release of the carbon dioxide left a tubular vacancy inside the NiO bulk, leading to the formation of NiONTs. The resulting nanotube samples are labeled NiONT-1 for $\gamma = 1$ and NiONT-2 for $\gamma = 7$.

7.3.3 Preparation of Colloidal Suspension of Ni-MWNT and NiONT

Electrode fabrication for testing electrochemical performance requires a very stable colloidal suspension of the active material. The prepared NiONT serves as the active material and the Ni-MWNT as a conductive additive to achieve high specific capacitance at high active mass loadings by dispersing and mixing these components.

Dynamic Light Scattering (DLS, DelsaMax Pro: Beckman Coulter) was used to measure the effect of two different dispersing agents, i.e., PAZO and PSSA, on the colloidal stability of Ni-MWNTs and NiONTs. Dispersions in PAZO were prepared by dissolving 1 g L^{-1} of the substance in a 75% ethanol solution, followed by dispersing 4 g L^{-1} of the solid material using the probe sonicator for 30 min. Dispersions in PSSA were prepared by dissolving 1 g L^{-1} of the compound in a 60% ethanol solution, again followed by dispersing of 4 g L^{-1} of the solid material and using the probe sonicator for 30 min. Both solutions were diluted further to make stability measurements using DLS.

7.3.4 Characterization Methods

X-Ray Diffraction (XRD) analysis of samples was performed using a Bruker D8 Discover instrument comprising a Davinci^{TM} diffractometer operating at 35 kV and 45 mA using Co-K_α radiation (λ_{avg} = 1.79026 Å). Bruker's DIFFRAC.Eva V3.1 software was used for qualitative analysis of the constituent phases. Scanning transmission and transmission electron microscopy (dark field STEM/TEM) and energy dispersive X-ray (EDX) spectroscopy were conducted with a JEOL 2010F field emission microscope. For STEM/TEM, the samples were suspended in ethanol, dropped onto a TEM copper grid, and then wicked off with a Kimwipe.

7.3.5 Electrochemical Performance Testing

Electrochemical characterization of the fabricated electrode was carried out using a standard three-electrode system using a potentiostat (PARSTAT 2273, Princeton Applied Research). The surface area of the working electrode was 1 cm^2. The counter electrode was a platinum gauze, and the reference electrode was a standard calomel electrode (SCE). The characterization was conducted in 1 M KOH aqueous solutions using (i) cyclic voltammetry (CV) and (ii) electrochemical impedance spectroscopy (EIS).

The CV measurements were performed within a 0–0.5 V potential range versus the SCE as a reference electrode, and data recorded by PowerSuite electrochemical software. The CVs were obtained at scan rates of 2-100 mV s^{-1}. The charge Q was calculated based on half of the integrated area of the CV curve. The integrated capacitance $C_S=Q/\Delta VS$ was determined by dividing Q by the width of the potential window ΔV and the electrode area S. Alternating current measurements of complex impedance $Z^*=Z'-iZ''$ were performed in the frequency range 10 mHz to 100 kHz for a signal amplitude of 5 mV. The complex differential capacitance $C_S^*=C_S'-iC_S''$ was determined from the impedance data through the relation $C_S'=Z''/\omega|Z|^2S$ and $C_S''=Z'/\omega|Z|^2S$, where $\omega=2\pi f$ and f denotes frequency.

7.4 Results and Discussion

7.4.1 Synthesis of NiONT: Characterization and Elemental Analyses

Figure 7.1b and 7.1c respectively present TEM images of the MWNT before and after electroless deposition of a layer of nickel that encapsulates the MWNT. Comparison of the images in Figures. 7.1b, 7.1c and 7.1d with their scale bars indicates that Ni deposition on the MWNT at $\gamma = 7$ is ≈40-50 nm. Annealing of Ni-MWNT results in oxidation of both nickel and carbon, which leaves a ≈50 nm tubular vacancy, as shown through the dark field STEM image of a NiONT in Figure 7.1d.

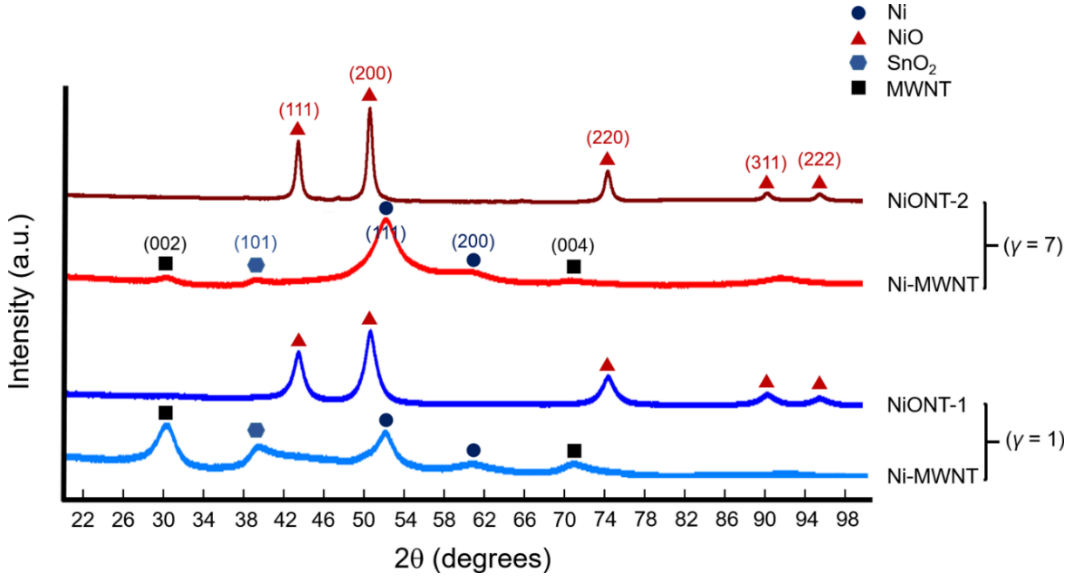

Figure 7.2: XRD patterns for Ni-MWNTs and NiONTs for two different Ni:MWNT weight ratios, i.e., $\gamma = 1$ and 7. The absence of diffraction peaks corresponding to MWNTs and the appearance of a diffraction peak corresponding to nickel oxide after annealing confirms the removal of carbon and oxidation of Ni to NiO.

The XRD analysis presented in Figure 7.2 confirms the existence of crystalline nickel (Ni, PDF No. 00-004-0850) and hexagonal carbon (multiwalled carbon nanotubes, PDF No. 00-058-1638) on Ni-MWNT samples for the two different Ni:MWNT weight ratios $\gamma = 1$ and 7. Comparing the ratios of the intensities of the diffraction peaks for the Ni (111) and (200) planes and likewise for the MWNT (002) and (004) planes for the two samples shows how the amount of deposited nickel increases by increasing the Ni:MWNT weight ratio. The XRD patterns for the annealed NiONT samples NiONT-1 and NiONT-2 confirm the absence of MWNTs and Ni, since these two materials are oxidized to CO_2, which is released, and NiO. Here, the diffraction peaks corresponding to nickel oxide (NiO, PDF No. 01-089-3080) confirm the presence of NiONTs, supporting our hypothesis of the formation of a crystalline nickel oxide phase.

Figure 7.3 presents dark field STEM images of the as-prepared NiONT for $\gamma = 1$ and 7. The STEM images for NiONT-1 (Figure 7.3, Panels a.1-a.5) show that both nickel oxide nanotubes and nickel oxide agglomerates are present, creating porous structures. The average outer diameter of the NiONTs is ≈60-80 nm, average inner diameter ≈30-40 nm and average wall thickness ≈10-25 nm. The STEM images for NiONT-2 (Figure 7.3, Panels b.1-b.5) show that NiO agglomeration is reduced. Here, the average NiONT outer diameter ≈160-180 nm, average inner diameter ≈60-80 nm, and average wall thickness ≈40-60 nm. The thin and porous Ni coating (~10-25 nm) [19] on the MWNT for $\gamma = 1$ has relatively low thermal stability so that it undergoes sintering during annealing [309, 310] into porous microstructures, as shown in Figure 7.3, Panels a.1-a.2. This is also evident from the morphology and the internal cavity in the NiONT-1 that are not smooth or continuous as shown in Figure 7.3, Panels a.4-a.5. In contrast, for $\gamma = 7$, the thickness of the Ni layer deposited on a MWNT is ≈40-60 nm [19], which is thermally more stable so that the tubular shape of individual MWNTs is retained during annealing, as is evident from Figure 7.3, Panel b. Additionally, the morphology and the internal cavity for NiONT-2 are smooth and continuous as shown in Figure 7.3, Panels b.3-b.5. These images indicate that larger NiONT agglomerates are produced when $\gamma = 1$ and more distinct tubular vacancies remain when $\gamma = 7$.

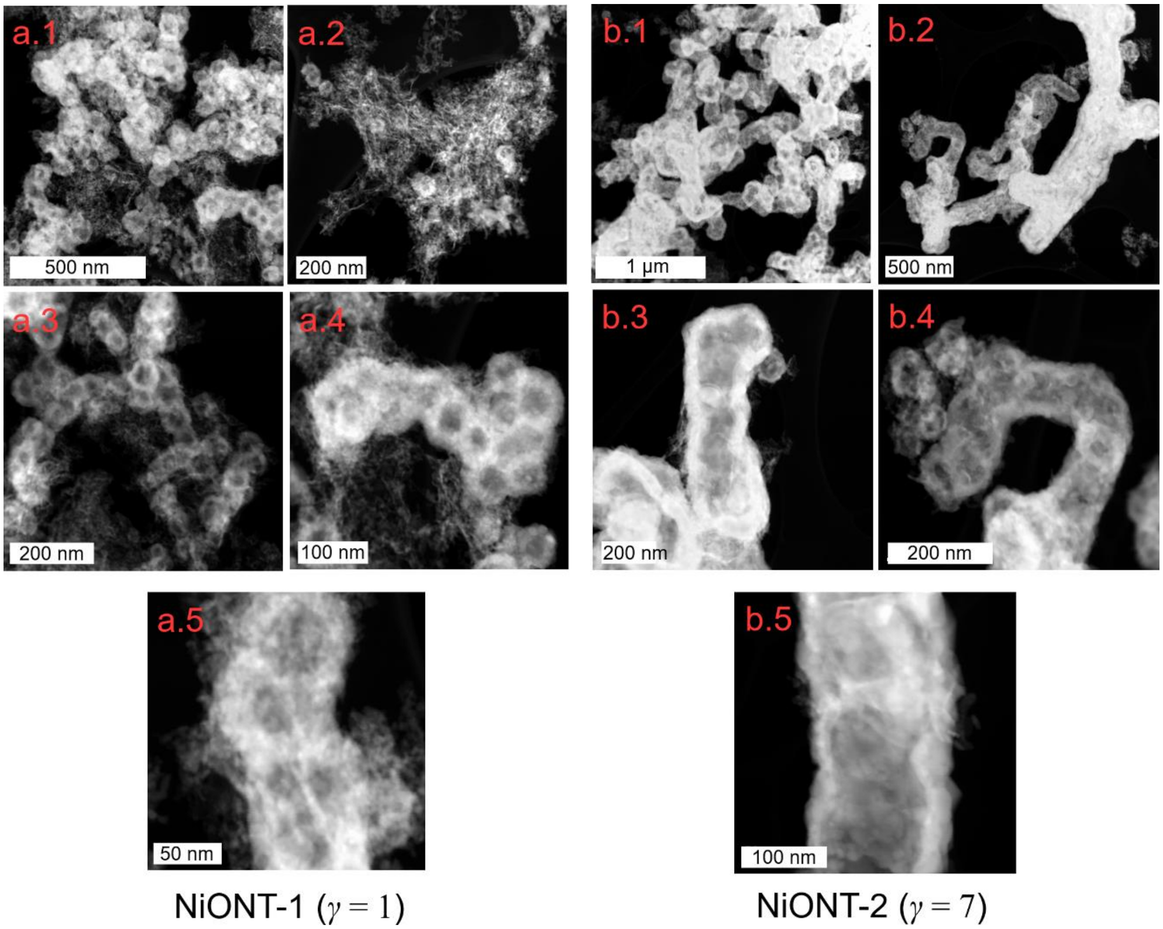

Figure 7.3: TEM and STEM images of NiONT for two different Ni:MWNT weight ratio $\gamma = 1$ and 7 at different magnifications. Panels a.1 and a.2 include TEM images and panels a.3 & a.4 show dark field STEM images of NiONTs produced at $\gamma = 1$. Panels b.1 & b.2 likewise show TEM images and panels b.3 & b.4 dark field STEM images for NiONT synthesized at $\gamma = 7$.

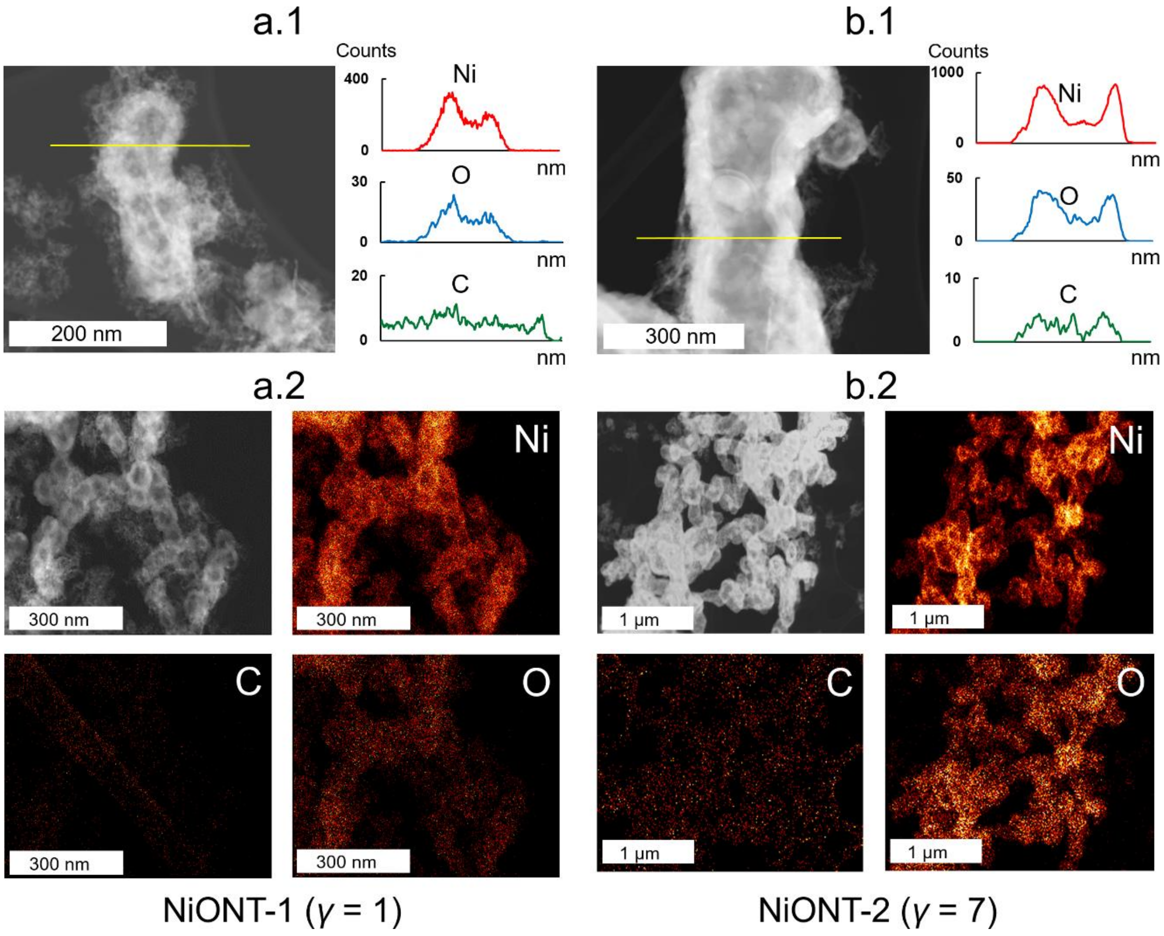

Figure 7.4: EDX elemental analyses of NiONT for elemental Ni, C and O. (Panels a.1 and b.1) along with line scans of the NiONTs synthesized at $\gamma = 1$ and 7, respectively. The line scans are taken across the cross-sections of the respective NiONTs shown in the accompanying STEM images. Panels a.2 and b.2 contain elemental maps of NiONT for $\gamma = 1$ and 7, respectively.

The EDX/STEM line scans for samples NiONT-1 and NiONT-2 are presented in Figure 7.4, Panels a.1 and b.1, respectively. The line scans, taken across the cross-sections of the respective NiONTs shown in the accompanying STEM images, confirm the existence of elemental Ni and O and absence of C in both samples. As evidence of vacancies, the magnitudes of the Ni and O line scan profiles are significantly reduced inside the nanotubes.

The EDX/STEM elemental mapping for NiONT-1 and NiONT-2 is presented in Figure 7.4, Panels a.2 and b.2, respectively. These maps provide additional confirmation that while Ni and O exist together outside the vacancies, there is a negligible amount of C in both samples. The small indication of elemental C is attributed to the background lacey grid used to hold the TEM samples.

7.4.2 Stability of the Colloidal Suspension

Chemical bonding of the dispersants to the particle surfaces is a prerequisite for efficient dispersion. Previous investigations [311] have shown that charged molecules with chelating ligands provide efficient dispersion of oxide nanoparticles. Since, molecules with single chelating ligands lead to relatively weak interactions with a particle surface, efficient dispersion of relatively large nanotubes requires stronger adsorption of a dispersant on a particle surface, such as one containing multiple chelating ligands [312, 313].

The chelating polyelectrolyte, PAZO (Figure 7.5a) is a dispersing agent that was recently employed for efficient dispersion and colloidal processing of nanoparticles [312, 313]. It is an anionic polyelectrolyte containing chelating monomers (Figure 7.5a). The salicylate groups of such monomers provide multiple adsorption sites, facilitating strong bonding to a particle surface. Figure 7.5b illustrates the bonding of a PAZO monomer, which involves complexation of a metal atom on the particle surface. The creation of multiple bonds leads to strong PAZO adsorption on nanoparticles of different types, including oxides, hydroxides and metals. Therefore, PAZO is a promising material for the dispersion of larger nanoparticles, such as NiONTs and Ni-MWNTs. Successful colloidal processing of nanoparticles using PAZO has generated interest in the search for new chelating polyelectrolytes and investigation of new bonding mechanisms, and PSSA attracted our attention as a chelating polyelectrolyte. Its chelating properties are related to carboxylic groups of PSSA monomers (Figure 7.5c). It is known that PSSA forms complexes with metal ions in solutions [314-316]. The chelating mechanism involves two carboxylic groups of each monomer [316]. We suggest that a similar mechanism leads to the complexation of Ni atoms on the NiONT and Ni-MWNT surfaces (Figure 7.5d). We also hypothesize that the multiple chelating bonds result in efficient adsorption of PSSA on both materials, which is important for their co-dispersion, prevention of agglomeration and improved mixing.

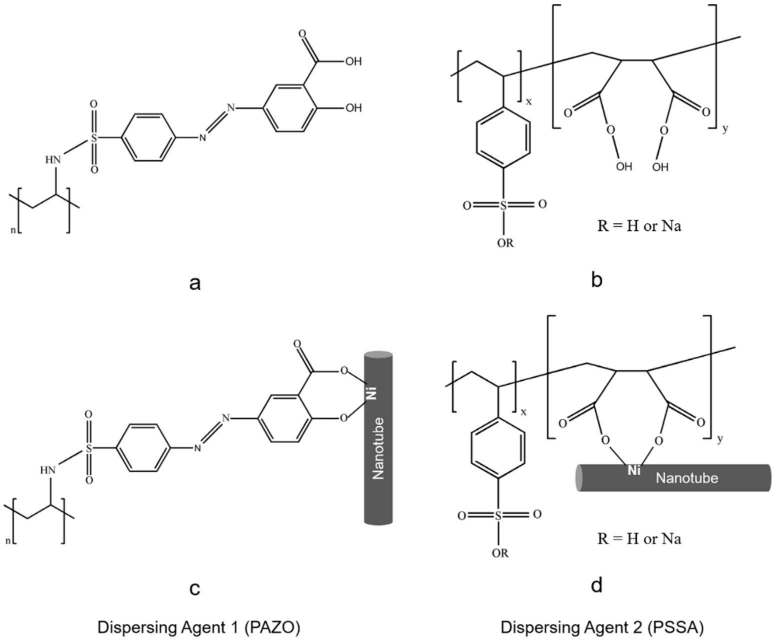

Figure 7.5: Chemical structures of (a) PAZO and (b) PSSA and corresponding adsorption mechanisms involving complexation of (c) salicylate groups of PAZO and (d) carboxylic groups of PSSA with Ni atoms on the surfaces of (c) Ni-MWNT and (d) NiONT.

Our aim is to fabricate a composite electrode with NiONTs (γ = 1 and 7) as the active material and Ni-MWNTs (γ = 1) as the conductive additive and characterize its electrochemical performance. The electrochemical performance of the electrode has a strong dependence on the microstructure of the active material. Good dispersion and mixing of the individual components in the composite active material are of critical importance for the development of advanced electrodes. Therefore, we paid attention to the dispersion and mixing of the individual components in the slurries, used for electrode fabrication.

We used Ni-MWNTs (γ = 1) only as the conductive additive, since their thin nickel layer reduced the charge transfer length as well as the specific mass of the electrode. The thin Ni layer allowed adsorption of PAZO and PSSA by mechanisms involving chelation of surface Ni atoms (Figure 7.5c-d). A similar mechanism, involving the chelation of Ni atoms on the NiONT surface allowed PAZO and PSSA to be adsorbed on the active material. Six different suspensions were prepared for three materials, i.e., NiONT-1, NiONT-2 and Ni-MWNT (γ = 1), with two dispersing agents, i.e. PAZO and PSSA, which were subjected to sedimentation tests and DLS.

Sedimentation tests showed that the addition of PAZO or PSSA to Ni-MWNT and NiONT suspensions resulted in improved suspension stability. Measurements of electrophoretic mobility showed that Ni-MWNT and NiONT were negatively charged. Figure 7.6 shows that the electrophoretic mobilities of Ni-MWNT (γ= 1) in the suspensions containing PAZO and PSSA were -0.40 and -0.82 μmcms^{-1}V^{-1}, respectively. In addition, NiONT-2 had higher electrophoretic mobility in both (PAZO and PSSA) suspensions (-

0.84 and -1.14 μmcms^{-1}V^{-1}, respectively) than NiONT-1 (-0.67 and -0.91 μmcms^{-1}V^{-1}, respectively). The lower suspension stability of NiONT-1 is attributed to the formation of a larger number of microscopic agglomerates, as discussed in section 7.4.1. Since fewer tubular vacancies remain in the structure, there is a significant reduction in the surface area to mass ratio, which reduces the suspension stability of these particles. Thus, NiONT-2 was preferred over NiONT-1 for electrode fabrication.

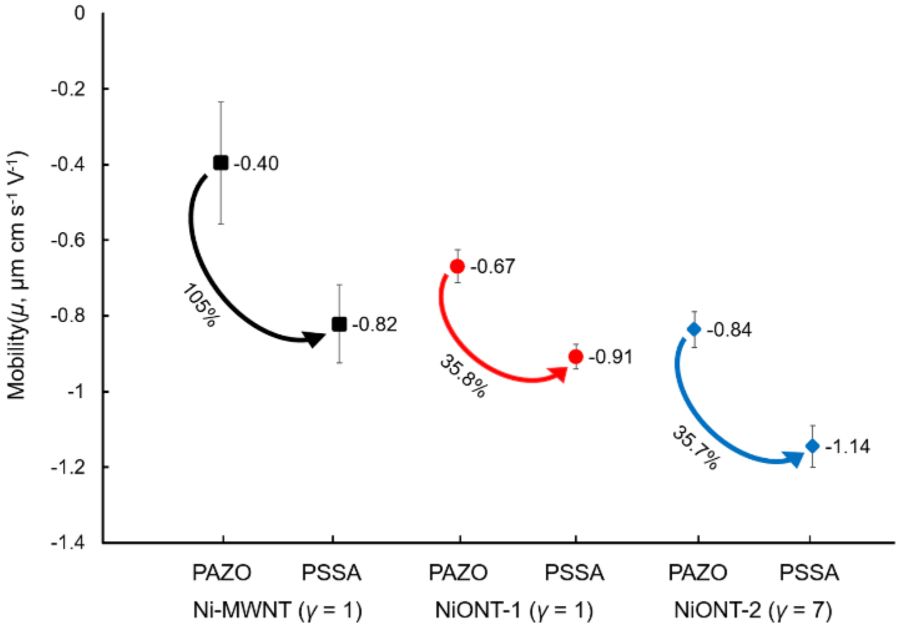

Figure 7.6: Electrophoretic mobility of Ni-MWNTs (for γ = 1) and NiONTs (for γ = 1 and 7) with two dispersing agents, PAZO and PSSA.

The use of PSSA as a dispersant allowed for improved suspension stability and higher electrophoretic mobility as compared to PAZO for all samples. The higher dispersion and electrophoretic mobility for both Ni-MWNTs and NiONTs achieved with PSSA is due to stronger PSSA adsorption on both types of nanoparticles. From the perspective of polyelectrolyte adsorption, the chelating groups exert a strong influence on polymer adsorption. The adsorbed polymer provides electrosteric dispersion of Ni-MWNT and NiONT, which facilitates their improved mixing.

7.4.3 Electrochemical Performance

Based on the suspension tests results, the electrode was fabricated with NiONT-2 as the active material, Ni-MWNT ($\gamma = 1$) as a conductive additive, and PSSA as dispersing agent. A probe sonicator was used for 30 min to prepare a dispersion containing a 5 ml PSSA solution (0.4 g L^{-1} in 60% ethanol solution), 2 ml PVB binder solution (0.75 g L^{-1} in 100% ethanol solution), 40 mg NiONT ($\gamma = 7$), and 10 mg of Ni-MWNT ($\gamma = 1$). The prepared colloidal dispersion was heated overnight at 60 °C until a dense slurry was obtained. This slurry was used to impregnate the Ni foam current collector, which was dried thereafter in air and subsequently pressed to 30% of its original thickness using a rolling press. The mass of the impregnated material was 24.1 mg cm^{-2}.

The prepared electrode was tested for the electrochemical performance using a potentiostat. Figure 7.7a shows typical CV results at different scan rates. The shape of the CVs in the selected voltage window of 0-0.5 V is similar to the corresponding literature data for NiO composites prepared by other methods [282, 286, 289, 292, 305, 317]. The gravimetric specific capacitance of 245.3 F g^{-1} is comparable with literature data for electrodes containing a smaller active mass [282, 295, 306, 307, 317, 318]. It is important to note that in our investigation the high gravimetric capacitance was achieved for electrodes with a relatively high mass of 24.1 mg cm^{-2}. As a result, we were able to realize relatively high areal capacitance of 3.28 F cm^{-2} at a scan rate of 2 mV s^{-1}.

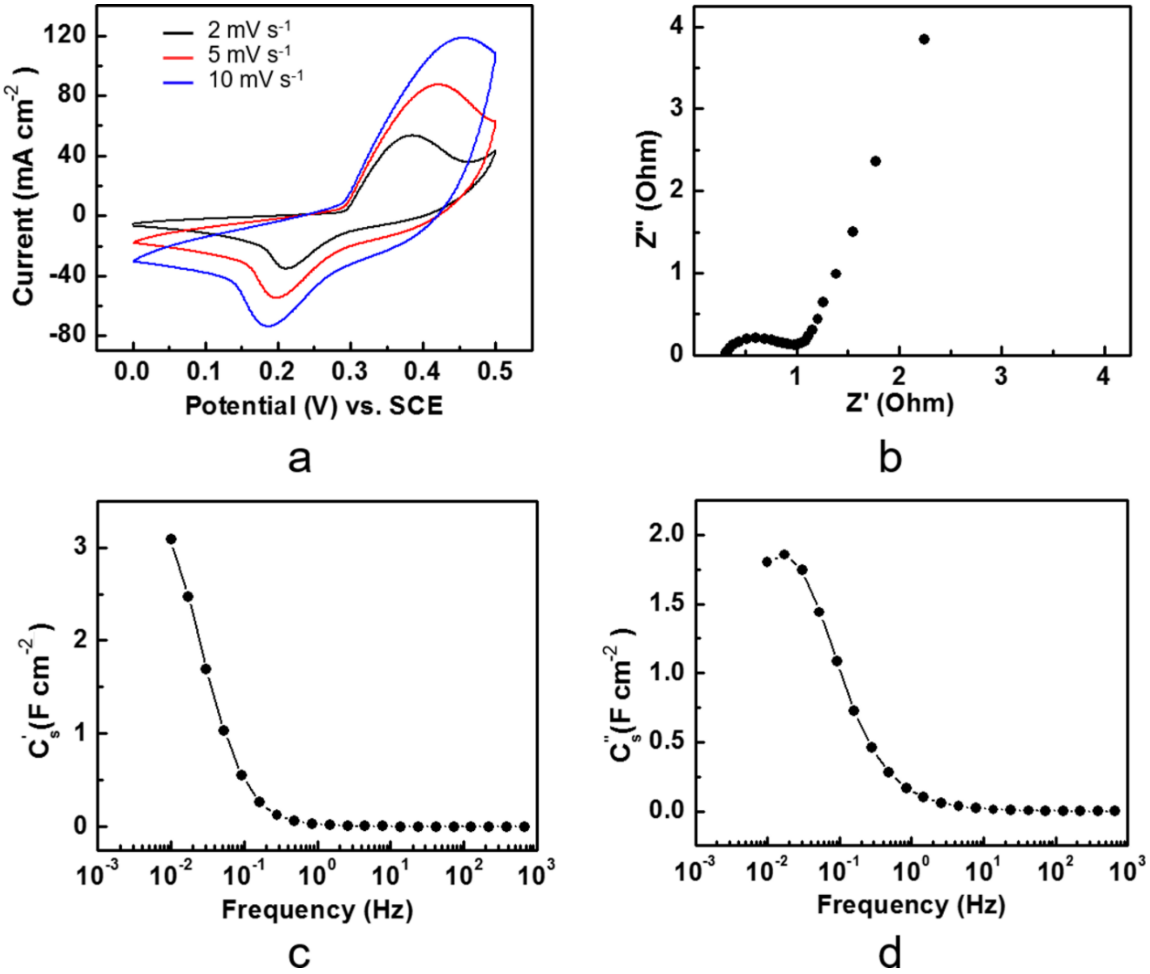

Figure 7.7: (a) CVs at different scan rates, (b) Nyquist plot of complex impedance, (c) real and (d) imaginary components of AC capacitance calculated from the impedance data versus frequency for NiONT (80%) - Ni-MWNT (20%) composite electrodes with active mass of 24.1 mg/cm^2.

The complex impedance data for the electrodes is presented in Nyquist plot in Figure 7.7b. The electrodes exhibited a relatively low resistance $R=Z'$ (Figure 7.7b). The relatively low Z'' resulted from a high capacitance. The components of complex AC capacitance, calculated from the CV data and plotted versus frequency, showed a relaxation type dispersion, as indicated by reduction in Cs' with increasing frequency and corresponding relaxation maximum of *Cs''* (Figure 7.7c and 7.7d). The low frequency capacitance *Cs'*, calculated from the impedance measurements is comparable with capacitance *Cs*, obtained from CV data at a scan rate of 2 mV s^{-1}.

7.5 Conclusion

We present a rapid method to synthesize NiONTs with different wall thicknesses, using MWNTs as the sacrificial template. This method, which can be scaled for bulk synthesis, is simpler and more cost effective than existing traditional methods that are intricate, time consuming and mostly useful for producing small batches of material. The NiONTs replicated the external dimensions of the MWNT template and their thickness varies with Ni:MWNT ratio during electroless plating. However, fractals of nickel oxide agglomerates are formed at a lower Ni:MWNT weight ratio of $\gamma=1$. The new chelating polyelectrolytes exhibit good colloidal stability and efficient mixing of NiONTs and Ni-MWNTs. The PSSA polyelectrolyte was more effective for stabilising both the Ni-MWNT and NiONT dispersions. The use of advanced slurry formulations allowed electrodes with a relatively high gravimetric capacitance of 245.3 F g^{-1} to be fabricated with high active mass loadings. As a result, a high areal capacitance of 3.28 F cm^{-2} was achieved. Thus, we conclude that our novel synthesis of NiONTs using sacrificial templates and the fabrication of electrodes based on these materials are promising for the development of advanced energy storage devices.

8. Summary and Future Work

8.1 Thesis Summary

Since the discovery of the CNTs in the last century, they have been recognized as important engineering nanomaterials because of their superior physical properties. However, their commercial use in large-scale applications is limited due to their high production cost. Recently, several techniques have emerged to reduce both the production cost and synthesis complexities. MWNTs, the cheapest available form of CNTs for commercial use suffer from several key challenges that compromise their performance.

Commercially available MWNTs are produced in the form of powder containing randomly oriented and entangled fragments, which are also restricted by their imperfect anisotropic and non-polar behaviour. Here, an experimental investigation focussed on the magnetization of MWNTs via different functionalization routes is conducted. Decorating CNTs with magnetic nanoparticles (MNPs) not only expedites their organization with a magnetic field, but also provides new hydrophilic and polar surfaces on the CNTs' original surfaces. This thesis demonstrates the efficacy of magnetized MWNTs over the commercially available MWNTs.

Magnetization of MWNTs via covalent functionalization is examining for six different routes of decorating MWNTs by *in situ* co-precipitation of magnetic nanoparticles. Four of these six routes are newly reported here. Functionalization using H_2SO_4 minimizes MWNT loss during synthesis and also yields a decoration density close to unity. Although mixtures of HNO_3 and H_2SO_4 are commonly employed, we found these to inflict significant structural damage to MWNTs. The damage results in short MWNT fragments, which are lost to the filtrate upon filtration. This loss of MWNTs can be as high as ≈ 46% (w/w) and is accompanied with significant nanotube oxidation that has an oxygen content up to 15.23%. Functionalization with either HNO_3 or H_2SO_4 is much less destructive than their mixtures with equal proportion. Despite considerable loss of MWNTs, the filtration step is necessary as it removes remaining traces of acid from the dispersion prior to co-precipitation. Elimination of the filtration step allows the acids to react with iron ions to produce nonmagnetic byproducts that compromise the magnetization of the MWNTs. Overall, (a) functionalizing with HNO_3 or H_2SO_4, followed by (b) filtration, (c) washing, (d) drying and (e) subsequent *in situ* coprecipitation of MNPs yields the best quality MNPs, relatively high magnetized MWNTs (mMWNT) yield of ≈ 95%, magnetization ratio close to an intended value of unity, reasonably uniform MNP distribution on the mMWNT surfaces, and negligible MWNT shortening and damage.

MWNTs are decorated by *in situ* co-precipitation with different magnetic nanoparticles (MNPs) for varying magnetization weight ratios γ (MNP:MWNT) in the range of 1-2. The decoration of MWNTs with MNPs depends upon the availability of activation sites on the outer surfaces of CNTs. The activation sites are completely utilized when γ reaches a specific value. Typically γ =1 provides uniform decoration of MNPs and minimum agglomeration. At a higher value of γ, although the number of MNPs exceeds the activation sites, decoration still continues with nanoparticle agglomerating perpendicular to the MWNT surface. The chemical composition of MNPs influences the magnetic properties of mMWNTs. Fe_3O_4 with a high Curie temperature produces mMWNTs with the highest magnetic saturation of M_s = 30.7 emu.g^{-1}. These mMWNTs exhibit the weakest sensitivity to a temperature increase of 60 K above 300 K with a corresponding reduction of 7.7% in M_s. $Mn_{0.2}Cu_{0.2}Zn_{0.6}Fe_2O_4$, and $Cu_{0.4}Zn_{0.6}Fe_2O_4$ MNPs have lower Curie temperatures. Thus mMWNTs produced with these MNPs have lower M_s values (10.5 and 16.6 emu.g^{-1}, respectively) and are more sensitive to a temperature increase (with up to 48.9% and 46.6% reductions in M_s).

The mMWNTs are successfully suspended to create novel and hitherto unreported magnetoresponsive conductive colloids (MCCs) with moderate colloidal stability. Synthesis of an MCC involves both the preparation of ferrofluids and of mMWNTs. Three separate magnetoresponsive conductive colloids are prepared using the three different types of MNPs (γ =1). All colloids have moderate suspension stability since their mean zeta potential $\zeta \approx$ -33 mV. Their electric conductivities of 150-170 mS.cm^{-1} are much higher than the conductivity of the deionized water which is used as the dispersing medium and is a poor conductor. The chemical composition of the MNPs decorating the MWNT influences the electric conductivity of the respective MCC. For instance, increasing the copper content in an MNP improves the electric conductivity. In summary, a novel methodology to produce stable magnetoresponsive conductive colloidal suspensions with tunable magnetic and electrical properties is provided. These colloidal suspensions are a promising new class of material that could be used for applications where a magnetic response, or action from a distance, must be coupled with a viable material electrical conductivity.

By adapting MCC synthesis, a biological magnetic ink is produced that contains Antibodies (Abs) that are immobilized on the surfaces of mMWNTs, which are dispersed in DI water containing Tween 20 as bio-compatible surfactant. Bio-ink synthesis is straightforward and does not involve the use of intermediate reagents. An applied magnetic field dynamically organizes the magnetized and functionalized CNTs, printing them into an electrically responsive strip that serves as a biosensor to detect specific Antigens (Ags). Unlike previous methods, a magnet is not required during sensing, facilitating simple integration of the sensor into an electric circuit. The sensor detects picomolar c-Myc concentrations within a minute and distinguishes between c-Myc and BSA samples of different concentrations through the change in the sensor current. The change, which occur due to the specific Ab-Ag binding kinetics, in real time is larger at higher Ag concentrations. The detection technique is simple, inexpensive and rapid as compared to typical cyclic voltammogram analysis. Once the ink is synthesized, the time required to fabricate the sensing strip is less than 5 minutes, excluding the ink drying time. Semi-quantitative Ag detection with picomolar sensitivity occurs within a minute after a sample is dispensed on the biosensor. This Bio-ink and sensor can be further tailored to detect different Ags.

Magnetization of MWNTs via non-covalent functionalization is developed by depositing nickel nanocrystals on MWNTs through electroless plating using a chemical metal reduction method for different Ni:MWNT weight ratios γ = 1, 7, 14, and 30. Once Ni deposits on palladium catalyst particles, it forms nanoclusters on the MWNT surfaces. With increasing Ni content, neighboring nanoclusters merges to produce a continuous Ni coating that completely encapsulates the MWNT. For larger γ, despite Ni coverage over the palladium catalyst, deposition of Ni continues through autocatalysis by the deposited nickel. The Ni-MWNT hybrid material (NiCH) contains encased MWNTs that are connected by Ni networks. Increasing γ improves the metallic connections between plated MWNTs so that the sparse MWNT network for $\gamma = 1$ becomes denser for $\gamma = 14$ with the formation of microscale NiCH structures. In such structures, Ni forms a conductive metallic matrix with MWNTs as the reinforcing filler material. The Ni-MWNT hybrid material with $\gamma = 1$, and 7 have higher elastic modulus $E \sim 18.3$ and 58.7 GPa respectively than pure MWNTs ($E \sim 12.5$ GPa), i.e., increasing γ enhances the elastic modulus. The magnetic properties of the NiCH are superior to those of the original diamagnetic MWNTs (e.g., M_s increases), and increases with γ. This electroless plating method is promising for improving the mechanical and magnetic properties of MWNTs and thus reducing their electrical resistance.

Ni-MWNT macrostructures with controlled morphologies using the NiCH are also fabricated. Continuous nickel deposition on the Ni-MWNT ($\gamma = 1$) hybrid sample can either result in vertically-aligned porous 3D macrostructures or horizontally-aligned hybrid denser and flatter macrostructures. These macrostructures could be utilized for nano and microscale filtration, as well as for printing electric circuits. The hydrophilic layer of nickel enhances the Ni-MWNT dispersion, which was used to synthetize electrically conductive inks by simply dispersing different concentrations of Ni-MWNT ($\gamma = 7$) samples in water. An ink with 8% volume concentration has a relatively low electrical resistivity of 5.9 Ωm.

Using a magnet to print inks containing low Ni-MWNT concentrations reduced the electric resistivity of the printed lines by 200-300Ωm than similar printed ones without the magnet.

The properties of nanocomposites are tailored by organizing nanoparticles within a polymer matrix, e.g., for aerospace, automobile and infrastructure applications. Electroless metal plating of commercially available MWNTs is a simple, direct, inexpensive and scalable method to improve and tune the mechanical and electrical properties of a nanocomposite. Since the resulting Ni-MWNTs are magnetic nanoparticles, an external magnetic field is applied from a distance to align these nanoparticles within the nanocomposite. These magnetized nanoparticles are introduced into an epoxy matrix at a relatively low 0.25-1% volume fraction, where, they are aligned with the external magnetic field along particular directions. Deposition of nickel over an MWNT improves the interfacial bonding between the resulting Ni-MWNT hybrid nanoparticles and the surrounding polymer matrix. This alignment enhances the properties of the composite, such as its tensile strength, elastic modulus and AC electrical resistivity. By changing this alignment, it becomes possible to tailor the properties of the resulting composite material. The alignment imparts anisotropic properties to the bulk material, but when the nanoparticles are aligned in perpendicular directions in two sequential layers, this coupled orientation produces an effectively isotropic composite material.

The tensile strength of a nanocomposite containing 0.25% volume fraction of aligned Ni-MWNTs is found to be ~9% higher than of pure epoxy and ~47% higher than the composite containing a similar volume fraction of randomly dispersed nanoparticles. Nanoparticle alignment reduces the variability in tensile strength measurements since the dispersion homogeneity in different samples is improved along the direction of the magnetic field. Nanocomposite with 0.25 vol% of aligned Ni-MWNTs, shows a ~40% lower AC electric resistivity along the alignment direction than that of pure epoxy and ~20% lower than of the composite containing same volume fraction of randomly dispersed nanoparticles. Alignment of anisotropic nanoparticles in multiple directions within a polymer matrix to produce an effectively isotropic nanocomposite is demonstrated for the first time. The AC electrical resistivity of an epoxy nanocomposite fabricated with 0.25 vol% Ni-MWNTs aligned in perpendicular directions in two sequential layers is effectively isotropic and ~11.6% lower than that of the composite containing a similar fraction of randomly dispersed Ni-MWNTs. Therefore, aligning Ni-MWNTs along multiple directions enables tailoring of the physical properties of their epoxy composites, as well as their direction-dependent bulk behaviour, which is potentially useful for many engineering solutions.

Metal plated MWNTs are then used as a template to synthesize metal oxide nanotubes (e.g. NiO) with different wall thicknesses, using MWNTs as the sacrificial template. Since nickel oxide nanotubes (NiONT) applications are limited by the lack of simple and low cost fabrication methods, a scalable method to overcome this limitation is proposed. The MWNTs are encapsulated with Ni by depositing the metal through electroless deposition to synthesize the Ni-MWNT hybrid material. These encapsulated nanotubes are annealed in air at temperatures much lower than the melting temperature of Ni (i.e. 500°c) so that both metal and carbon in MWNTs oxidizes to NiO and CO_2 respectively. Release of the gaseous carbon dioxide results in a tubular vacancy where the

MWNTs previously existed. Thus, the residual NiO retains the shape of the (now oxidized) underlying MWNT template, producing a NiONT. However, fractals of nickel oxide agglomerates are formed at a lower Ni:MWNT weight ratio of γ=1. The wall thickness of this nanotube may be controlled by varying the mass of Ni deposited, which could allow control over the dimensions of the synthesized NiONTs.

The charge storage capacity of the NiONT-based electrode of an electrochemical supercapacitor have been investigated. The electrode is fabricated with NiONTs as the active material, nickel coated carbon nanotubes (Ni-MWNTs) as a conductive additive, and a dispersing agent. A new chelating polyelectrolyte is used as the dispersing agent to achieve high colloidal stability both for Ni-MWNTs and NiONTs. A relatively high gravimetric specific capacitance of 245.3 F g^{-1} and areal capacitance of 3.28 F cm^{-2} is achieved with a mass loading of 24.1 mg cm^{-2} which meets the requirement of practical applications. Thus, the novel synthesis of NiONTs using sacrificial templates and the fabrication of electrodes based on these materials are promising for the development of advanced energy storage devices.

8.2 Future Work

Means to control and enhance the magnetization of MWNT via both covalent and non-covalent functionalization have been investigated for some important engineering applications (e.g. nanofluids, biosensors, nanocomposites, and supercapacitors). However, significant future work is required for improving the synthesis methods.

These additional efforts should consider how covalent functionalization of CNTs can be accomplished with other non-acid oxidizing agents to eliminate the hazards associated with using large quantity of acids and their disposal. The suspension stability and thermal conductivity of MCCs based on covalently magnetized CNTs must also be investigated. For the biosensor, the MCCs must be adapted for different specific antibody-antigen combinations. The binding kinetics of the antibodies over CNTs require detailed investigation to enable semi-quantitative prediction of sensor sensitivity. The bio-ink needs more attention for printing a continuous and stable sensing strip.

Non-covalent functionalization of CNTs requires further study to improve the magnetic properties of the produced Ni:CNT hybrid nanomaterials. Heat treatment in a controlled atmosphere to enhance the nickel crystallinity, changing the reducing agent to prevent contamination with phosphorus, or replacing nickel with other ferromagnetic metals could be different ways for future investigation. Further, utilizing a magnetic field to control the growth of Ni:CNT hybrid nanomaterials into macrostructures requires more attention, including the effect of using different complex configurations of the magnetic field. These macro structure must be investigated for other novel applications.

The successful tailoring of both anisotropic and isotropic properties of bulk polymeric composites utilizing multi-directional alignment of Ni-coated MWNT in sequential layers should be further investigated. Other means to enhance the alignment to better the composite material’s anisotropic behaviour should be pursued. Further, the effect of alignment along several, say three or four directions, on the behaviour of the different physical properties should be investigated. Modeling and experimental investigations should be conducted in tandem to highlight the effect of the multi-directional alignment of the Ni-MWNT fragments in multiple layers on the thermal conductivity of the bulk material.

The successful synthesis of nickel oxide nanotubes based on MWNT as a sacrificial templated utilizing the metal plating with nickel requires further verification of the same concept with different metals (e.g. Cu, Fe, Au, and Ag). The technique should be developed to synthesize either metal or metal oxide nanotubes on demand.

9. References

1. Gubin, S.P., *Magnetic nanoparticles*. 2009: John Wiley & Sons.
2. Cao, G., *Nanostructures and nanomaterials: synthesis, properties and applications*. 2004: World Scientific.
3. Reithmaier, J., et al., *Nanostructured materials for advanced technological applications*. 2009: Springer Science & Business Media.
4. Simonis, M. and S. Schilthuizen, *Nanotechnology: innovation opportunities for tomorrows defence.* 2009.
5. Scoville, C., et al., *Carbon Nanotubes.* Notes Lecture.
6. Coville, N.J., et al., *A review of shaped carbon nanomaterials.* South African Journal of Science, 2011. **107**(3-4): p. 01-15.
7. Kaushik, B.K. and M.K. Majumder, *Carbon Nanotube Based VLSI Interconnects: Analysis and Design*. 2015: Springer.
8. Li, H., et al., *Carbon nanomaterials for next-generation interconnects and passives: physics, status, and prospects.* IEEE Transactions on Electron Devices, 2009. **56**(9): p. 1799-1821.
9. Jariwala, D., et al., *Carbon nanomaterials for electronics, optoelectronics, photovoltaics, and sensing.* Chemical Society Reviews, 2013. **42**(7): p. 2824-2860.
10. Kamat, P., *Carbon nanomaterials: Building blocks in energy conversion devices.* Interface, 2006. **15**(1): p. 45-47.
11. Schwenke, A.M., S. Hoeppener, and U.S. Schubert, *Synthesis and modification of carbon nanomaterials utilizing microwave heating.* Advanced Materials, 2015. **27**(28): p. 4113-4141.
12. Popov, V.N., *Carbon nanotubes: properties and application.* Materials Science and Engineering: R: Reports, 2004. **43**(3): p. 61-102.
13. De Volder, M.F., et al., *Carbon nanotubes: present and future commercial applications.* Science, 2013. **339**(6119): p. 535-539.
14. Ciraci, S., et al., *Functionalized carbon nanotubes and device applications.* Journal of Physics: Condensed Matter, 2004. **16**(29): p. R901.
15. Chen, R.J., et al., *Noncovalent functionalization of carbon nanotubes for highly specific electronic biosensors.* Proceedings of the National Academy of Sciences, 2003. **100**(9): p. 4984-4989.
16. Atieh, M.A., *Effect of functionalized carbon nanotubes with carboxylic functional group on the mechanical and thermal properties of styrene butadiene rubber.* Fullerenes, Nanotubes and Carbon Nanostructures, 2011. **19**(7): p. 617-627.
17. Abdalla, A.M., et al., *Magnetoresponsive conductive colloidal suspensions with magnetized carbon nanotubes.* Journal of Magnetism and Magnetic Materials, 2017. **421**: p. 292-299.
18. Abdalla, A.M., S. Ghosh, and I.K. Puri, *Decorating carbon nanotubes with co-precipitated magnetite nanocrystals.* Diamond and Related Materials, 2016. **66**: p. 90-97.

19. Abdalla, A.M., et al., *Fabrication of nanoscale to macroscale nickel-nultiwall carbon nanotube hybrid materials with tunable material properties.* Materials Research Express, 2016. **3**(12): p. 125014.
20. Abdel Fattah, A.R., et al., *Nickel Nanoparticles Entangled in Carbon Nanotubes: Novel Ink for Nanotube Printing.* ACS Applied Materials & Interfaces, 2016. **8**(3): p. 1589-1593.
21. Pisanello, F., et al., *GHz properties of magnetophoretically aligned iron-oxide nanoparticle doped polymers.* ACS Appl Mater Interfaces, 2013. **5**(8): p. 2908-14.
22. Shin, J., et al., *Magnetic manipulation of bacterial magnetic nanoparticle-loaded neurospheres.* Integrative Biology, 2014. **6**(5): p. 532-539.
23. Bonnemay, L., C. Hoffmann, and Z. Gueroui, *Remote control of signaling pathways using magnetic nanoparticles.* Wiley Interdisciplinary Reviews: Nanomedicine and Nanobiotechnology, 2015. **7**(3): p. 342-354.
24. Gabayno, J.L.F., et al., *Controlled manipulation of Fe 3 O 4 nanoparticles in an oscillating magnetic field for fast ablation of microchannel occlusion.* Nanoscale, 2015. **7**(9): p. 3947-3953.
25. Yi, L., G. Yu, and X. Chenjie, *Using magnetic nanoparticles to manipulate biological objects.* Chinese Physics B, 2013. **22**(9): p. 097503.
26. Iijima, S., *Helical microtubules of graphitic carbon.* Nature, 1991. **354**(6348): p. 56-58.
27. Iijima, S. and T. Ichihashi, *Single-shell carbon nanotubes of 1-nm diameter.* Nature, 1993. **363**: p. 603-605.
28. Bethune, D., et al., *Cobalt-catalysed growth of carbon nanotubes with single-atomic-layer walls.* Nature, 1993. **363**: p. 505-507.
29. Dresselhaus, M.S., G. Dresselhaus, and P. Avouris, *Carbon nanotubes: Synthesis, structure, properties and applications* S-Verlag Berlin, Heidelberg and New York, 2001: p. 12-25.
30. Wernik, J.M. and S.A. Meguid, *Recent developments in multifunctional nanocomposites using carbon nanotubes.* Applied Mechanics Reviews, 2010. **63**(5): p. 050801.
31. Varshney, K., *Carbon nanotubes: a review on synthesis, properties and applications.* International Journal of Engineering Research, 2014. **2**(4): p. 660-677.
32. Ren, Z., Y. Lan, and Y. Wang, *Aligned carbon nanotubes: physics, concepts, fabrication and devices*. 2012: Springer Science & Business Media.
33. Jorio, A., G. Dresselhaus, and M.S. Dresselhaus, *Carbon nanotubes: Advanced topics in the synthesis, structure, properties and applications. Topics in applied physics*. 2008: Springer.
34. Saito, R., G. Dresselhaus, and M.S. Dresselhaus, *Physical properties of carbon nanotubes*. Vol. 35. 1998: World Scientific.
35. Gou, J. and K. Lau, *Modeling and simulation of carbon nanotube/polymer composites.* A chapter in the handbook of theoretical and computational nanotechnology. American Scientific Publishers in, 2005: p. 20051-58883.
36. Sinha, N., J. Ma, and J.T. Yeow, *Carbon nanotube-based sensors.* Journal of Nanoscience and Nanotechnology, 2006. **6**(3): p. 573-590.

37. Mahar, B., et al., *Development of carbon nanotube-based sensors—a review.* Sensors Journal, IEEE, 2007. **7**(2): p. 266-284.
38. Antiohos, D., et al., *Carbon nanotubes for energy applications.* Syntheses and Applications of Carbon Nanotubes and Their Composites, 2013: p. 496-534.
39. Dhavle, J., *Carbon nanotubes' use in energy storage.* Storage4, 2013.
40. Popov, V.N. and P. Lambin, *Carbon nanotubes: from basic research to nanotechnology*. Vol. 222. 2006: Springer Science & Business Media.
41. Peng, L.-M., Z. Zhang, and S. Wang, *Carbon nanotube electronics: recent advances.* Materials Today, 2014. **17**(9): p. 433-442.
42. Szabó, A., et al., *Synthesis methods of carbon nanotubes and related materials.* Materials, 2010. **3**(5): p. 3092-3140.
43. Park, S., et al., *Carbon nanosyringe array as a platform for intracellular delivery.* Nano Letters, 2009. **9**(4): p. 1325-1329.
44. Sinha, N. and J.T. Yeow, *Carbon nanotubes for biomedical applications.* NanoBioscience, IEEE Transactions on, 2005. **4**(2): p. 180-195.
45. Zhu, Y., C. Xu, and L. Wang, *Carbon nanotubes in biomedicine and biosensing*. 2011: INTECH Open Access Publisher.
46. Shao, W., et al., *Carbon nanotubes for use in medicine: Potentials and limitations.* Syntheses and Applications of Carbon Nanotubes and Their Composites. Croatia: InTech, 2013: p. 285-311.
47. Ando, Y. and X. Zhao, *Synthesis of carbon nanotubes by arc-discharge method.* New Diamond and Frontier Carbon Technology, 2006. **16**(3): p. 123-138.
48. Rafique, M.M.A. and J. Iqbal, *Production of carbon nanotubes by different routes-a review.* Journal of Encapsulation and Adsorption Sciences, 2011. **1**(02): p. 29.
49. Prasek, J., et al., *Chemical Vapor Depositions for Carbon Nanotubes Synthesis*. 2013, Nova Science Publishers. p. 87-106.
50. Terranova, M.L., V. Sessa, and M. Rossi, *The world of carbon nanotubes: an overview of CVD growth methodologies.* Chemical Vapor Deposition, 2006. **12**(6): p. 315-325.
51. Yokomichi, H., et al., *Morphology of carbon nanotubes synthesized by thermal CVD under high magnetic field up to 10T.* Vacuum, 2008. **83**(3): p. 625-628.
52. O'connell, M.J., *Carbon nanotubes: properties and applications*. 2006: CRC press.
53. Choudhary, V. and A. Gupta, *Polymer/carbon nanotube nanocomposites.* Carbon Nanotubes-Polymer Nanocomposites, 2011: p. 65-90.
54. Goh, P., A. Ismail, and B. Ng, *Directional alignment of carbon nanotubes in polymer matrices: contemporary approaches and future advances.* Composites Part A: Applied Science and Manufacturing, 2014. **56**: p. 103-126.
55. Kimura, T., et al., *Polymer composites of carbon nanotubes aligned by a magnetic field.* Advanced Materials, 2002. **14**(19): p. 1380-1383.
56. Du, J., J. Bai, and H. Cheng, *The present status and key problems of carbon nanotube based polymer composites.* Express Polymer Letters, 2007. **1**(5): p. 253-273.
57. Ovchinnikov, A.A., *Giant diamagnetism of carbon nanotubes.* Physics Letters A, 1994. **195**(1): p. 95-96.

58. Kim, Y., et al., *High-purity diamagnetic single-wall carbon nanotube buckypaper.* Chemistry of Materials, 2007. **19**(12): p. 2982-2986.
59. Lu, S.H., et al., *Improved hydrophobicity of carbon nanotube arrays with micropatterning.* Langmuir, 2009. **25**(21): p. 12806-12811.
60. Homma, Y., et al., *Photoluminescence measurements and molecular dynamics simulations of water adsorption on the hydrophobic surface of a carbon nanotube in water vapor.* Physical Review Letters, 2013. **110**(15): p. 157402.
61. Naseh, M.V., et al., *Functionalization of carbon nanotubes using nitric acid oxidation and DBD plasma.* World Academy of Science, Engineering and Technology, 2009. **49**: p. 177-179.
62. Meng, L., C. Fu, and Q. Lu, *Advanced technology for functionalization of carbon nanotubes.* Progress in Natural Science, 2009. **19**(7): p. 801-810.
63. Yang, F., et al., *Magnetic functionalised carbon nanotubes as drug vehicles for cancer lymph node metastasis treatment.* European Journal of Cancer, 2011. **47**(12): p. 1873-1882.
64. Chen, L., H. Xie, and W. Yu, *Functionalization methods of carbon nanotubes and its applications*. 2011: INTECH Open Access Publisher.
65. Balasubramanian, K. and M. Burghard, *Chemically functionalized carbon nanotubes.* Small, 2005. **1**(2): p. 180-192.
66. Ma, P.-C., et al., *Dispersion and functionalization of carbon nanotubes for polymer-based nanocomposites: a review.* Composites Part A: Applied Science and Manufacturing, 2010. **41**(10): p. 1345-1367.
67. Wei, X. and D.K. Roper, *Tin sensitization for electroless plating review.* Journal of The Electrochemical Society, 2014. **161**(5): p. D235-D242.
68. Worsley, K.A., et al., *Functionalization and dissolution of nitric acid treated single-walled carbon nanotubes.* Journal of the American Chemical Society, 2009. **131**(50): p. 18153-18158.
69. Ahmed, D.S., A.J. Haider, and M. Mohammad, *Comparesion of functionalization of multi-Walled carbon nanotubes treated by oil olive and nitric acid and their characterization.* Energy Procedia, 2013. **36**: p. 1111-1118.
70. Tchoul, M.N., et al., *Effect of mild nitric acid oxidation on dispersability, size, and structure of single-walled carbon nanotubes.* Chemistry of Materials, 2007. **19**(23): p. 5765-5772.
71. Datsyuk, V., et al., *Chemical oxidation of multiwalled carbon nanotubes.* Carbon, 2008. **46**(6): p. 833-840.
72. Kanai, Y., et al., *Atomistic oxidation mechanism of a carbon nanotube in nitric acid.* Physical Review Letters, 2010. **104**(6): p. 066401.
73. Zhang, H., et al., *Functionalization of multi-walled carbon nanotubes via surface unpaired electrons.* Nanotechnology, 2010. **21**(8): p. 085706.
74. Ngo, C.L., et al., *Surface modification and functionalization of carbon nanotube with some organic compounds.* Advances in Natural Sciences: Nanoscience and Nanotechnology, 2013. **4**(3): p. 035017.

75. Chusuei, C.C. and M. Wayu, *Characterizing functionalized carbon nanotubes for improved fabrication in aqueous solution environments*. 2011: INTECH Open Access Publisher.
76. Baykal, A., et al., *Acid functionalized multiwall carbon nanotube/magnetite (MWCNT)-COOH/*Fe_3O_4 *hybrid: synthesis, characterization and conductivity evaluation.* Journal of Inorganic and Organometallic Polymers and Materials, 2013. **23**(3): p. 726-735.
77. Scheibe, B., E. Borowiak-Palen, and R.J. Kalenczuk, *Oxidation and reduction of multiwalled carbon nanotubes—preparation and characterization.* Materials Characterization, 2010. **61**(2): p. 185-191.
78. Ngoy, J.M., et al., *Covalent functionalization for multi-walled carbon nanotube (f-MWCNT)-folic acid bound bioconjugate.* Journal of Applied Sciences, 2011. **11**(15): p. 2700-2711.
79. Shojaosadati, S., et al., *Effect of different CNT's oxidation methods on thiocoline detection by surfactant modified graphite electrodes.* International Journal of Nanoscience and Nanotechnology, 2010. **6**(4): p. 195-204.
80. Sánchez, A., et al., *Functionalization of carbon nanotubes and polymer compatibility studies.* Journal of Materials Science Research, 2014. **3**(1): p. 1.
81. Lin, T., et al., *Chemistry of carbon nanotubes.* Australian Journal of Chemistry, 2003. **56**(7): p. 635-651.
82. Atieh, M.A., et al., *Effect of carboxylic functional group functionalized on carbon nanotubes surface on the removal of lead from water.* Bioinorganic Chemistry and Applications, 2011. **2010**.
83. Griffiths, D.J. and R. College, *Introduction to electrodynamics*. Vol. 3. 1999: prentice Hall Upper Saddle River, NJ.
84. Tauxe, L., et al., *Essentials of Paleomagnetism, Third Web Edition*. 2014.
85. Stöhr, J. and H.C. Siegmann, *Magnetism.* Solid-State Sciences. Springer, Berlin, Heidelberg, 2006. **5**.
86. Dionne, G.F., *Magnetic oxides*. Vol. 14. 2009: Springer.
87. Stefanita, C.-G., *Magnetism: Basics and applications*. 2012: Springer Science & Business Media, .
88. Getzlaff, M., *Fundamentals of magnetism*. 2007: Springer Science & Business Media.
89. Goldman, A., *Modern ferrite technology*. 2006: Springer Science & Business Media.
90. Frenkel, J. and J. Dorfman, *Spontaneous and induced magnetisation in ferromagnetic bodies.* Nature, 1930. **126**(3173): p. 274-275.
91. Akbarzadeh, A., M. Samiei, and S. Davaran, *Magnetic nanoparticles: preparation, physical properties, and applications in biomedicine.* Nanoscale Research Letters, 2012. **7**(1): p. 1-13.
92. Bean, C. and J. Livingston, *Superparamagnetism.* Journal of Applied Physics, 1959. **30**(4): p. S120-S129.

93. Issa, B., et al., *Magnetic nanoparticles: surface effects and properties related to biomedicine applications.* International Journal of Molecular Sciences, 2013. **14**(11): p. 21266-21305.
94. Vatta, L.L., R.D. Sanderson, and K.R. Koch, *Magnetic nanoparticles: Properties and potential applications.* Pure and Applied Chemistry, 2006. **78**(9): p. 1793-1801.
95. Ghosh, S. and I.K. Puri, *Soft polymer magnetic nanocomposites: microstructure patterning by magnetophoretic transport and self-assembly.* Soft Matter, 2013. **9**(6): p. 2024-2029.
96. Ghosh, S., et al., *Patterning the stiffness of elastomeric nanocomposites by magnetophoretic control of cross-linking impeder distribution.* Materials, 2015. **8**(2): p. 474-485.
97. Jagannatham, M., S. Sankaran, and H. Prathap, *Electroless nickel plating of arc discharge synthesized carbon nanotubes for metal matrix composites.* Applied Surface Science, 2015. **324**: p. 475-481.
98. Velasco-Santos, C., A. Martinez-Hernandez, and V. Castano, *Carbon nanotube-polymer nanocomposites: The role of interfaces.* Composite Interfaces, 2005. **11**(8-9): p. 567-586.
99. Mahanthesha, P., C. Srinivasa, and G. Mohankumar, *Processing and characterization of carbon nanotubes decorated with pure electroless nickel and their magnetic properties.* Procedia Materials Science, 2014. **5**: p. 883-890.
100. Liebau, M., et al., *Contact improvement of carbon nanotubes via electroless nickel deposition.* Applied Physics A, 2003. **77**(6): p. 731-734.
101. Gong, J.-L., et al., *Removal of cationic dyes from aqueous solution using magnetic multi-wall carbon nanotube nanocomposite as adsorbent.* Journal of Hazardous Materials, 2009. **164**(2): p. 1517-1522.
102. Fazelirad, H., et al., *Preparation of magnetic multi-walled carbon nanotubes for an efficient adsorption and spectrophotometric determination of amoxicillin.* Journal of Industrial and Engineering Chemistry, 2015. **21**: p. 889-892.
103. Tarigh, G.D. and F. Shemirani, *Magnetic multi-wall carbon nanotube nanocomposite as an adsorbent for preconcentration and determination of lead (II) and manganese (II) in various matrices.* Talanta, 2013. **115**: p. 744-750.
104. Chen, C., et al., *Functionalization and magnetization of carbon nanotubes using Co-60 gamma-ray irradiation.* Journal of Magnetism and Magnetic Materials, 2014. **367**: p. 47-52.
105. Huang, Y., et al., *Optimization and evaluation of chelerythrine nanoparticles composed of magnetic multiwalled carbon nanotubes by response surface methodology.* Applied Surface Science, 2014. **292**: p. 378-386.
106. Wang, Z., et al., *Magnetite nanocrystals on multiwalled carbon nanotubes as a synergistic microwave absorber.* The Journal of Physical Chemistry C, 2013. **117**(10): p. 5446-5452.
107. Ghasemi, A., et al., *Enhanced reflection loss characteristics of substituted barium ferrite/functionalized multi-walled carbon nanotube nanocomposites.* Journal of Applied Physics, 2011. **109**(7): p. 07A507.

108. Sarkar, D., et al., *Enhanced broadband microwave reflection loss of carbon nanotube ensheathed Ni–Zn–Co-ferrite magnetic nanoparticles.* Materials Letters, 2014. **120**: p. 259-262.
109. Weissker, U., et al., *Carbon nanotubes filled with ferromagnetic materials.* Materials, 2010. **3**(8): p. 4387-4427.
110. Sameera, I., R. Bhatia, and V. Prasad, *Characterization and magnetic response of multiwall carbon nanotubes filled with iron nanoparticles of different aspect ratios.* Physica E: Low-dimensional Systems and Nanostructures, 2013. **52**: p. 1-7.
111. Hayashi, Y., et al., *Growth and nanoscale magnetic properties of ferromagnetic nanowire encapsulated inside carbon nanotubes.* Magnetics, IEEE Transactions on, 2009. **45**(6): p. 2488-2491.
112. Wang, S.-F., et al., *Magnetic and electronic properties of a single iron atomic chain encapsulated in carbon nanotubes: A first-principles study.* Journal of Molecular Structure: THEOCHEM, 2010. **962**(1): p. 108-112.
113. Kaneko, T., et al., *Magnetic property of FePt nanoparticles encaged in carbon nanotubes.* Vacuum, 2013. **87**: p. 187-190.
114. Masotti, A. and A. Caporali, *Preparation of magnetic carbon nanotubes (Mag-CNTs) for biomedical and biotechnological applications.* International Journal of Molecular Sciences, 2013. **14**(12): p. 24619-24642.
115. John, A.R. and P. Arumugam, *Studies on structural and magnetic properties of pristine and nickel-filled carbon nanotubes synthesized using LaNi 5 alloy particles as a catalyst.* Chemical Engineering Journal, 2014. **243**: p. 436-447.
116. Munoz-Sandoval, E., et al., *Synthesis, characterization and magnetic properties of Co@ Au core-shell nanoparticles encapsulated by nitrogen-doped multiwall carbon nanotubes.* Carbon, 2014. **77**: p. 722-737.
117. Qi, X., et al., *Controllable synthesis, characterization, and magnetic properties of magnetic nanoparticles encapsulated in carbon nanocages and carbon nanotubes.* Diamond and Related Materials, 2014. **45**: p. 12-19.
118. Korneva, G., et al., *Carbon nanotubes loaded with magnetic particles.* Nano Letters, 2005. **5**(5): p. 879-884.
119. Kopyl, S., et al., *Filling carbon nanotubes with magnetic particles.* Journal of Materials Chemistry C, 2013. **1**(16): p. 2860-2866.
120. Kopyl, S., et al., *FMR study of carbon nanotubes filled with* Fe_3O_4 *nanoparticles.* Journal of Magnetism and Magnetic Materials, 2014. **358**: p. 44-49.
121. Demir, A., et al., *Low temperature magnetic investigation of* Fe_3O_4 *nanoparticles filled into multiwalled carbon nanotubes.* Synthetic Metals, 2014. **187**: p. 75-80.
122. Kim, K., et al., *Formation and surface modification of* Fe_3O_4 *nanoparticles by co-precipitation and sol-gel method.* Journal of Industrial and Engineering Chemistry-Seoul, 2007. **13**(7): p. 1137.
123. Fun Chin, S. and K. Swaminathan Iyer, *Fabrication of carbon nano-tubes decorated with ultra fine superparamagnetic nano-particles under continuous flow conditions.* Lab on a Chip, 2008. **8**(3): p. 439-442.
124. Yan, L., et al., *Characterization of magnetic guar gum-grafted carbon nanotubes and the adsorption of the dyes.* Carbohydrate Polymers, 2012. **87**(3): p. 1919-1924.

125. Xiao, D., et al., *Development of novel molecularly imprinted magnetic solid-phase extraction materials based on magnetic carbon nanotubes and their application for the determination of gatifloxacin in serum samples coupled with high performance liquid chromatography.* Journal of Chromatography A, 2013. **1274**: p. 44-53.
126. Yu, P., et al., *Polyethylene glycol modified magnetic carbon nanotubes as nanosorbents for the determination of methylprednisolone in rat plasma by high performance liquid chromatography*. Journal of Chromatography A, 2014. **1348**: p. 27-33.
127. Sowichai, K., et al., *Facile method to prepare magnetic multi-walled carbon nanotubes by in situ co-precipitation route.* Journal of Industrial and Engineering Chemistry, 2012. **18**(5): p. 1568-1571.
128. Zarei, H., et al., *Magnetic nanocomposite of anti-human IgG/COOH–multiwalled carbon nanotubes/*Fe_3O_4 *as a platform for electrochemical immunoassay.* Analytical Biochemistry, 2012. **421**(2): p. 446-453.
129. Romero, V., et al., *In situ ultrasound-assisted synthesis of* Fe_3O_4 *nanoparticles with simultaneous ion co-precipitation for multielemental analysis of natural waters by total reflection X-ray fluorescence spectrometry*. Journal of Analytical Atomic Spectrometry, 2013. **28**(6): p. 923-933.
130. Mendoza-Bello, S., et al., *Size-controlled synthesis of* Fe_2O_3 *and* Fe_3O_4 *nanoparticles onto zeolite by means of a modified activated-coprecipitation method: effect of the HCl concentration during the activation.* Journal of Nanoparticle Research, 2012. **14**(11): p. 1-9.
131. Mascolo, M.C., Y. Pei, and T.A. Ring, *Room temperature co-precipitation synthesis of magnetite nanoparticles in a large pH window with different bases.* Materials, 2013. **6**(12): p. 5549-5567.
132. Wei, Y., et al., *Synthesis of* Fe_3O_4 *nanoparticles and their magnetic properties.* Procedia Engineering, 2012. **27**: p. 632-637.
133. Wu, S., et al., Fe_3O_4 *magnetic nanoparticles synthesis from tailings by ultrasonic chemical co-precipitation.* Materials Letters, 2011. **65**(12): p. 1882-1884.
134. Kim, I.T. and R. Tannenbaum, *Magnetic carbon nanotubes: Synthesis, characterization, and anisotropic electrical properties*. 2011: INTECH Open Access Publisher.
135. Zhao, W., et al., *Magnetic nanoparticles decorated multi-walled carbon nanotubes by bio-inspired poly (dopamine) surface functionalization.* Synthetic Metals, 2013. **169**: p. 59-63.
136. Zhang, Q., et al., *Synthesis and characterization of carbon nanotubes decorated with manganese–zinc ferrite nanospheres.* Materials Chemistry and Physics, 2009. **116**(2): p. 658-662.
137. Ali, S.D., S.T. Hussain, and S.R. Gilani, *Synthesis, characterization and magnetic properties of carbon nanotubes decorated with magnetic* $M_{II}Fe_2O_4$ *nanoparticles.* Applied Surface Science, 2013. **271**: p. 118-124.
138. Gabal, M., et al., *MWCNTs decorated* $Mn_{0.8}Zn_{0.2}Fe_2O_4$ *:Synthesis, characterization and compositional effect on the structural and magnetic properties.* Journal of Magnetism and Magnetic Materials, 2015. **374**: p. 230-237.

139. Bittencourt, C., et al., *Decorating carbon nanotubes with nickel nanoparticles.* Chemical Physics Letters, 2007. **436**(4): p. 368-372.
140. Li, Q., et al., *Coating of carbon nanotube with nickel by electroless plating method.* Japanese Journal of Applied Physics Part 2 Letters, 1997. **36**: p. L501-L503.
141. Bak, S.-M., et al., *Mesoporous nickel/carbon nanotube hybrid material prepared by electroless deposition.* Journal of Materials Chemistry, 2011. **21**(6): p. 1984-1990.
142. Ellis, A., et al., *Magnetic properties of electroless nickel-phosphorus coated multi-walled carbon nanotubes.* Carbon-Science and Technology, 2008. **1**(1): p. 13-18.
143. Singh, N.B., B. Bhattacharya, and U. Sarkar, *Nickel decorated single-wall carbon nanotube as CO Sensor.* Soft Nanoscience Letters, 2013. **3**(04): p. 9.
144. Arai, S., et al., *Pure-nickel-coated multiwalled carbon nanotubes prepared by electroless deposition.* Electrochemical and Solid-State Letters, 2010. **13**(12): p. D94-D96.
145. Dobrzański, L., et al., *Synthesis and characterization of carbon nanotubes decorated with platinum nanoparticles.* Journal of Achievements in Materials and Manufacturing Engineering, 2010. **39**(2): p. 184-189.
146. Choi, W.-K., et al., *Electromagnetic interference shielding effectiveness of electroless nickel-plated MWCNTs/CFs-reinforced HDPE matrix composites.* Bull. Korean Chem. Soc, 2014. **35**(2): p. 597.
147. Arai, S., et al., *Nickel-coated carbon nanofibers prepared by electroless deposition.* Electrochemistry Communications, 2004. **6**(10): p. 1029-1031.
148. Schlesinger, M., *Electroless deposition of nickel.* Modern Electroplating, 2000. **4**: p. 667-684.
149. Wang, F., S. Arai, and M. Endo, *The preparation of multi-walled carbon nanotubes with a Ni–P coating by an electroless deposition process.* Carbon, 2005. **43**(8): p. 1716-1721.
150. Mallory, G.O. and J.B. Hajdu, *Electroless plating: fundamentals and applications*. 1990: William Andrew, .
151. Sarojini, K.K., et al., *Electrical conductivity of ceramic and metallic nanofluids.* Colloids and Surfaces A: Physicochemical and Engineering Aspects, 2013. **417**: p. 39-46.
152. Wang, J., et al., *Heat transfer and pressure drop of nanofluids containing carbon nanotubes in laminar flows.* Experimental Thermal and Fluid Science, 2013. **44**: p. 716-721.
153. Wan, M., et al., *Temperature dependent heat transfer performance of multi-walled carbon nanotube-based aqueous nanofluids at very low particle loadings.* Johnson Matthey Technology Review, 2015. **59**(3): p. 199-206.
154. Glover, B., et al., *Effective electrical conductivity of functional single-wall carbon nanotubes in aqueous fluids.* Synthetic Metals, 2008. **158**(12): p. 506-508.
155. Salazar, P.F., et al., *Enhanced electrical conductivity of imidazolium-based ionic liquids mixed with carbon nanotubes: a spectroscopic study*. Journal of The Electrochemical Society, 2014. **161**(9): p. H481-H486.

156. Xue, Q.-Z., *Model for effective thermal conductivity of nanofluids.* Physics Letters A, 2003. **307**(5): p. 313-317.
157. Strauss, M.T. and R.L. Pober, *Nanotubes in liquids: Effective thermal conductivity.* Journal of Applied Physics, 2006. **100**(8): p. 084328.
158. Vaisman, L., H.D. Wagner, and G. Marom, *The role of surfactants in dispersion of carbon nanotubes.* Advances in Colloid and Interface Science, 2006. **128**: p. 37-46.
159. Sadri, R., et al., *An experimental study on thermal conductivity and viscosity of nanofluids containing carbon nanotubes.* Nanoscale Research Letters, 2014. **9**(1): p. 1-16.
160. Eapen, J., et al., *The classical nature of thermal conduction in nanofluids.* Journal of Heat Transfer, 2010. **132**(10): p. 102402.
161. Kraynov, A. and T.E. Müller, *Concepts for the stabilization of metal nanoparticles in ionic liquids*. 2011: INTECH Open Access Publisher.
162. Berger, P., et al., *Preparation and properties of an aqueous ferrofluid.* Journal of Chemical Education, 1999. **76**(7): p. 943.
163. Fonseca, M.A., et al., *Carbon nanotubes in a fluidic medium: Critical analysis*. 2013: INTECH Open Access Publisher.
164. Hilding, J., et al., *Dispersion of carbon nanotubes in liquids.* Journal of Dispersion Science and Technology, 2003. **24**(1): p. 1-41.
165. Scherer, C. and A.M. Figueiredo Neto, *Ferrofluids: properties and applications.* Brazilian Journal of Physics, 2005. **35**(3A): p. 718-727.
166. Mehta, R. and R. Upadhyay, *Science and technology of ferrofluids.* Current Science, 1999. **76**(3): p. 305-312.
167. Samouhos, S. and G. McKinley, *Carbon nanotube–magnetite composites, with applications to developing unique magnetorheological fluids.* Journal of Fluids Engineering, 2007. **129**(4): p. 429-437.
168. Moaseri, E., et al., *Improvements in mechanical properties of multi-walled carbon nanotube-reinforced epoxy composites through novel magnetic-assisted method for alignment of carbon nanotubes.* Composites Part A: Applied Science and Manufacturing, 2014. **64**: p. 228-233.
169. Cadek, M., et al., *Morphological and mechanical properties of carbon-nanotube-reinforced semicrystalline and amorphous polymer composites.* Applied Physics Letters, 2002. **81**(27): p. 5123-5125.
170. Biercuk, M., et al., *Carbon nanotube composites for thermal management.* Applied Physics Letters, 2002. **80**(15): p. 2767-2769.
171. Choi, E., et al., *Enhancement of thermal and electrical properties of carbon nanotube polymer composites by magnetic field processing.* Journal of Applied physics, 2003. **94**(9): p. 6034-6039.
172. Correa-Duarte, M.A., et al., *Alignment of carbon nanotubes under low magnetic fields through attachment of magnetic nanoparticles.* The Journal of Physical Chemistry B, 2005. **109**(41): p. 19060-19063.
173. Park, C., et al., *Aligned single-wall carbon nanotube polymer composites using an electric field.* Journal of Polymer Science Part B: Polymer Physics, 2006. **44**(12): p. 1751-1762.

174. Kim, I.T., A. Tannenbaum, and R. Tannenbaum, *Anisotropic conductivity of magnetic carbon nanotubes embedded in epoxy matrices.* Carbon, 2011. **49**(1): p. 54-61.
175. Sathyanarayana, S. and C. Hübner, *Thermoplastic nanocomposites with carbon nanotubes*, in *Structural Nanocomposites*. 2013, Springer. p. 19-60.
176. Das, A., et al., *Magnetite (Fe3O4)-filled carbon nanofibers as electro-conducting/superparamagnetic nanohybrids and their multifunctional polymer composites.* Journal of Nanoparticle Research, 2015. **17**(1): p. 1-14.
177. Song, W., et al., *The decoration of multi-walled carbon nanotubes with metal nanoparticles of uniform size using MeV electron beam irradiation.* Carbon, 2011. **49**(5): p. 1692-1698.
178. Li, X., et al., *Effect of sensitizing and activating pretreatment on the electroless plated MWCNTS*, in *International Conference on Composite Materials*. 2011: Jeju Island, Korea.
179. Pistone, A., et al., *Synthesis and magnetic properties of multiwalled carbon nanotubes decorated with magnetite nanoparticles.* Physica B: Condensed Matter, 2014. **435**: p. 88-91.
180. Chin, S.F., K.S. Iyer, and C.L. Raston, *Fabrication of carbon nano-tubes decorated with ultra fine superparamagnetic nano-particles under continuous flow conditions.* Lab on a Chip, 2008. **8**(3): p. 439-442.
181. He, H. and C. Gao, *Synthesis of Fe 3 O 4/Pt nanoparticles decorated carbon nanotubes and their use as magnetically recyclable catalysts.* Journal of Nanomaterials, 2011. **2011**: p. 11.
182. Maciejewska, B., et al., *Experimental and theoretical studies on the mechanism for chemical oxidation of multiwalled carbon nanotubes.* RSC Advances, 2014. **4**(55): p. 28826-28831.
183. Tserpes, K.I. and N. Silvestre, *Modeling of carbon nanotubes, graphene and their composites*. 2014: Springer.
184. Shan, Y., et al., *Preparation and characterization of biocompatible magnetic carbon nanotubes.* Applied Surface Science, 2010. **257**(2): p. 362-366.
185. Mitróová, Z., et al., *Preparation and characterization of carbon nanotubes functionalized by magnetite nanoparticles.* Olomouc, Czech Republic, EU, 2010. **10**: p. 12-14.
186. Chang, P.R., et al., *Characterization of magnetic soluble starch-functionalized carbon nanotubes and its application for the adsorption of the dyes.* Journal of Hazardous Materials, 2011. **186**(2): p. 2144-2150.
187. Karaagac, O., et al., *A simple way to synthesize superparamagnetic iron oxide nanoparticles in air atmosphere: iron ion concentration effect.* Magnetics, IEEE Transactions on, 2010. **46**(12): p. 3978-3983.
188. Maity, D. and D. Agrawal, *Synthesis of iron oxide nanoparticles under oxidizing environment and their stabilization in aqueous and non-aqueous media.* Journal of Magnetism and Magnetic Materials, 2007. **308**(1): p. 46-55.
189. Lopez, J.A., et al., *Synthesis and characterization of* Fe_3O_4 *magnetic nanofluid.* Revista Latinoamericana de Metalurgia y Materiales, 2010: p. 60-66.

190. Mozaffari, M., J. Amighian, and R. Tavakoli, *The effect of yttrium substitution on the magnetic properties of magnetite nanoparticles.* Journal of Magnetism and Magnetic Materials, 2015. **379**: p. 208-212.
191. Murakami, K., *The characteristics of ferrite cores with low Curie temperature and their application.* Magnetics, IEEE Transactions on, 1965. **1**(2): p. 96-100.
192. Rezlescu, N. and E. Cuciureanu, *Cation distribution and Curie temperature in some ferrites containing copper and manganese.* Physica Status Solidi (a), 1970. **3**(4): p. 873-878.
193. Arulmurugan, R., et al., *Mn–Zn ferrite nanoparticles for ferrofluid preparation: Study on thermal–magnetic properties.* Journal of Magnetism and Magnetic Materials, 2006. **298**(2): p. 83-94.
194. Auzans, E., et al., *Synthesis and properties of Mn-Zn ferrite ferrofluids.* Journal of Materials Science, 1999. **34**(6): p. 1253-1260.
195. Jeong, J.R., et al., *Magnetic properties of γ-Fe2O3 nanoparticles made by coprecipitation method.* physica status solidi (b), 2004. **241**(7): p. 1593-1596.
196. Aliahmad, M. and N. Nasiri Moghaddam, *Synthesis of maghemite (γ-Fe2O3) nanoparticles by thermal-decomposition of magnetite (Fe3O4) nanoparticles.* Materials Science-Poland, 2013. **31**(2): p. 264-268.
197. Tartaj, P., et al., *The preparation of magnetic nanoparticles for applications in biomedicine.* Journal of Physics D: Applied Physics, 2003. **36**(13): p. R182.
198. Kappiyoor, R., et al., *The effects of magnetic nanoparticle properties on magnetic fluid hyperthermia.* Journal of Applied Physics, 2010. **108**(9): p. 094702.
199. Ghosh, S. and I.K. Puri, *Changing the magnetic properties of microstructure by directing the self-assembly of superparamagnetic nanoparticles.* Faraday discussions, 2015. **181**: p. 423-435.
200. Mørup, S., *Superferromagnetic nanostructures.* Hyperfine Interactions, 1994. **90**(1): p. 171-185.
201. Subhankar, B. and K. Wolfgang, *Supermagnetism.* J. Phys. D, 2009. **42**: p. 013001.
202. Lee, S.-J., et al., *Synthesis and characterization of superparamagnetic maghemite nanoparticles prepared by coprecipitation technique.* Journal of Magnetism and Magnetic Materials, 2004. **282**: p. 147-150.
203. Millan, A., et al., *Surface effects in maghemite nanoparticles.* Journal of magnetism and magnetic materials, 2007. **312**(1): p. L5-L9.
204. Racuciu, M., D. Creanga, and G. Calugaru, *Synthesis and rheological properties of an aqueous ferrofluid.* Journal of Optoelectronics and Advanced Materials, 2005. **7**(6): p. 2859-2864.
205. Liu, Y., et al., *Attachment of magnetic nanoparticles on carbon nanotubes using oleate as an interlinker molecule.* Materials Chemistry and Physics, 2009. **116**(2): p. 438-441.
206. Caneba, G., et al., *Novel ultrasonic dispersion of carbon nanotubes.* Journal of Minerals and Materials Characterization and Engineering, 2010. **9**(03): p. 165.
207. Othman, S.H., et al., *Dispersion and stabilization of photocatalytic* TiO_2 *nanoparticles in aqueous suspension for coatings applications.* Journal of Nanomaterials, 2012. **2012**: p. 2.

208. Baykal, A., et al., *Acid Functionalized Multiwall Carbon Nanotube/Magnetite (MWCNT)-COOH/Fe3O4 Hybrid: Synthesis, Characterization and Conductivity Evaluation.* Journal of Inorganic and Organometallic Polymers and Materials, 2013. **23**(3): p. 726-35.
209. Ganguly, R., A.P. Gaind, and I.K. Puri, *A strategy for the assembly of three-dimensional mesoscopic structures using a ferrofluid.* Physics of Fluids, 2005. **17**(5).
210. Ganguly, R., et al., *Analyzing ferrofluid transport for magnetic drug targeting.* Journal of Magnetism and Magnetic Materials, 2005. **289**: p. 331-334.
211. Ganguly, R., B. Zellmer, and I.K. Puri, *Field-induced self-assembled ferrofluid aggregation in pulsatile flow.* Physics of Fluids, 2005. **17**: p. 097104.
212. Roy, T., et al., *Magnetic microsphere-based mixers for microdroplets.* Physics of Fluids, 2009. **21**: p. 027101.
213. Ganguly, R. and I.K. Puri, *Field-assisted self-assembly of superparamagnetic nanoparticles for biomedical, MEMS and BioMEMS applications.* Advances in Applied Mechanics, 2007. **41**: p. 293-335.
214. Ganguly, R. and I.K. Puri, *Microfluidic transport in magnetic MEMS and bioMEMS.* Wiley Interdisciplinary Reviews: Nanomedicine and Nanobiotechnology, 2010. **2**(4): p. 382-399.
215. Puri, I.K. and R. Ganguly, *Particle transport in therapeutic magnetic fields.* Annual Review of Fluid Mechanics, 2014. **46**(1): p. 407-440.
216. Rosensweig, R.E., *Ferrohydrodynamics*. 1997: Dover Publications.
217. Massart, R., *Preparation of aqueous magnetic liquids in alkaline and acidic media.* IEEE Transactions on Magnetics 1981. **17**(2): p. 1247-1248.
218. Massart, R., et al., *Preparation and properties of monodisperse magnetic fluids.* Journal of Magnetism and Magnetic Materials, 1995. **149**(1): p. 1-5.
219. Voit, W., et al. *Magnetic behavior of coated superparamagnetic iron oxide nanoparticles in ferrofluids*. in *MRS Proceedings*. 2001. Cambridge Univ Press.
220. Fattah, A.R.A., S. Ghosh, and I.K. Puri, *Printing microstructures in a polymer matrix using a ferrofluid droplet.* Journal of Magnetism and Magnetic Materials, 2016. **401**: p. 1054-1059.
221. Karthik, P. and S.P. Singh, *Conductive silver inks and their applications in printed and flexible electronics.* RSC Advances, 2015. **5**(95): p. 77760-77790.
222. Kamyshny, A. and S. Magdassi, *Conductive nanomaterials for printed electronics.* Small, 2014. **10**(17): p. 3515-3535.
223. Kolosovas-Machuca, E.S., et al., *Resistance-based biosensor of Multi-Walled Carbon Nanotubes.* J Immunoassay Immunochem, 2015. **36**(2): p. 142-8.
224. Soleymani, L., et al., *Nanostructuring of patterned microelectrodes to enhance the sensitivity of electrochemical nucleic acids detection.* Angewandte Chemie International Edition, 2009. **48**(45): p. 8457-8460.
225. Alubaidy, M., et al., *Femtosecond laser nanostructuring for femtosensitive DNA detection.* Biosensors and bioelectronics, 2012. **33**(1): p. 82-87.
226. Balasubramanian, K. and M. Burghard, *Biosensors based on carbon nanotubes.* Anal Bioanal Chem, 2006. **385**(3): p. 452-68.

227. Chao Li, et al., *Complementary Detection of Prostate-Specific Antigen Using In2O3 Nanowires and Carbon Nanotubes.* J. Am. Chem. Soc., 2005. **127**: p. 12484-85.
228. Chen, R.J., et al., *Noncovalent functionalization of carbon nanotubes for highly specific electronic biosensors.* Proc Natl Acad Sci U S A, 2003. **100**(9): p. 4984-9.
229. Cid, C.C., et al., *Carbon nanotube field effect transistors for the fast and selective detection of human immunoglobulin G.* Analyst, 2008. **133**(8): p. 1005-8.
230. Liu, Z., et al., *Polyaniline-coated Fe3O4 nanoparticle-carbon-nanotube composite and its application in electrochemical biosensing.* Small, 2008. **4**(4): p. 462-6.
231. Pozuelo, M., et al., *Paper-based chemiresistor for detection of ultralow concentrations of protein.* Biosens Bioelectron, 2013. **49**: p. 462-5.
232. Abdel Fattah, A.R., et al., *Nickel Nanoparticles Entangled in Carbon Nanotubes: Novel Ink for Nanotube Printing.* ACS Appl. Mater. & Interfaces, 2016. **8**(3): p. 1589-93.
233. Masotti, A. and A. Caporali, *Preparation of magnetic carbon nanotubes (Mag-CNTs) for biomedical and biotechnological applications.* Int J Mol Sci, 2013. **14**(12): p. 24619-42.
234. Balasubramanian, K. and M. Burghard, *Chemically functionalized carbon nanotubes.* Small, 2005. **1**(2): p. 180-92.
235. Korneva, G., et al., *Carbon nanotubes loaded with magnetic particles.* Nano Lett, 2005. **5**(5): p. 879-84.
236. He, H. and C. Gao, *Synthesis of Fe3O4/Pt Nanoparticles Decorated Carbon Nanotubes and Their Use as Magnetically Recyclable Catalysts.* Journal of Nanomaterials, 2011. **2011**: p. 1-10.
237. Abdel Fattah, A.R., S. Ghosh, and I.K. Puri, *Printing Microstructures in a Polymer Matrix using a Ferrofluid Droplet* J. Mag. Mag. Mater., 2016. **401**: p. 1054-1059.
238. Ganguly, R. and I.K. Puri, *Field-assisted self-assembly of superparamagnetic nanoparticles for biomedical, MEMS and BioMEMS applications.* Adv. in Appl. Mech., 2007. **41**: p. 293-335.
239. Ganguly, R. and I.K. Puri, *Microfluidic transport in magnetic MEMS and bioMEMS.* Wiley Interdisciplinary Rev.: Nanomed. and Nanobiotech., 2010. **2**: p. 382-399.
240. Abdel Fattah, A.R., S. Ghosh, and I.K. Puri, *Printing three-dimensional heterogeneities in the elastic modulus of an elastomeric matrix.* ACS Appl Mater Interfaces, 2016.
241. Tsai, P.J., et al., *Tailoring Material Stiffness by Filler Particle Organization.* ACS Applied Materials & Interfaces, 2016. **8**(41): p. 27449-27453.
242. Qu, S., et al., *Magnetic loading of carbon nanotube/nano-Fe(3)O(4) composite for electrochemical sensing.* Talanta, 2007. **71**(3): p. 1096-102.
243. Pérez-López, B. and A. Merkoçi, *Magnetic Nanoparticles Modified with Carbon Nanotubes for Electrocatalytic Magnetoswitchable Biosensing Applications.* Advanced Functional Materials, 2011. **21**(2): p. 255-260.
244. Zarei, H., et al., *Magnetic nanocomposite of anti-human IgG/COOH-multiwalled carbon nanotubes/Fe(3)O(4) as a platform for electrochemical immunoassay.* Anal Biochem, 2012. **421**(2): p. 446-53.

245. Hernández, J. and I.M. Thompson, *Prostate-specific antigen: a review of the validation of the most commonly used cancer biomarker.* Cancer, 2004. **101**(5): p. 894-904.
246. Fürstenberger, G. and H.-J. Senn, *Insulin-like growth factors and cancer.* The lancet oncology, 2002. **3**(5): p. 298-302.
247. Engel, R.H. and V.G. Kaklamani, *HER2-positive breast cancer.* Drugs, 2007. **67**(9): p. 1329-1341.
248. Chen, B.J., et al., *Small molecules targeting c-Myc oncogene: promising anti-cancer therapeutics.* Int J Biol Sci, 2014. **10**(10): p. 1084-96.
249. Dang, C.V., *MYC on the path to cancer.* Cell, 2012. **149**(1): p. 22-35.
250. D J Liao and R.B. Dickson, *c-Myc in breast cancer.* Endocrine-Related Cancer, 2000. **7**: p. 143-164.
251. Yang, M., Y. Kostov, and A. Rasooly, *Carbon nanotubes based optical immunodetection of Staphylococcal Enterotoxin B (SEB) in food.* Int J Food Microbiol, 2008. **127**(1-2): p. 78-83.
252. Mirhosseini, H., et al., *Effect of Arabic gum, xanthan gum and orange oil contents on ζ-potential, conductivity, stability, size index and pH of orange beverage emulsion.* Colloids and Surfaces A: Physicochemical and Engineering Aspects, 2008. **315**(1): p. 47-56.
253. Ostolska, I. and M. Wiśniewska, *Application of the zeta potential measurements to explanation of colloidal* Cr_2O_3 *stability mechanism in the presence of the ionic polyamino acids.* Colloid and Polymer Science, 2014. **292**(10): p. 2453-2464.
254. Abdalla, A.M., S. Ghosh, and I.K. Puri, *Decorating carbon nanotubes with co-precipitated magnetite nanocrystals.* Diamond and Related Materials, 2016.
255. Stefansson, S., H.H. Kwon, and S.N. Ahn, *Targeting Antibodies to Carbon Nanotube Field Effect Transistors by Pyrene Hydrazide Modification of Heavy Chain Carbohydrates.* Journal of Nanotechnology, 2012. **2012**: p. 1-8.
256. Patolsky, F., Y. Weizmann, and I. Willner, *Long-range electrical contacting of redox enzymes by SWCNT connectors.* Angew Chem Int Ed Engl, 2004. **43**(16): p. 2113-7.
257. Zhang, X., et al., *Electronic Detection of Escherichia coli O157：H7 Using Single-Walled Carbon Nanotubes Field-Effect Transistor Biosensor.* Engineering, 2012. **04**(10): p. 94-98.
258. Salehi-Khojin, A., et al., *Sensitivity of nanotube chemical sensors at the onset of Poole–Frenkel conduction.* Applied Physics Letters, 2010. **96**(16): p. 163110.
259. Amin Salehi-Khojin, et al., *On the Sensing Mechanism in Carbon Nanotube Chemiresistors.* ACS Nano, 2010. **5**: p. 153-158.
260. Li, W., et al., *The microstructure of Ni layer on single-walled carbon nanotubes prepared by an electroless coating process.* Journal of Nanomaterials, 2011. **2011**: p. 13.
261. Agarwala, R. and V. Agarwala, *Electroless alloy/composite coatings: A review.* Sadhana, 2003. **28**(3-4): p. 475-493.

262. Ang, L.-M., et al., *Electroless plating of metals onto carbon nanotubes activated by a single-step activation method.* Chemistry of Materials, 1999. **11**(8): p. 2115-2118.
263. Yung, K., J. Wei, and B. Tay, *Electroless plating of nickel on carbon nanotubes film*, in *Electronic Packaging Technology Conference*. 2005, IEEE: Singapore. p. 636-638.
264. Wang, F., et al., *Synthesis of carbon nanotube-supported nickel–phosphorus nanoparticles by an electroless process.* Carbon, 2006. **44**(7): p. 1307-1310.
265. Van Gestel, T., et al., *Manufacturing of new nano-structured ceramic–metallic composite microporous membranes consisting of ZrO 2, Al 2 O 3, TiO 2 and stainless steel.* Solid State Ionics, 2008. **179**(27): p. 1360-1366.
266. Jie, G., et al., *Preparation and characterization of carboxyl multi-walled carbon nanotubes/calcium alginate composite hydrogel nano-filtration membrane.* Materials Letters, 2015. **157**: p. 112-115.
267. Jang, J.H., et al., *Correlation between particle deposition and the size ratio of particles to patterns in nano-and micro-patterned membrane filtration systems.* Separation and Purification Technology, 2015. **156**: p. 608-616.
268. Abdel Fattah, A.R., S. Ghosh, and I.K. Puri, *Printing three-dimensional heterogeneities in the elastic modulus of an elastomeric matrix.* ACS Applied Materials & Interfaces, 2016. **8**(17): p. 11018-11023.
269. He, X., et al., *Size dependence of the magnetic properties of Ni nanoparticles prepared by thermal decomposition method.* Nanoscale Research Letters, 2013. **8**(1): p. 446.
270. Kolhatkar, A.G., et al., *Tuning the magnetic properties of nanoparticles.* International Journal of Molecular Sciences, 2013. **14**(8): p. 15977-16009.
271. Belcher, A.M., et al., *Control of crystal phase switching and orientation by soluble mollusc-shell proteins.* Nature, 1996. **381**: p. 56-58.
272. Combes, S.A., *Materials, structure, and dynamics of insect wings as bioinspiration for MAVs.* Encyclopedia of aerospace engineering, 2010.
273. Esposito, C.J., et al., *A robotic fish caudal fin: effects of stiffness and motor program on locomotor performance.* Journal of Experimental Biology, 2012. **215**(1): p. 56-67.
274. Pozegic, T., et al., *Multi-functional carbon fibre composites using carbon nanotubes as an alternative to polymer sizing.* Scientific Reports, 2016. **6**.
275. Ma, C., Y. Wang, and Y. Yu, *Electrical and thermal properties of carbon nanotubes/PMMA composites induced by low magnetic fields.* Plastics, Rubber and Composites, 2010. **39**(2): p. 49-53.
276. Abdalla, A.M., et al., *Nickel oxide nanotubes synthesis using multiwalled carbon nanotubes as sacrificial templates for supercapacitor application.* Nanotechnology, 2016.
277. Liu, C., et al., *Advanced materials for energy storage.* Advanced Materials, 2010. **22**(8): p. E28–E62.
278. Dai, W., et al., *Electrochemical imprinted polycrystalline nickel–nickel oxide half-nanotube-modified boron-doped diamond electrode for the detection of l-serine.* ACS Applied Materials & Interfaces, 2015. **7**(41): p. 22858-22867.

279. Li, X.-H., et al., *An electrokinetic route to rapid synthesis of nickel hydroxide and nickel oxide nanotubes.* Journal of Nanoscience and Nanotechnology, 2010. **10**(8): p. 5191-5195.
280. Conway, B.E., *Electrochemical supercapacitors: scientific fundamentals and technological applications*. 2013, New York: Springer Science & Business Media.
281. Kötz, R. and M. Carlen, *Principles and applications of electrochemical capacitors.* Electrochimica Acta, 2000. **45**(15): p. 2483-2498.
282. Lokhande, C., D. Dubal, and O.-S. Joo, *Metal oxide thin film based supercapacitors.* Current Applied Physics, 2011. **11**(3): p. 255-270.
283. Cheng, M.-Y., et al., *Size effect of nickel oxide for lithium ion battery anode.* Journal of Power Sources, 2014. **253**: p. 27-34.
284. Yan, X., et al., *Synthesis of hollow nickel oxide nanotubes by electrospinning with structurally enhanced lithium storage properties.* Materials Letters, 2014. **136**: p. 74-77.
285. Sattarahmady, N., H. Heli, and F. Faramarzi, *Nickel oxide nanotubes-carbon microparticles/Nafion nanocomposite for the electrooxidation and sensitive detection of metformin.* Talanta, 2010. **82**(4): p. 1126-1135.
286. Pang, H., et al., *Facile synthesis of nickel oxide nanotubes and their antibacterial, electrochemical and magnetic properties.* Chemical Communications, 2009(48): p. 7542-7544.
287. Rai, A.K., et al., *Electrochemical study of NiO nanoparticles electrode for application in rechargeable lithium-ion batteries.* Ceramics International, 2013. **39**(6): p. 6611-6618.
288. Sk, M.M., et al., *Review on advances in porous nanostructured nickel oxides and their composite electrodes for high-performance supercapacitors.* Journal of Power Sources, 2016. **308**: p. 121-140.
289. Feng, L., et al., *Recent progress in nickel based materials for high performance pseudocapacitor electrodes.* Journal of Power Sources, 2014. **267**: p. 430-444.
290. Jacob, G.M. and I. Zhitomirsky, *Microstructure and properties of manganese dioxide films prepared by electrodeposition.* Applied Surface Science, 2008. **254**(20): p. 6671-6676.
291. Wang, Y. and I. Zhitomirsky, *Cathodic electrodeposition of Ag-doped manganese dioxide films for electrodes of electrochemical supercapacitors.* Materials Letters, 2011. **65**(12): p. 1759-1761.
292. Gu, L., et al., *Anodic electrodeposition of a porous nickel oxide–hydroxide film on passivated nickel foam for supercapacitors.* Journal of Materials Chemistry A, 2014. **2**(20): p. 7161-7164.
293. Sun, X., et al., *Porous nickel oxide nano-sheets for high performance pseudocapacitance materials.* Journal of Materials Chemistry, 2011. **21**(41): p. 16581-16588.
294. Zhu, Y., et al., *Ultrathin nickel hydroxide and oxide nanosheets: synthesis, characterizations and excellent supercapacitor performances.* Scientific Reports, 2014. **4**.

295. Wang, Y., et al., *Mesoporous transition metal oxides for supercapacitors.* Nanomaterials, 2015. **5**(4): p. 1667-1689.
296. Li, J. and I. Zhitomirsky, *Electrophoretic deposition of manganese dioxide–carbon nanotube composites.* Journal of Materials Processing Technology, 2009. **209**(7): p. 3452-3459.
297. Devan, R.S., et al., *One-dimensional metal-oxide nanostructures: recent developments in synthesis, characterization, and applications.* Advanced Functional Materials, 2012. **22**(16): p. 3326-3370.
298. Song, X., L. Gao, and S. Mathur, *Synthesis, characterization, and gas sensing properties of porous nickel oxide nanotubes.* The Journal of Physical Chemistry C, 2011. **115**(44): p. 21730-21735.
299. Gong, M., et al., *Nanoscale nickel oxide/nickel heterostructures for active hydrogen evolution electrocatalysis.* Nature Communications, 2014. **5**.
300. Liu, H., et al., *Highly ordered mesoporous NiO anode material for lithium ion batteries with an excellent electrochemical performance.* Journal of Materials Chemistry, 2011. **21**(9): p. 3046-3052.
301. Needham, S.A., G. Wang, and H. Liu, *Synthesis of NiO nanotubes for use as negative electrodes in lithium ion batteries.* Journal of Power Sources, 2006. **159**(1): p. 254-257.
302. Needham, S., et al., *Nickel oxide nanotubes: Synthesis and electrochemical performance for use in lithium ion batteries.* Journal of Nanoscience and Nanotechnology, 2006. **6**(1): p. 77-81.
303. Xu, J., et al., *Electrochemical capacitance of nickel oxide nanotubes synthesized in anodic aluminum oxide templates.* Journal of Solid State Electrochemistry, 2011. **15**(9): p. 2005-2011.
304. Zhuo, K., M.-G. Jeong, and C.-H. Chung, *Dendritic nanoporous nickel oxides for a supercapacitor prepared by a galvanic displacement reaction with chlorine ions as an accelerator.* RSC Advances, 2013. **3**(31): p. 12611-12615.
305. Meher, S.K., P. Justin, and G. Ranga Rao, *Microwave-mediated synthesis for improved morphology and pseudocapacitance performance of nickel oxide.* ACS Applied Materials & Interfaces, 2011. **3**(6): p. 2063-2073.
306. Fisher, R.A., M.R. Watt, and W.J. Ready, *Functionalized carbon nanotube supercapacitor electrodes: a review on pseudocapacitive materials.* ECS Journal of Solid State Science and Technology, 2013. **2**(10): p. M3170-M3177.
307. Faraji, S. and F.N. Ani, *Microwave-assisted synthesis of metal oxide/hydroxide composite electrodes for high power supercapacitors–a review.* Journal of Power Sources, 2014. **263**: p. 338-360.
308. Gogotsi, Y. and P. Simon, *True performance metrics in electrochemical energy storage.* Science, 2011. **334**(6058): p. 917-918.
309. Stappert, S., et al. *Preparation, Structure, and Sintering of Nickel Nanoparticles*. in *EUREM 2000*. 2000. Brno, Czech Republic.
310. Kim, C., et al., *Expeditious low-temperature sintering of copper nanoparticles with thin defective carbon shells.* Nanoscale, 2015. **7**(15): p. 6627-6635.

311. Ata, M., Y. Liu, and I. Zhitomirsky, *A review of new methods of surface chemical modification, dispersion and electrophoretic deposition of metal oxide particles.* RSC Advances, 2014. **4**(43): p. 22716-22732.
312. Liu, Y., et al., *Film deposition mechanisms and properties of optically active chelating polymer and composites.* Colloids and Surfaces A: Physicochemical and Engineering Aspects, 2015. **487**: p. 17-25.
313. Liu, Y., et al., *Universal dispersing agent for electrophoretic deposition of inorganic materials with improved adsorption, triggered by chelating monomers.* Journal of Colloid and Interface Science, 2016. **462**: p. 1-8.
314. Rivas, B.L., G.V. Seguel, and K.E. Geckeler, *Poly (styrene-alt-maleic acid)–metal complexes with divalent metal ions. synthesis, characterization, and physical properties.* Journal of Applied Polymer Science, 2001. **81**(6): p. 1310-1315.
315. Roy, P., et al., *Accelerated aging of LDPE films containing cobalt complexes as prooxidants.* Polymer Degradation and Stability, 2006. **91**(8): p. 1791-1799.
316. Mazi, H. and A. Gulpinar, *Cu (II), Zn (II) and Mn (II) complexes of poly (methyl vinyl ether-alt-maleic anhydride). Synthesis, characterization and thermodynamic parameters.* Journal of Chemical Sciences, 2014. **126**(1): p. 239-245.
317. Nam, K.-W. and K.-B. Kim, *A study of the preparation of NiO x electrode via electrochemical route for supercapacitor applications and their charge storage mechanism.* Journal of the Electrochemical Society, 2002. **149**(3): p. A346-A354.
318. Prasad, K.R. and N. Miura, *Electrochemically deposited nanowhiskers of nickel oxide as a high-power pseudocapacitive electrode.* Applied Physics Letters, 2004. **85**(18): p. 4199-4201.